NONLINEAR BATHYMETRY INVERSION BASED ON WAVE PROPERTY ESTIMATION FROM NEARSHORE VIDEO IMAGERY

A Thesis
Presented to
The Academic Faculty

by

Jeseon Yoo

In Partial Fulfillment
of the Requirements for the Degree
Doctor of Philosophy in the
School of Civil and Environmental Engineering

Georgia Institute of Technology
December 2007

NONLINEAR BATHYMETRY INVERSION BASED ON WAVE PROPERTY ESTIMATION FROM NEARSHORE VIDEO IMAGERY

Approved by:

Dr. Hermann Fritz, Committee Chair
School of Civil and Environmental Engineering
Georgia Institute of Technology

Dr. Paul Work
School of Civil and Environmental Engineering
Georgia Institute of Technology

Dr. Kevin Haas
School of Civil and Environmental Engineering
Georgia Institute of Technology

Dr. Francesco Fedele
School of Civil and Environmental Engineering
Georgia Institute of Technology

Dr. Christopher Barnes
School of Electrical and Computer Engineering
Georgia Institute of Technology

Date Approved: November 12, 2007

ACKNOWLEDGEMENTS

This research was primarily sponsored by the U.S. National Geospatial-Intelligence Agency. In addition, the field data used in this study was collected under the financial support of the U.S. Geological Survey, the South Carolina Sea Grant and the National Oceanographic Partnership Program.

I would like to express my sincere gratitude to my advisor Dr. Hermann Fritz for this research opportunity, his valuable guidance, continuous support, and patience throughout my studies. I also wish to thank my research co-supervisors: Dr. Kevin Haas, Dr. Chris Barnes, and Dr. Paul Work. Dr. Kevin Haas' expert guidance in nearshore wave processes, Dr. Barnes' expertise in image signal processing, and Dr. Work's timely review for my research progress were of great value. Comments and suggestions of my other committee member, Dr. Francesco Fedele, are also extremely appreciated.

I also appreciate the friendship of my colleagues in coastal engineering, Chris Blount, Fahad Mohammed, Dr. Huseyin Demir, Kemal Cambazoglu, Zafer Defne, Lindsay Check, and Charley Johnson. I want to particularly express my gratitude to my past video research mate Brian Sapp for his kind support and help.

I would also express my sincere gratitude to my parents, Yun-Yi Yang and Jung-Hyun Yoo, and parents-in-law, Soon-Ae Hwang and Chang-Bok Kim, for their love and prayers. Especially, I am greatly grateful to my wife Eun-Hee Kim for her love, patience, and encouragement, and my daughters Irae, Anna and New Baby to be born for being sweet and lovely. Lastly, my Lord has kept me in His grace to complete this research work.

TABLE OF CONTENTS

LIST OF TABLES

LIST OF FIGURES

SUMMARY

Bathymetry in the nearshore changes continuously under energetic interactions with shoaling and breaking waves. A large storm can bring about significant changes of the nearshore bathymetry on a time scale of an hour. Nearshore bathymetry is required to describe depth-induced wave changes and large-scale fluid motions. The evolution of nearshore bathymetry will be predicted based on current bathymetry and nearshore hydrodynamics. Depth inversion methods by remote-sensing have been developed to cover a large span of spatial and temporal scales, substituting conventional labor-and-time intensive in-situ bathymetry survey methods. However, earlier depth inversion methods have limitations at estimating bathymetry accurately in the surf zone because of image noise due to foam induced by wave breaking in the surf zone.

Video based remote sensing techniques are well-suited to collect spatially resolved wave images in the surf zone with breaking waves. Herein, an advanced video-based depth inversion method is developed to remotely survey bathymetry in the surf zone. Optical wave image sequences in time, captured in the nearshore by video cameras mounted on top of a high building, are used. The present method involves image processing of original wave image sequences, wave property estimation based on linear feature extraction from the processed image sequences, and use of a nonlinear depth inversion model.

The original wave image sequences are processed through video image frame differencing and directional low-pass image filtering (i.e. an elliptic Butterworth filter) to remove the noise arising from foam in the surf zone and characterized by high frequencies in the video imagery. The processed image sequences are rectified into the real

world coordinates to generate cross-shore image timestacks which collect time-series of pixel intensity at a one dimensional array along a cross-shore transect in the rectified image sequences. The extraction of individual wave crest features are conducted in the processed cross-shore image timestacks having a two dimensional space-time domain. The features of individual crest trajectories are extracted by tracking pixels of high intensity values within an interrogation sub-window of a Radon-transform-based line-detection algorithm. The wave phase celerity is computed using space-time information of the individual wave crest trajectories extracted in the cross-shore timestack domain.

The computed nearshore bathymetry from video image sequences is based on a nonlinear depth inversion using the nonlinear shallow water wave equation theory. The present nonlinear depth inversion method consists of 3 model components: wave breaker model, wave dissipation model, wave shoaling model. The nonlinear wave amplitude dispersion effects at the breaker points are determined by the wave breaker model, i.e. combining the approximate nonlinear shallow water wave equation-based celerity equation with a wave breaker criterion, thereby computing water depths iteratively from the celerity derived from the video data. The water depths estimated at the breaker points present initial bathymetric anchor points. Bathymetric profiles in the surf zone are inverted by calculating wave heights after wave breaking with the wave dissipation model and wave heights shoaled before wave breaking with the wave shoaling model. The continuous wave amplitude dispersion effects are subtracted from the measured celerity profiles, resulting in nearshore bathymetric profiles.

The nonlinear depth inversion derived bathymetric estimates from nearshore imagery match the measured values with a biased mean depth error of about +0.06m in the depth range of 0.1 to 3m. In addition, the wave height estimates by the depth inversion model are comparable to the in-situ measured wave heights with a biased mean wave height error of about +0.14m. The present depth inversion method based

on optical remote-sensing supports coastal management, navigation, and amphibious operations.

CHAPTER I

INTRODUCTION

1.1 Background

Beach and nearshore processes are dominantly characterized by the extremely dynamic breaking of waves coming from offshore. Bathymetry in the nearshore changes continuously under the energetic interactions with shoaling and breaking waves. A large storm can bring about significant changes of the nearshore bathymetry on a time scale of an hour. Human activities and residency are increasing along the coast, being exposed to the dynamic waves on nearshore beaches. For this reason, continual investigation of bottom topography in the nearshore regions is necessary for societal perspectives as well as scientific purposes. From a societal point of view, for instance, navigation of ships in military operations requires very recently updated bottom topographic maps. In addition, coastal development and management issues such as the planning and design of coastal structures and beach protections along the coasts should include knowledge of littoral bathymetry. With respect to the scientific purposes, nearshore bathymetry is required to describe depth-induced wave processes. Further, future evolution of the nearshore bathymetry will be predicted based on the initial bathymetry and the depth-influenced nearshore hydrodynamics.

Conventionally, bathymetry surveying has been conducted through in-situ measurements, using a total station and a survey rod, sonar-based bathymetric soundings, or amphibious vehicles, etc. However, the in-situ measurement techniques are limited in observing beach profile variations at time scales of hours to days, since these techniques are typically slow, expensive, and labor-intensive. In addition, these techniques

are not suitable to stormy weather situations. In order to overcome the shortcomings of in-situ techniques, several remote sensing techniques have been applied such as video-, radar-, altimeter-, or satellite-image based measurements, enabling temporally high resolution nearshore bathymetry to be obtained (Dugan et al, 2001; Bell, 1999; Leu et al, 1999; etc.).

In the estimation of littoral bottom profiles using the remote sensing techniques, it is not easy for the techniques other than video-based monitoring methods to collect spatially high resolution wave image sequences in the surf region which extends from O(10∼100m), and in which waves start to break and bathymetric changes are most dynamic. In the case of the video imaging techniques, even though it acquires spatially high resolution images in the surf-zone area, the previous video based bathymetry inversion methods have showed poor performance in the surf zone compared to the performance achieved in the offshore zone (Stockdon and Holman, 2000). This is mainly due to the assumption that image pixel intensity signals correspond to water level signals (Lippmann and Holman, 1991). This approach applied to bathymetry estimation is deteriorated by persistent foam generated by wave breaking.

1.2 Research objectives and scope

The earlier works (Stockdon and Holman, 2000) exhibit significant errors in analyzing and extracting wave properties in the surf zone from wave imagery taken in the nearshore, in which wave and water motions are extremely dynamic, compared to the results from the offshore image sequences. In addition, although synthetic wave data-based depth inversion algorithms, which will be reviewed in Chapter 2, consider the effects of nonlinear amplitude dispersion, most depth inversion algorithms based on field data cannot include the effects of nonlinear amplitude dispersion. This is because planar remote sensing platforms are not capable of obtaining water surface

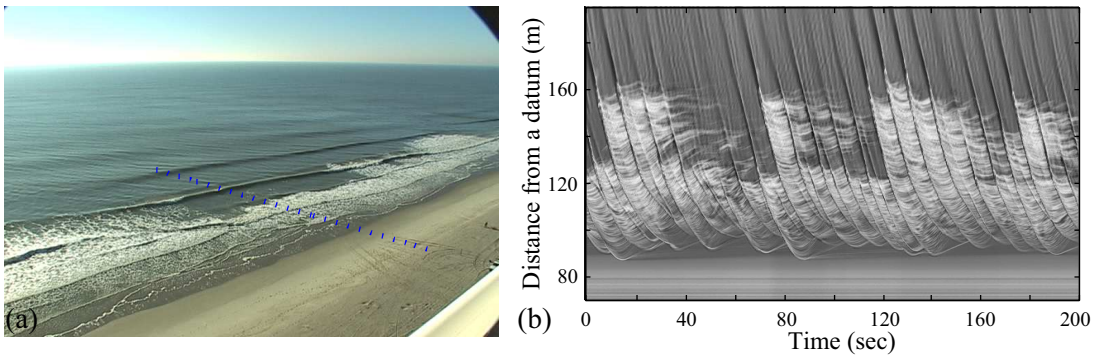

Figure 1: A segmental cross-shore image timestack sampled at 3 Hz from the Myrtle Beach video captured on Dec. 13, 2003 (Haas et al., 2004): (a) cross-shore transect in an original image frame to generate an original image timestack, (b) the generated original image timestack having a two dimensional space-time domain.

elevation data without stereo-optics.

The purpose of this study is to improve estimation of surf-zone bathymetry by developing video-based wave property estimation methods. This method involves development of image processing methods to minimize the influence of the persistent foam on wave information extracted from image sequences. Wave properties such as wave celerity, wave period, wavelength, and incident wave angle are estimated in a two-dimensional space-time domain, i.e. from cross-shore image timestacks which are generated by collecting time-series of pixel intensity at a one dimensional array along a cross-shore transect from image sequences in time. Fig. 1 shows an example of cross-shore image timestacks. The cross-shore image timestack in Fig. 1(b) is presented in a two dimensional space-time domain. The cross-shore direction is positive offshore. The slightly curved trajectory patterns are individual waves propagating onshore.

This study also aims to include the nonlinear effects in the depth inversion model by retrieving wave height information from video imagery. Thus, the following issues are investigated in this study:

- development of an image processing methodology to remove noise due to foam from wave signals obtained from nearshore video image sequences.

- identification of wave crests in video image sequences, i.e. cross-shore image timestacks in a two dimensional space-time domain.
- estimation of wave properties such as incident wave angle, wave celerity, wave period, and wavelength from wave image sequences by utilizing space-time information of the identified wave crests.
- detection of wave breaking points in the wave image sequences.
- estimation of wave heights and water depths at the breaker points.
- estimation of wave height dissipation after wave breaking in the surf zone.
- estimation of wave shoaling related transformation before wave breaking in the nearshore.
- analysis of the nonlinear amplitude effects on wave phase speeds.
- estimation of nearshore bathymetry by subtracting the contribution of the nonlinear effects from the phase speed profiles along the cross-shore transects.
- investigation of the effects of error sources on the video-derived nearshore depth inversion.

1.3 Thesis overview

In Chapter 2, previous studies on remote-sensing-based bathymetry survey are reviewed, discussing their algorithms, advantages and shortcomings. In Chapter 3, the procedure for wave crest feature extraction by applying image processing methods to the captured image sequences is described. In addition, the experimental field datasets used in this study are briefly described. In Chapter 4, wave property estimation methods are developed by utilizing the extracted wave crest features, the original

image sequences and the processed image sequences. In Chapter 5, a video-based nonlinear depth inversion algorithm is developed to predict water depths with inclusion of the nonlinear amplitude dispersion effects by utilizing video imagery derived wave properties. The present nonlinear depth inversion algorithm computes breaking wave heights and water depths at wave breaking points by combining a nonlinear shallow water wave theory and a breaker criterion. In addition, the algorithm includes a wave dissipation model and a wave shoaling model for computing wave heights transformed after and before wave breaking, respectively. Thereafter, the wave height contributions to wave phase speeds are subtracted from the measured celerity using a nonlinear shallow water wave theory based wave celerity equation. The algorithm produces bathymetric profiles from the wave phase speed profiles estimated using the extracted wave crest trajectories. The iteration of the inversion algorithm updates the beach profiles until bathymetric change between iteration steps is less than a certain threshold limit. In Chapter 6, the results of wave feature extraction, wave property estimation, and the nonlinear depth inversion are investigated and discussed by use of the error source and accuracy analyses. A summary of the main results and some future research considerations conclude the thesis in Chapter 7.

CHAPTER II

LITERATURE REVIEW

2.1 Introduction

In order to survey nearshore bathymetry remotely, several remote sensing methods have been applied either to measure water depths directly or to estimate water depths indirectly by depth inversion modeling through estimation of water surface movements. The group of direct measurement methods is basically to utilize the fact that the light penetrates to different depth levels at various wavelengths in the water column. The other group of indirectly estimating bathymetry infers water depths by measuring water surface characteristics. The approach of this group is to model nearshore bathymetry inversely by estimating depth-induced wave properties from remotely captured images, identifying waves, and using water wave dispersion relation. This chapter will review the direct bathymetry survey methods briefly, and focus on the indirect measurement group of the remote-sensing based depth inversion methods which involve use of nearshore wave processes.

2.2 Direct bathymetry survey by remote sensing

The techniques in this group depends on optical clarity of sea waters, and usually requires empirical algorithms for retrieving water depths from optical complexities caused by scattering and attenuation of incident light in the water column, and bottom reflection as well. For the direct extraction of the coastal bathymetry, spectral satellite/airborne technology (Adler-Golden et al., 2005; Benny and Dawson, 1983; Bierwirth et al., 1993; Lee et al., 2001; Sandidge and Holyer, 1998), and light detection and ranging (LIDAR) technology (Irish and Lillycrop, 1999) have been suggested.

Benny and Dawson (1983) and Bierwirth et al. (1993) demonstrated retrieval of water depths with Landsat multi-spectral scanner (MSS) and Landsat Thematic Mapper (TM).

Benny and Dawson (1983) could detect and contour shallow water area and shoals less than 18 m depths in a region at the northern end of the Red Sea using the Landsat MSS system, aiming to apply to nautical charting. Bierwirth et al. (1993) applied the Landsat TM system to survey Shark Bay in Western Australia and their method overestimated water depths by several meters. Sandidge and Holyer (1999) used hyperspectral image data from the Airborne Visible/Infrared Imaging Spectrometer (AVIRIS) to derive nearshore bathymetry in Tampa Bay in Florida and in the Florida areas over a depth range of 0 to 6 m. The root mean square (rms) errors when compared to ground truth data in the two areas were 0.84 m and 0.39 m respectively. Lee at el. (2001) also applied an AVIRIS technique to survey water subsurface properties in Tampa Bay using a model-driven optimization algorithm without prior knowledge of the water optical properties. The derived depths ranged from 0.3 to 4.6 m. Adler-Golden et al. (2005) applied a physics-based algorithm which uses minimal ground truth input to hyperspectral (AVIRIS; LASH - Littoral Airborne Sensor Hyperspectral) and multispectral (Quickbird) imagery to retrieve depths and seafloor topography in Tampa Bay in Florida and in Kaneohe Bay in Hawaii. The accuracy of the computed depth was within 2$\sim$3 meters over a depth range of 0 to 10 m.

The LIDAR-based method, named SHOALS, of Irish and Lillycrop (1999) showed greater bathymetry estimation performance than the spectral methods mentioned above, having maximum measurable water depths of up to 60 m and a vertical accuracy of about 15 cm. The direct bathymetry survey methods are highly dependent on water clarity and require prior knowledge of the relation between the optical water properties and water depths.

2.3 Indirect bathymetry estimation by depth inversion methods

There are several different ways to classify depth inversion methods: frequency domain inversions or time domain inversions; priori or full approaches; depth-induced spatial water surface variation based inversions, depth-induced wave property based inversions or wave breaking generated dissipation pattern-based inversions; field-data-based or synthetic-data-based inversions; etc.

Misra et al. (2003) subdivided depth inversion methods into frequency domain inversions and time domain inversions. Depth inversions in the frequency domain take temporally dense wave image data, and analyze by the spectral analysis, and then invert the depths from linear dispersion relation using wave parameters obtained by the spectral analysis. On the other hand, time domain inversions utilize temporally sparse wave information obtained from one or two sequential images of wave phase or surface elevation maps with reasonably short time interval.

The classification of the inversion methods by Narayanan at el. (2004) is two sub-groups of a priori and full approaches. The a priori inversions simply use a previously specified dispersion relationship relating wave properties and water depths, whereas the full inversions use all physical properties provided by a numerical model for wave propagation influenced by water depths.

Aarninkhof et al. (2005) subdivided the indirect group broadly into three sub-groups: depth inversions relying on depth-induced spatial variations in water surface roughness, cross-shore changes in local wave number or wave celerity over a varying depth profile, and cross-shore dissipation patterns caused by depth-induced wave breaking.

Catalan (2006) identified the earlier inversion methods as two sub-groups of field-data-based and synthetic-data-based inversions. Field-data-based inversions use wave parameters obtained from remotely sensed field data as inputs to the linear wave

dispersion relation, while wave data used in the synthetic-data-based inversions are numerically generated to provide all physical wave processes some of which cannot be remotely acquired in the present situations of remote sensing techniques such as wave heights and water particle velocities.

A variety of depth inversion methods have been developed along with advance of various remote sensing techniques. For instance, in order to remotely measure water surface characteristics influenced by bathymetry, several remote sensing platforms have been developed such as airborne video (Dugan et al., 2001), tower mounted video (Stockdon and Holman, 2000), microwave X band radar (Bell, 1999), synthetic aperture radar (SAR) (Greidanus, 1997), and SPOT satellite (Leu et al., 1999) images. Those measurements commonly cover a large span of spatial and temporal scales, being capable of continually monitoring on a time scale of one hour and on a length scale of 1 km. However, each of those remote sensing platforms has its own limitations as well as advantages over others in terms of image resolution, spatial image coverage, and temporal image collections, etc. For this reason, several different approaches for remotely estimating littoral seafloor topography can be considered depending on input image data types. Since availability and quality of the remotely collected wave image data determine a best suitable depth inversion method, herein, previous depth inversion methods are reviewed through classifying them with a basis of how to approach and analyze wave data.

For instance, the airborne optical platform allows much more orthogonal measurements over the sea surface than shore-mounted platforms, and continuous sampling wave imagery at high frequencies over a target area on the scale of an hour to a day, flying around the area of the interest. Thus, the airborne video imaging provides highly uniform physical resolution over the 2-D image space. Dugan et al. (2001) retrieved surface currents and water depths from three-dimensional (3-D: space-space-time) data cubes. Individual wave images in time sequence are stacked on top of them

to generate the 3D data cubes. The 3D data cubes are analyzed to estimate surface currents and wave properties of wavelengths and wave periods using 3-D fast Fourier transform (FFT) analysis. However, shore-mounted video cameras look down at the sea at more oblique angles, sampling 2-D image-time sequences of which physical resolution in the image domain decreases with distance from the cameras. In this case, the physical resolution over the oblique image frame is not quietly consistent so that it may not be adequate to utilize 3-D data cubes from the obliquely captured image sequence for wave property extraction. Instead, Stockdon and Holman (2000) collected pixel intensity time series at an array of pixel locations in the cross-shore direction, i.e. a cross-shore timestack (space-time image), from the obliquely sampled 2-D image sequence to trace wave crests. Lippmann and Holman (1989) averaged wave images taken by tower mounted video camera for 10 minutes to generalize wave breaking patterns in the nearshore, and quantified sand bar locations and morphology. In contrast to locally operated platforms, satellites orbit around the Earth and acquire only one snapshot image or can sample wave images over a target area for a few seconds. For cases where the surface information is collected sparsely in time, Dalrymple et al. (1998) developed two depth inversion methods using the Hilbert transform and lag-correlation methods from two sequential images. In fact, Dalrymple et al. (1998) numerically generated the two sequential surface elevation maps with a reasonably short time interval, instead of using actual images.

Previous depth inversion methods can be classified into 4 sub-groups according to input image data types: (1) 3-D data cube methods, (2) timestack methods, (3) time-exposed image methods, and (4) sparse time-lapsed image methods. These sub-groups will be reviewed in detail in separate subsequent sub-chapters.

2.3.1 Wave dispersion relations for depth inversion

The depth inversion methods based on the first two sub-groups, 3-D FFT methods and timestack methods, compute water depths by relating wave parameters such as wave period (T) and wavelength (L) and current velocity obtained by the two sub-groups to the general form of the surface gravity wave dispersion relation (Dean and Dalrymple, 1991),

$$\omega = \sqrt{gk \times tanh\,(kh)} + \vec{U} \cdot \vec{k} \tag{1}$$

where $\omega = 2\pi/T$ is the frequency, g is the gravitational acceleration, h is the local depth, $\vec{U}$ is the water mean velocity vector, and $\vec{k} = (k_x, k_y)$ is the wave number vector of magnitude k which is defined as $2\pi/L$. Since water waves become less dispersive and wave phase speed (or celerity) becomes more strongly dependent on water depth rather than on the wave parameters as they propagate toward shallower water, the phase speed has been more practically used for depth determination by substituting for either one of the frequency and the wave number as shown as the follows:

$$c = \frac{\omega}{k} = \sqrt{\left(\frac{g}{k}\right) tanh\,(kh)} \tag{2}$$

with the assumption of $\vec{U} \cdot \vec{k} = 0$. In deep water ($kh > 0.5$), Eq. 2 simplifies to

$$c_o = \sqrt{\frac{g}{k}} = \frac{g}{\omega} = \frac{gT}{2\pi} = \frac{L_o}{T} \tag{3}$$

where the subscript o denotes deep water conditions and L_o is deep water wavelength obtained from Eq. 1 with the no-current and deep water assumptions as

$$L_o = \frac{gT^2}{2\pi} \tag{4}$$

From Eqs. 2 and 3, the celerity of a wave propagating from deep water toward shallower water can be expressed as

$$c = c_o \sqrt{tanh\,(kh)} \tag{5}$$

In shallow water ($kh < 0.05$), the approximation of Eq. 2 becomes

$$c = \sqrt{gh} \tag{6}$$

which is a function of water depth only, being independent of wave number. However, a number of previous researches have shown that the shallow water linear dispersion relation underestimates the wave speed within the surf zone close to shoreline because of the finite amplitude effects. Suhayda and Pettigrew (1977), for instance, showed that the wave speeds within the surf zone featuring plunging waves exceed by up to 20% the solitary wave theory based wave speed approximation ($c = \sqrt{gh_c}$ where h_c is depth from the wave crest to the seafloor) near breaking points. Thornton and Guza (1982) also found that the measured celerity values were up to 20% higher than the predicted by the linear dispersion relation at wave breaking and inside the surf zone. Thus, in consideration of the nonlinear effects of finite wave amplitudes, Holland (2001) formulated the shallow water dispersion using the cnoidal wave speed equation and the field data measured at the U.S. Army Corps of Engineers Field Research Facility, Duck, NC, and suggested for the remote sensing-based depth inversions an empirical shallow water dispersion relationship,

$$h = \frac{c^2}{g} - \alpha H_s = \frac{\omega^2}{gk^2} - \alpha H_s \tag{7}$$

where H_s is significant wave height and α is an empirical coefficient. Holland (2001) showed that the coefficient value of $\alpha = 0.48$ set in the surf zone for depth less than 4 m reduced the overall bias of the computed shallow depths from 41 cm to 3 cm on average.

2.3.2 3D data cube based depth inversions

3D FFT techniques are mainly used to extract 3D directional wave power spectra from the 3D image cubes in which the spatial and temporal sea surface elevation information is stored. The spectrum from the 3D image cubes is not based on the true wave signal $X(f)$ for the wave amplitude, but on the remotely sensed signal $G(f)$. Hence, the remotely sensed signal is used as a proxy for the true signal. The observed relationship between them can be represented by the modulation transfer function, $M(f)$, (Gonzales and Woods, 1992) as

$$G\left(f\right) = M\left(f\right) X\left(f\right) \tag{8}$$

which describes the relationship of both the phases and amplitudes between the two signals. Preliminary tests of the relationship between the video and pressure sensor data by Lippmann and Holman (1991) showed high coherence of cross spectra between them. Most techniques reviewed in this chapter and techniques used in this study are primarily derived based on signal phases.

A 3-D FFT transforms the spatial and temporal information consisting of pixel intensity values, $I(x, y, t)$, in the space-time domain to the spectral wavenumber-frequency domain

$$\left|FFT\left(I(x,y,t)\right)\right|^2 = \Phi\left(k_x, k_y, \omega\right) \tag{9}$$

where k_x and k_y are the components of the wavenumber vector $\vec{k} = (k_x, k_y)$ and Φ is the 3-D image energy spectrum. The spectral energy is located on the dispersion relation shell in the spectral wavenumber-frequency domain. The theoretical dispersion shell of Eq. 1 in the spectral wavenumber-frequency domain is illustrated in Fig. 2 for deep water and no current conditions.

With the condition of no currents ($\vec{U} = 0$) and deep water, the spectral energy

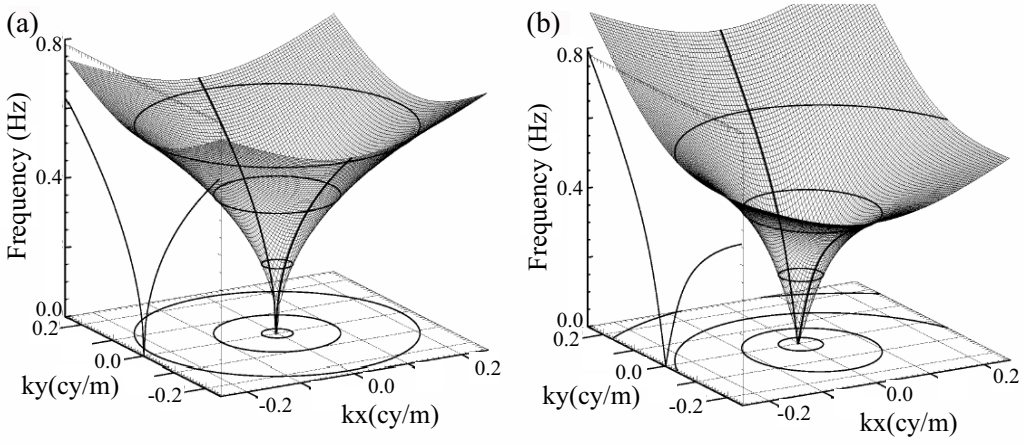

Figure 2: Theoretical linear dispersion shell for (a) infinite depth and no current and (b) 4-m depth and a current magnitude of 65 cm/s in y - direction (Piotrowski and Dugan, 2002).

is distributed on the symmetrically curved dispersion shell as shown in Fig. 2(a). However, water movement by near-surface currents deforms the dispersion shell as shown in Fig. 2(b) on which the frequency-wavenumber spectra of the modulations are located. Hence, once a 3-D image energy spectrum is obtained from the 3-D data cube of wave images, the depth (h) and near-surface current ($\vec{U}$) are estimated by fitting the dispersion shell of Eq. 1 to the 3-D energy spectrum distribution.

Dugan et al. (2001) applied this technique using a relatively coarse spatial window resolution of the 256×256 pixel patch (∼500×500 m) to retrieve water depths and currents in the offshore from airborne optical imagery taken at Duck, NC. Dugan et al. (2001) showed that depth retrieval results by the technique compared well to a bathymetric survey at depths of 4 ∼ 12 m, with root-mean-square (RMS) errors ranging from 5 to 13%. Biases due to nonlinear effects were observed, but they were neglected because the biases are relatively small compared to the RMS errors. Trizna (2001) measured in depths between 3.6 and 5.8 m using 3-D FFT analysis of radar image sequences with the spatial window resolution of 384 × 384 m, and observed that the errors increased with greater wave heights and shallower water depths. Piotrowski

and Dugan (2002) showed that a data cube either temporally or spatially small in size contributed to significant errors, whereas the spatial resolution of a pixel and image sampling rate were less critical in controlling error.

The 3-D data cube technique implies that waves propagate in stationary and homogenous conditions and water depth is constant over the sample window on a length scale of O(100m). So, the assumption of this approach is not adequate for sea state conditions that water surface varies appreciably over the spatial sample window as waves are propagating and shoaling in the surf zone. The minimally required sampling window size is also too big to investigate rapid changing bathymetry near the surf and the shoreline.

2.3.3 Timestack based depth inversions

This approach involves collecting time series of pixel intensity at a 1-D array of pixel locations in the 2-D spatial domain, typically along a cross-shore direction for bathymetry survey. Thereafter, wave parameters at each cross-shore location are estimated from the space-time data plane, called a timestack, resulting in inputs for depth inversion modeling. Fig. 3 represents a cross-shore timestack, and the traces of wave crests are clearly visible up to the wave breaking points. The slice of the timestack at each cross-shore location illustrates the variations in pixel intensity in time as a proxy for wave amplitudes.

Stockdon and Holman (2000) calculated the frequency and the cross-shore and longshore wavenumber from timestacks, and inverted nearshore bathymetry between 0 and 5 m in depths using the linear dispersion relation assuming no currents. Wave frequency estimation by Stockdon and Holman (2000) was performed by calculating intensity based energy spectra from a cross-shore timestack at each cross-shore location and averaging spectra over all cross-shore locations, selecting the spectral peak

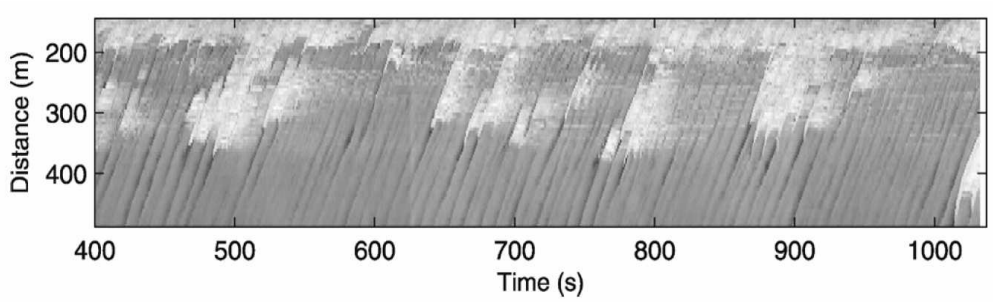

Figure 3: Example of a cross-shore intensity timestack sampled with 2 Hz from Duck in November, 1997. The cross-shore direction is positive offshore from the shoreline. The slightly curved patterns are individual waves propagating onshore (Aarninkhof and Ruessink, 2004).

frequency as the input frequency. For determination of the cross-shore wavenumbers, the method of a frequency domain complex empirical orthogonal function (CEOF) analysis, which is generally used to detect propagating signals at different frequencies, is applied to the normalized cross-spectral matrix of the pixel intensity signals. The analysis provides a normalized eigenvector, and the first mode complex eigenvector $\Lambda_1 = a(x) + ib(x)$ is used to calculate the phase ϕ and amplitude A along the cross-shore as:

$$A(x) = \sqrt{a(x)^2 + b(x)^2} \tag{10}$$

$$\phi(x) = tan^{-1}\left(\frac{b(x)}{a(x)}\right) \tag{11}$$

From the phase variations in the cross-shore direction, the wave number is obtained by calculating the phase gradient:

$$k_x(x) = \frac{d\phi}{dx} \tag{12}$$

In the same way, the longshore wavenumber is calculated by conducting a similar eigenvector analysis of a longshore pixel intensity array set as:

$$k_y(x) = \frac{d\phi}{dy} \tag{13}$$

In addition, wave angle α at each cross-shore position can be determined from the cross-shore and longshore components of wavenumber as:

$$\alpha(x) = tan^{-1}\left(\frac{k_y(x)}{k_x(x)}\right) \tag{14}$$

where α is incident wave angle at each cross-shore location.

Stockdon and Holman (2000) investigated the accuracy of their inversion technique from the video data collected hourly over one month period at Duck, North Carolina. The results were in good agreement with surveyed bathymetric data, showing that the mean relative error was 13% biased toward water depth overestimation. However, the error in the mean bias in shallow water (less than 3 m in depth) was three times higher than the mean bias of -0.20 m in deeper water, and tended to increase with wave heights. In addition, the comparison between the solitary theory based phase speeds and the linear theory based phase speeds in the saturated surf zone (inner surf zone) showed that water depths when using the linear theory could be overestimated up to 42% due to the nonlinear effects of finite-amplitude dispersion.

This technique did not only have relatively large errors in the surf zone, but also filtered out most of the image intensity data in the region between the shoreline and the onset of breaking by the significance test. This method was not successful at depth inversion in the breaker zone.

2.3.4 Time exposed imaging based depth inversions

In contrast to the previous two techniques, this one utilizes persistent high intensity values caused by wave breaking in the breaker zone. Initially, this technique was employed by Lippmann and Holman (1989) to obtain statistically stable wave breaking

patterns in the nearshore by exposing and averaging out video wave images over a 10-minute period. Lippmann and Holman (1989) visualized underlying morphology such as sand bar locations and cross-shore and longshore length scales using 2-D images of wave breaking patterns averaged over the 10-min period. Ruessink et al. (2000) quantified nearshore bar crest locations using time-averaged X-band radar images. The basic assumption of this method is that the sand bar locations correspond to high intensity peaks of the time-averaged intensity profile in the cross-shore direction, relying on the fact that sand bars cause persistent wave breaking, that is, high intensity values in wave images. However, the image based bar crest positions generally do not match the real bar positions, but vary depending on wave heights, water levels and characteristics of bathymetry. Van Enckevort and Ruessink (2001) investigated the effects of those parameters on estimates of the bar crest positions based on the wave energy and roller balance modeled using the time-averaged intensity profile at the double-barred beach of Egmond aan Zee, Netherlands. The results showed that the distance difference, δx, between the predicted and the measured bar positions was on the order of 10 m, and the predicted bar position moved offshore with either increase of offshore wave height or sea level decrease under unsaturated conditions. When the wave field was in saturated conditions in which most of incoming waves were breaking, δx depended on only changes of offshore water level.

Aarninkhof et al. (2005) developed a beach mapping model, called Subtidal Beach Mapper (SBM), for monitoring bathymetric evolution in the nearshore subtidal zone over extended time scales (more than years) using time-exposured (hours) video images. This model requires the input of an initial depth profile, either measured or obtained from a previous run of the model, prior to model operation. The basis of SBM is that the cross-shore intensity profile of the time-exposure images of breaking waves can be used as the dissipation proxy for the roller energy. Some portion of high intensity foam patches in image sequences is newly generated by a present wave

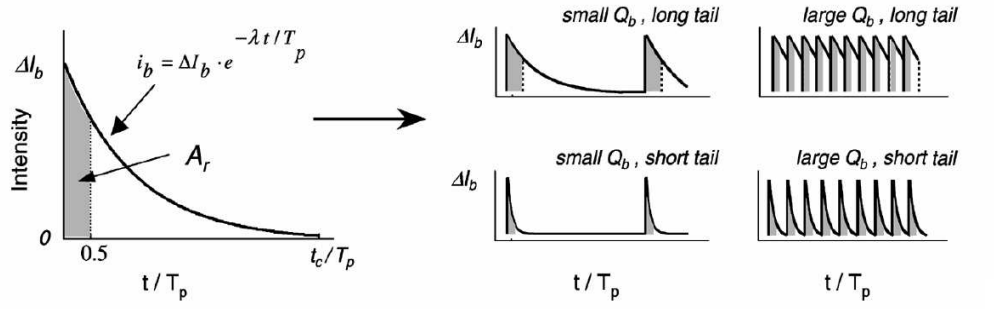

Figure 4: Intensity description of an individual breaking wave, showing the intensity increase during the passage of the wave roller (gray-shaded area) and the subsequent persistent foam (blank area) for different fractions of breaking waves (Q_b) (Aarninkhof and Ruessink, 2004).

breaking event while another portion remains from the aerated rollers due to earlier wave breaking events. For this reason, the escaped persistent foam is removed by assuming that the roller-induced contribution to intensity time series lasts only for $0 \leq t \leq 0.5\ T_p$, where T_p is wave period during a wave passing by as shown in Fig. 4.

The video-derived dissipation observation of the wave roller $D_o(x)$ is compared with the predicted dissipation $D_c(x)$ modeled from the depth profile output at the previous step. The local positive and negative differences, $D_c(x) - D_o(x)$, calculated by the comparison between the two results in predicted local seabed erosion and seabed accretion respectively, implementing the depth profile update. Aarninkhof et al. (2005) tested SBM using one year video data exposed hourly at Egmond aan Zee, Netherlands. The results of SBM derived depth profiles were in good agreement with the bathymetry surveyed after one year. The RMS error on the inner bar was smallest as much as about 0.2m, and the largest RMS error of 0.6m was at the outer bar trough.

This technique does not involve estimating wave parameters for quantification of

nearshore bathymetric signatures like the two methods described in the two subsections above. It uses high intensity peaks of time-averaged images to quantify underlying sandbar locations or time-averaged cross-shore intensity profiles to model the update of bathymetric change. This approach is not suited to computing cross-shore depth profiles unless the initial bathymetry is given.

2.3.5 Sparse time-lapsed imaging based depth inversions

This technique does not require temporally dense image sequences, and utilizes one or two sequential images of wave phase or surface elevation maps over a reasonably short time interval less than wave period. Leu et al. (1999), and Leu and Chang (2005) deduced water depths less than about 12 m from two SPOT satellite images taken in deep and shallow water regions. Assuming waves are propagating from deep water to shallow water, first, dominant deep water wavenumber and wave frequency are estimated from 2-D wave phase information of the deep water image. Thereafter, 2-D wavenumber spectrum of the shallow water image is analyzed, thereby deriving the water depth using the linear dispersion relation. The physical distance of sampling window was 200 m (32 pixels), which is not adequate for the nearshore region close to the shore.

The effect of the nonlinear wave amplitude dispersion contributes significantly to the errors of depth inversion in the nearshore area via the linear dispersion relation. So, wave surface information should be measured and included in the depth inversion. However, the current status of remote sensing measurements offers only image intensity as a proxy of wave amplitude as mentioned earlier. For this reason, synthetic maps of free surface elevation were numerically generated by nonlinear wave models to use for nonlinear depth inversions. Grilli (1998) produced periodic and non-breaking waves using a fully nonlinear potential flow (FNPF) model for a planar

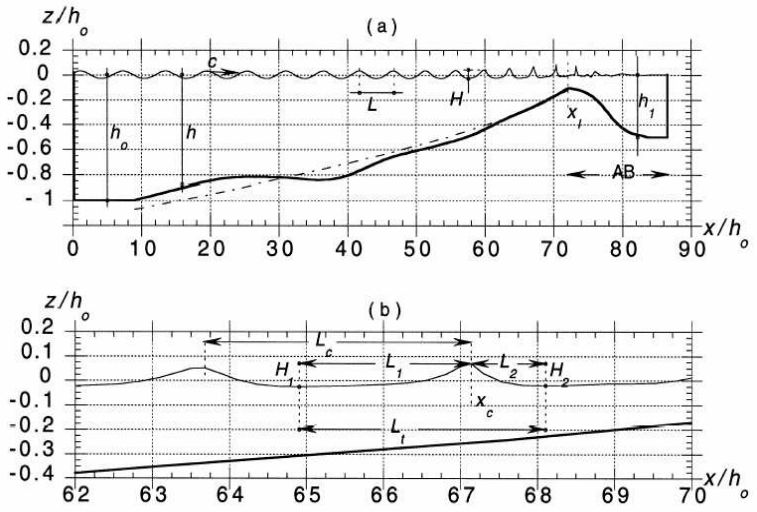

Figure 5: Definition of the wave geometric characteristics used in the depth inversion algorithms; (a) an instantaneous sketch of periodic wave shoaling computation by FNPF, (b) detail of (a) (Grilli, 1998)

sloping beach, and retrieved from the synthetic wave data the empirical relations of the wave celerity ratio c/c_o and the wave asymmetry. Those empirical relations were formulated as functions of local wave number k, local water depth h, and the offshore steepness $k_o H_o$. Local celerity c, local wave height H, and two local characteristic wave lengths L_c and L_t defined in Fig. 5(b) are obtained from two successive snapshots of surface elevation maps. In addition, wave period T is computed using c, L_c and L_t. Thereafter, the local depth h is estimated iteratively by updating offshore wave height Ho from the normalized wave steepness $Hc_o/H_o c$ as a function of kh.

For the case that water surface elevation information cannot be obtained remotely, the empirical relation of the wave asymmetry s_2/s_1 with $s_2 = H_2/L_2$ and $s_1 = H_1/L_1$ was used instead of the wave celerity ratio c/c_o, assuming $s_2/s_1 \simeq L_1/L_2$. L_1 and L_2 denote horizontal distance from a crest to the previous (seaward) and next (landward) troughs, and H_1 and H_2 are their corresponding vertical distance. Those depth inversion algorithms reproduced beach profiles with normalized relative errors of about 1 and about 6% respectively, whereas the depth inversion by linear

wave theory revealed errors up to 50%. One critical limitation in those algorithms is that they can be applied only to monochromatic wave conditions. Another critical limitation is that it is practically difficult to read out wave trough points (i.e. L_t, L_1, L_2) from wave images.

Kennedy et al. (2000) employed a fully nonlinear Boussinesq model to generate two synthetic spatial maps of free surface elevation and water particle velocities. From the two snapshots of dense spatial measurements of free surface elevation generated within a reasonable time interval less than wave period, local phase speeds c_m as the measured speeds are computed using 2-D cross-correlation analysis. The first spatial measurements of free surface elevation and velocities and the initial guess of bathymetry (i.e. flat bed) are input to the Boussinesq model to produce surface elevations and velocities at the second measurement time. This results in the computed local phase speeds c_l derived by the model.

By comparing c_m and c_l and updating local water depths, the predicted depth h_m is determined iteratively using

$$h_m = h_l \left(\frac{c_m}{c_l} \right)^4 \tag{15}$$

where h_l is the newly updated local depth at the previous step, which was empirically adjusted to cover the wavelength scale in shallow water to intermediate depths. This algorithm requires measurements of both surface elevation and particle velocities which are not available from current remote sensing platforms.

Misra et al. (2003) improved the technique of Kennedy et al. (2000) so as to compute local phase speeds from measurements of either the surface elevation or the particle velocities using a least-squares method. In addition, their inversion algorithm can calculate particle velocities from the measured surface elevation and vice versa. However, their method is not still applicable to most remote sensing measurements.

2.4 Conclusions

Various remote sensing platforms have been applied to measure wave characteristics in the coastal region. The current remote sensing techniques do not provide water surface elevation measurements without stereo-optics, whereas they provide good spatial and temporal wave phase information. For an alternative to water surface elevation, image pixel intensity is used as a proxy for water surface elevation. Wave properties such as wave period, wavelength, wave phase speed, and water surface currents are extracted from the remotely acquired wave images in the coast.

The remotely measured wave data, in the advantageous perspective, have activated the indirect ways to survey the nearshore bathymetry cost and labor effectively. The previous depth inversion techniques show good performances to estimate water depths in intermediate water depths up to wave breaking lines, although most of them employ the linear dispersion relation to compute water depth using the remotely measured wave properties.

Each depth inversion technique has its own advantages and short comings. Commonly, previous inversion techniques are not successful at modeling depth inversion in the surf zone compared to intermediate water. Inclusion of nonlinear amplitude effects has not been considered in the depth inversion modeling in the surf zone due to lack of measurements of water surface elevation by planar remote sensing platforms. In addition, remotely captured optical wave imagery contains noisy signals other than wave signals due to foam generated by wave breaking in the surf zone, causing significant errors in the imagery derived depth inversion.

CHAPTER III

WAVE CREST FEATURE EXTRACTION USING IMAGE PROCESSING METHODS

3.1 Introduction

This study involves developing a video-based depth inversion technique to inversely compute water depths from depth induced wave properties such as incident wave angle, wave phase speed, wave period, and wavelength, which can be evaluated from nearshore video image sequences. Video platforms can provide high resolution wave signals in the nearshore in the space and time domains. One of the challenging issues arising from video-based surf zone research is that drifting foam patches in the breaking zone deteriorate wave signals in the form of image pixel intensity, hindering accurate computation of the wave properties from the captured surf zone imagery. For instance, Fig. 6 shows that the high intensity foam patches contained in a raw image make it difficult to distinguish wave crests in the surf zone.

In earlier studies, the image data were smoothed with low-pass filters to remove the foam induced signals (e.g. frequency $f > 0.5\ s^{-1}$: Stockdon and Holman 2000). Nevertheless, errors of the wave property estimates from the filtered image data were relatively larger in the surf zone than in the offshore because of incomplete foamy noise removal. An image processing methodology is developed to remove or filter out the foam patches in this study, thereby, gaining better estimation of wave properties through detection of wave crests based on high intensity values.

Figure 6: High intensity foam patches contained in a raw video image of the surf zone (Haas et al., 2004).

3.2 Procedure of the present study

Previous video-based coastal studies involved calculating wave properties preferably in the frequency domain by applying the FFT analysis methods to temporally dense wave image sequences. The FFT analysis of the image intensity signals is physically meaningful only when the intensity signals are a reasonable proxy of actual water levels. In those previous studies, band-pass filtering was only applied as a pre-processing step prior to the wave data analysis to remove high frequency noise or to exclude the influence of low frequency flow motions, since the original intensity signals do not contain wave breaking induced foam signals in most of their area of interest, i.e. outside the surf zone.

In contrast, the present image processing methodology is designed to remove the foam signals in the surf zone, strongly reforming the original intensity signals through a couple of image pre-processing steps due to very low signal-to-noise ratio. The pre-processed intensity signals are expected to have wave crest peaks exaggerated by the image processing methods and lose the natural form pattern of real wave signals, even though foam signals are removed successfully. The pre-processed intensity signals

cannot be used as a proxy for actual water level signals, since their cyclic signal shapes are strongly deformed and lose natural form of actual water level signals. This means that spectral coherence between the actual water level signals and the pre-processed intensity signals is not high. So, it is not reasonable to analyze the strongly pre-processed image intensity signals in the frequency domain. On the other hand, the pre-processed intensity signals indicate wave crest peak points outstandingly so that the wave crest peaks can be readily identified from the signals in time-series. For these reasons, this study will rather analyze wave data preferably in the time domain by tracking individual wave crest trajectories detected and extracted from the processed surf zone imagery.

Fig. 7 summarizes the procedure applied to the present study showing three main steps for nearshore bathymetry estimation derived from video imagery: 1) image processing, 2) wave property estimation, and 3) depth inversion model. The details of each step will be described in separate subsequent chapters.

This chapter describes the image processing for obtaining tracks of wave crests in the surf zone from recorded video image sequences. The purpose of the image processes is to obtain physically and quantitatively analyzable information on wave crest behaviors from the captured video. Thus, transformation of an image domain to a physical domain is essential among the image processes. Other image processes need to be determined base on their dependency on homogeneousness of spatial image quality and resolution whether they are conducted either before or after the transformation. This is because the image rectification process, which will be described later in this chapter, changes original spatial image quality, having better quality close to cameras and quality decrease with increase of the distance from cameras. Image processes such as image filtering requiring homogeneous spatial image resolution over the image domain should be desirably located prior to the image transformation process, since the image resolution becomes inhomogeneous over the space domain after the

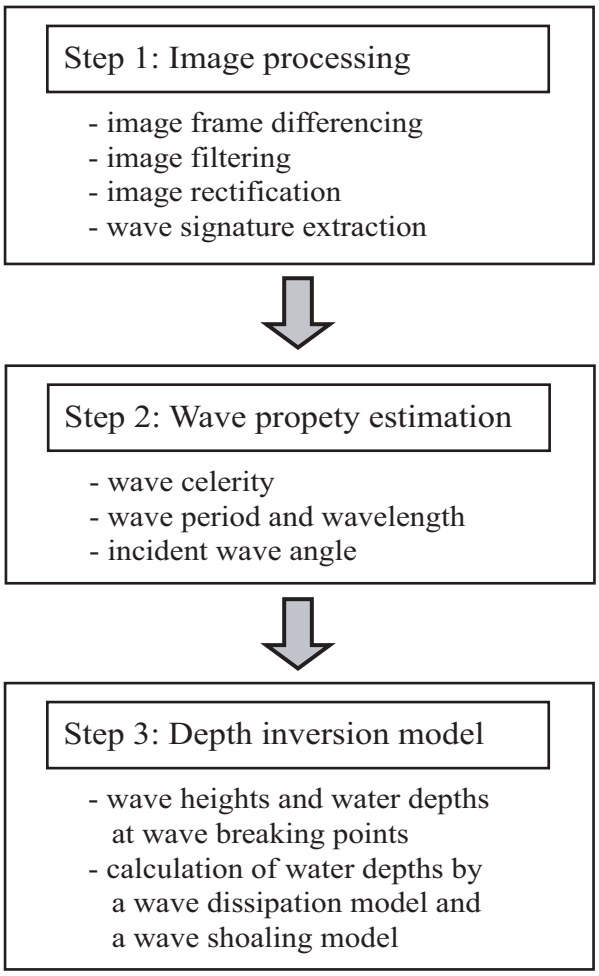

Figure 7: Steps of the present study for depth inversion using nearshore imagery.

image rectification. On the other hand, the processes for retrieving physical information such as generating a cross-shore timestack need to be conducted posterior to the transformation process.

The general procedure of the image analysis developed in this study can be summarized as follows: 1) association of subsequent image frames in the image domain and image filtering for foam removal in the frequency domain; 2) image rectification by transforming image frame coordinates to real world coordinates; 3) generation of the timestack of 1-D intensity time-series along the cross-shore; 4) extraction of individual wave crest tracks from the timestack. Fig. 8 illustrates the flowchart of the image processes along with data inputs and outputs which will be described in detail in subsequent subsections. This study uses video imagery, which will be described in detail later in this chapter, digitally recorded with 8-bit intensity depth ranging from 0 to 255. In Fig. 8, raw imagery is processed through two processing flow tracks. The flow track with solid lines aims to extract wave crest trajectories and estimate wave properties such as wave celerity, incident wave angle and wavelength from video imagery. The flow track with dotted lines is to extract wave period information from video imagery.

3.3 Image frame differencing and image filtering for foam removal

As shown in Fig. 6, both the wave crests and foam patches have high intensity values. One outstanding difference between them is that after wave breaking, wave crests still propagate at high speeds, while white foam remains drifting slowly in the direction of surface currents behind wave crests. Consequently, high intensity values caused by the foam last up to a couple of wave periods after instantaneous intensity peaks due to wave crests.

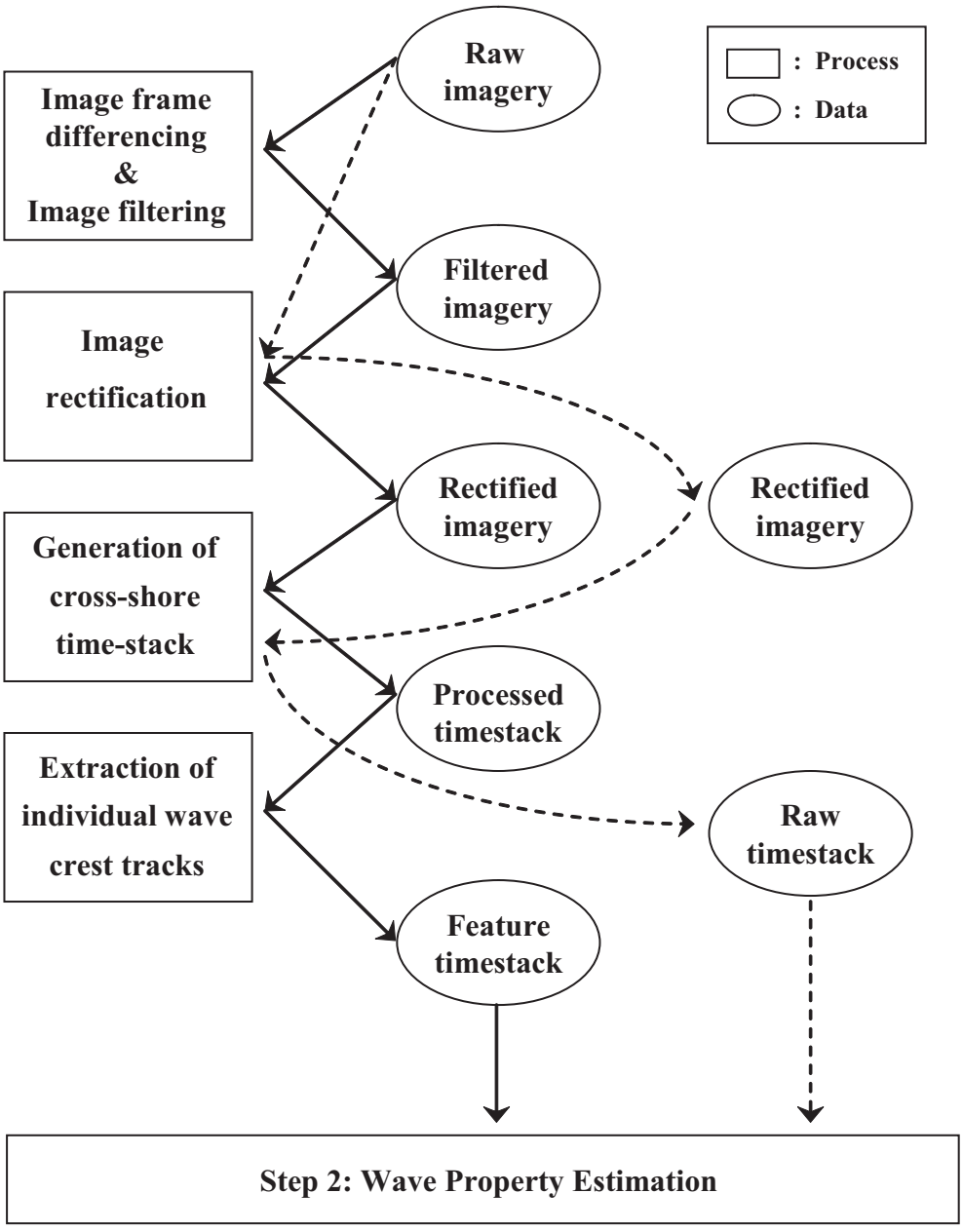

Figure 8: Flowchart of image processing procedures along with data inputs and outputs (solid line for identifying wave crest trajectries from video imagery, dotted line for extracting wave period information from video imagery).

3.3.1 Image frame differencing

Image frame differencing techniques to subtract the non-moving background from image sequences have been applied to various research fields such as visualization in robotics, automated road traffic evaluation, etc. Most of them employed frame differencing by subtracting the initial background image from each image frame, aiming to detect moving objects in the image frame. In the field of flow visualization research, Honkanen and Nobach (2005) associated double frames as an input set to Particle Image Velocimetry (PIV) analysis. Honkanen and Nobach (2005) simply subtracted one of the double frames from the other to remove non-moving or slow moving objects. Lippmann and Holman (1989) introduced frame differencing to quantify sand bar morphology in the nearshore. Lippmann and Holman (1989) subtracted image frames, separated by a time interval ($0.5 \sim 1.0$ seconds) to eliminate persistent signals by residual foam accumulation. Sapp (2006) investigated Rip current circulations in a laboratory by tracking drifters in image sequences subtracted by average images of every 50^{th} frame at the sampling rate of 15Hz to remove non-moving background and reduce the effects of periodic wave motions on tracking difters.

3.3.1.1 Determination of image frame sampling rate using PIV analysis

As applied and shown by Lippmann and Holman (1989), association of successive image frames by the image frame differencing technique is an effective method to reduce or remove effects of drifting foam in the breaking zone on wave signals. In the present study, in order to eliminate slowly moving foam and retain faster moving wave crest features in the image domain more effectively, an advanced image frame differencing method of sequential image frame association is developed. One important imaging parameter to be determined prior to the image frame differencing implementation is the image frame sampling rate, i.e. imaging time interval (dt), since the time

interval should be small enough to capture representative motion of objects in image sequence. For instance, the former video based coastal studies used significantly different image sampling rates depending on imaging conditions of camera-to-object distance: $1 \sim 2$ Hz for field imaging (Lippmann and Holman, 1989), and 15 Hz for laboratory imaging (Sapp, 2006). Since foam intensity signals in the image domain intend to be canceled by conducting the image frame association (i.e. image frame subtraction) with 2 successive images, a frame time interval that is too small will lose a great deal of moving wave crest features also. For this reason, the image sampling rate is determined such that displacements of wave crests per frame interval are to be about 2 $pixels/dt$. This intent intuitively confines speeds of residual foam to be almost 0 or less than 1 $pixel/dt$. Consequently, the image sampling rate (f_s) can be determined as:

$$f_s \left(= \frac{1}{dt} \right) \approx \frac{v_{pixel}}{2\, pixels} \tag{16}$$

where v_{pixel} = speed of wave crests in the image domain, and its unit is $pixels/sec$. In order to quantify speeds of wave crests required for determining the image frame sampling rate, the PIV analysis technique is applied to raw image sequences in the image frame coordinates. Speeds of wave crests in the image frame coordinates tend to be seemingly consistent along the cross-shore transects over the image domain, since wave crests having smaller celerity near the shoreline are close to cameras while wave crests having larger celerity near the offshore are far from camera locations. However, speeds of wave crests in the real world coordinates vary significantly along the cross-shore transects. These facts indicate that the frame differencing in the image frame coordinates is more practical.

Digital, video-based PIV studies have been applied to near-shore processes, in particular to investigate two-dimensional cross-sections of coherent flow structures

of water waves under water surface including breaking waves at laboratory scale (Chang and Liu, 1998; Dibajnia, 2002). The PIV method had originally evolved from laser speckle velocimetry. The classical laboratory applications confine a plane in the water body with a laser light-sheet, and use discrete flow seeding particles. Recently, the PIV method has been applied to non-discrete image patterns of seeded or non-seeded water wave flow fields (Fritz, 2002; Holland et al., 2001). In particular, Holland et al. (2001) applied the PIV method to non-seeded natural coastal images to quantify the horizontal flow structure of swash. Holland et al. (2001) tracked natural image textures resulting from foam patterns in sub-windows with the PIV technique, instead of artificially seeded image textures. Similarly, the cross-correlation based PIV analysis is applied to sequential near-shore ocean surface video wave images to estimate speed of wave crest patches generally having high intensity values in this study.

PIV is a 2-D (image window) auto- or cross-correlation based measurement technique which uses multiple images of seeded flow fields in a confined plane to measure the two components of the flow velocities in the 2-D confined plane (Raffel et al. 1998). Flow fields captured in the video image sequence are assumed to be planar during the entire analysis process. The instantaneous planar velocity vector fields can be computed with a cross-correlation based adaptive multi-pass algorithm to increase spatial resolution and dynamic range of the computed flow vectors (Scarano and Riethmuller 2000). In this study, a commercial PIV software (LaVision DaVis PIV package) is used to conduct the PIV analysis using the adaptive multi-pass algorithm.

Nearshore video imaging experiments at Myrtle Beach in Dec., 2003 (Haas et al., 2004) of which datasets (hereafter, referred to as 2003 Myrtle video datasets) are used in the present study were conducted with two types of camera viewing conditions as shown in Fig. 9(a)(c): (a) oblique-top and (c) oblique-side views. The Myrtle video datasets were digitally recorded at the NTSC standard of 30 Hz with a 8-bit intensity

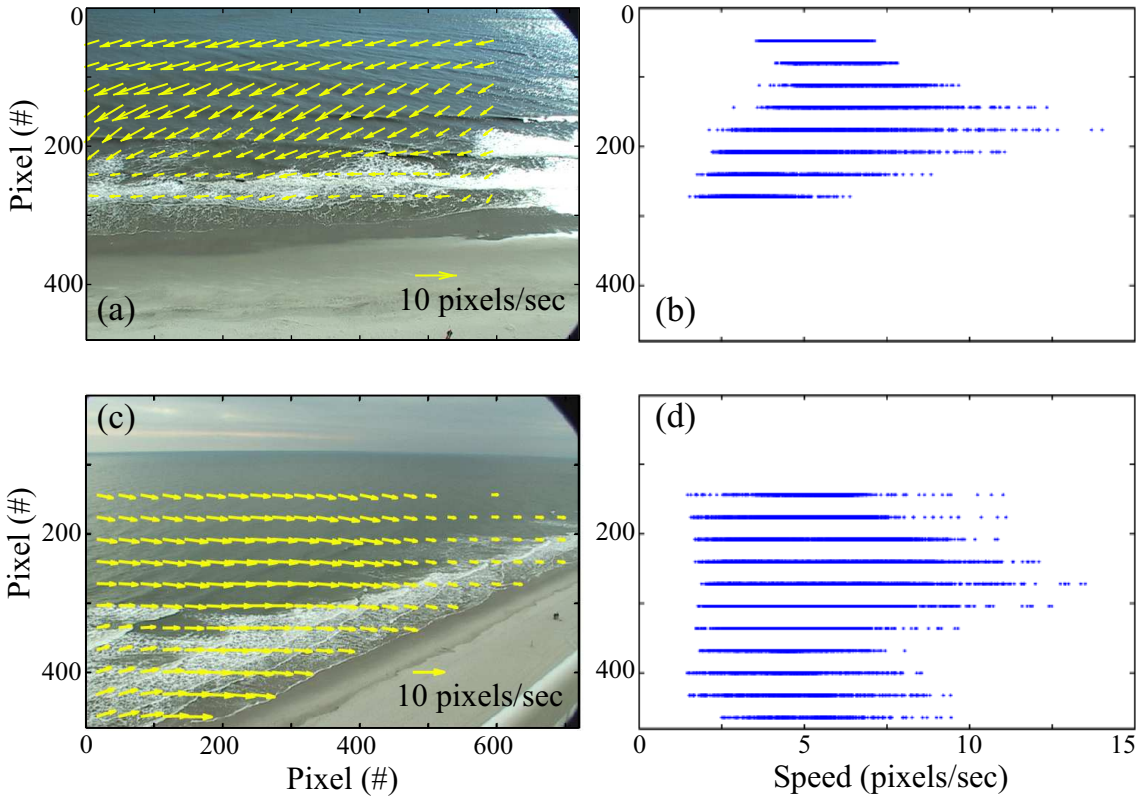

Figure 9: Speeds of wave crests computed by the PIV analysis in the image coordinates: (a) an instantaneous velocity vector field in the oblique-top view image frame, (b) distribution of wave crest speeds accumulated during a 30-sec timespan of case (a), (c) an instantaneous velocity vector field in the oblique-side view image frame, (d) distribution of wave crest speeds accumulated during a 30-sec time-span of case (c).

depth (intensity range: $0 \sim 255$ counts). Two wave image datasets were selected from oblique-top-view and oblique-side-view video recordings respectively to be inputs to PIV analysis. The oblique-top-view dataset is selected with a 30-second time span from video imagery recorded on Dec. 11, 2003 on which the weather was clean and sunny. The oblique-side-view dataset is also selected with the same time span from Dec. 13, 2003, a day which was dark and cloudy.

Prior to the PIV application, the surface flow fields are isolated from stationary image parts in the image domain by digital masking, since the stationary parts such as the beach and horizon causes bias error in the correlation analysis. Thereafter, a set

of two sequential images are input to the PIV software, and the instantaneous velocity vectors are computed with the cross-correlation based adaptive multi-pass algorithm. In this study, the final interrogation cell size of 64×64 pixels ($Height \times Width$) (hereafter, referred to ($H \times W$) or omitted) with 50% overlapping is used. The interrogation window size is determined to be equivalent to the length scale of the wavelengths (in pixels) of incoming waves in the image domain, intending to retain approximately one wave crest over the interrogation window. The wavelengths in the image domain for the two datasets were manually determined as less than 60 pixels.

Fig. 9 presents instantaneous vector fields computed by the PIV analysis and distributions of the computed speeds accumulated during the 30-second time span with respect to y-axis of the image coordinates. Speeds of wave crests at a fixed point in the image domain are obtained by calculating magnitudes of velocity vectors. Both speed distributions in Fig. 9(b)(d) show similar speed range of roughly $2 \sim 13$ pixels/sec having their mean values as (b) 5.42 pixels/sec and (d) 6.87 pixels/sec. Thus, based on the mean values of wave crest speeds, image frame sampling rates of the both cases are determined mathematically using Eq. 16 as 2.71 Hz and 3.44 Hz respectively. The both sampling rates round to the same nearest integer frequency of 3 Hz. This suggests that 2003 Myrtle video datasets can be down-sampled to the integer frequency of 3 Hz for image frame differencing purposes. Some changes of water depth are not expected to cause significant changes of wave phase speeds in most of the area of interest. In addition, the camera-to-object (i.e. the surf zone) distances didn't change during the video experiments. For those reasons, the image sampling rate is chosen as 3 Hz for 2003 Myrtle video datasets in this study.

3.3.1.2 Determination of image frame association

Once the image sampling rate is selected such that wave crests can be displaced at least 2 pixels or so during the frame interval, most of residual foam may stay at the same locations and some of it may eventually move 1 pixel as mentioned before. Association of two consecutive images by subtracting intensities from the first frame from intensities from the second one will cancel signals of non-moving foam and background. Wave breaking-induced foam captured in image sequences usually acts not like a particle but like a patch. So, averaging two consecutive images is expected to enhance foam configuration in the image frame.

Thus, the frame differencing is designed to subtract from a target image the averaged of 2 successive images in its neighborhood in this study. Consequently, it removes the non-moving background and the foam patches more clearly than the case of Lippmann and Holman's application, retaining moving features in the image frame. Since foam lags behind in terms of wave propagation while a wave crest tumbled down in the surf zone marches in the front, the method of backward differencing, instead of central or forward differencing, is applied:

$$I_k^{new}(i,j) = I_k(i,j) - \frac{1}{2}\sum_{n=k-2}^{n=k-1} I_n(i,j) + K \tag{17}$$

where I_k = pixel intensity of k^{th} image; I_k^{new} = pixel intensity of k^{th} image after frame differencing; (i,j) = pixel coordinates in an image; K = constant for image brightness enhancement. Intensity depth of video images is 8-bit ($0 \sim 255$), and subtraction of image frames causes negative intensity values having the mean of subtracted image frame intensities as almost 0. Thus, K is set to be 127 in this study. Fig. 11(a)(b) presents an original image and its frame-differenced image by Eq. 17.

3.3.2 Image filtering in 2-D frequency domain

Although the frame differencing is applied, frame differenced images still contain spot-like residual noise. So, further image filtering is required to smooth out the residual spot noise. Signals of the spot-like noise can be regarded as high frequency in the frequency domain having their wavelengths of up to several pixels in the spatial domain. Thus, a low-pass filtering is applied to the frame differenced image sequence in this study.

Image filtering in the frequency domain is conducted through 2-D Fourier transform as shown in Fig. 10(a) which presents the concept of image filtering operations in the frequency domain. Fig. 10(b) shows an example of ideal low-pass filter design. The product of a Fourier-transformed 2-D spectrum, $F(u, v)$ where $(u, v) =$ coordinates in the frequency domain, and a designed low-pass filter function $H(u, v)$ attenuates high frequency components of the frequency domain, having low frequencies unchanged. In circularly oriented filters, the cutoff frequency remains constant in all directions. However, the constant cutoff frequency is not reasonable to be applied to the frame-differenced wave images, since those images have strong directionalities of the wave crest features in them.

Fig. 11 presents the 2D Fourier transform of sub-window in a frame-differenced wave image to develop a directional (or elliptic) low-pass filter design. Retained wave crest features of high intensities in frame-differenced images are directionally elongated as shown in Fig. 11(b)(c). Consequently, 2D Fourier spectra of the frame-differenced images show higher energy frequency components in one direction (Fig. 11(d)). In the low-pass filter design for this case, if a constant cutoff frequency is set in all directions as in circularly oriented filters, high frequency components contributing to high intensity wave crest features will also be removed. However, elliptically oriented filters have varying cutoff frequencies at different angles, leaving low to high frequency components unchanged in the direction of high spectrum energy

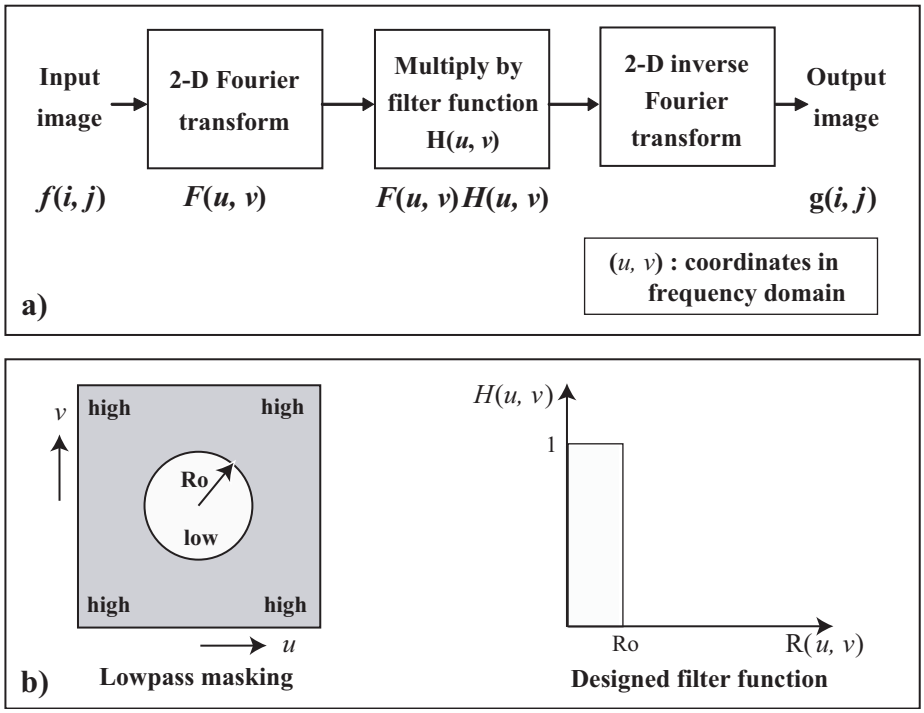

Figure 10: Image filtering operations in the frequency domain: (a) basic steps of frequency domain image filtering, (b) ideal low-pass filter design.

components in the frequency domain. In this study, the Butterworth filter as an elliptic low-pass filter is used:

$$H(u,v) = \frac{1}{1 + \left[\left(\frac{u \cdot cos\theta + v \cdot sin\theta}{f_M}\right)^2 + \left(\frac{-u \cdot cos\theta + v \cdot sin\theta}{f_m}\right)^2\right]^n} \tag{18}$$

where θ = angle of the major axis, f_M = cutoff frequency for the major axis, f_m = cutoff frequency for the minor axis, and n is filtering order. The angle of the major axis, θ, is determined from the 2-D Fourier spectrum. Frequency components with high energy above an energy threshold are isolated in the frequency domain, and linear regression is applied to compute the angle. Throughout the present study, the sub-window size of 64×64 pixels is used to interrogate and filter local area in the image domain, and the energy threshold is set to be 0.85 in the normalized 2D

Fourier spectrum by the maximum energy value. As applied to determine the sub-window of PIV analysis for computing speeds of wave crests in the image domain, the interrogation window size of the direction low-pass image filter is also determined to be equivalent to the length scale of the wavelengths (in pixels) of incoming waves in the image domain. This intent retains approximately one wave crest over the interrogation window. In addition, f_M, f_m, and n are empirically selected to be 0.3, 0.07, and 3 respectively. Fig. 11(e) presents the visualized image of the Butterworth filter function designed for filtering the sub-window image of (c) using the determined Butterworth filter parameters, and its filtering result is shown in Fig. 11(f).

In order to filter the entire image domain, sub-windows with the size of 64×64 pixels (hereafter, referred to as the local interrogation window) are moved with 50% overlapping, thereby taking the centered square portion with the size of 32×32 pixels as valid filtering area. If correlation of the isolated energy components, (u, v), in the 2-D Fourier spectrum to obtain the angle of the major axis in the frequency domain is less than 0.5, the angle of the major axis is substituted with the angle (hereafter, referred to as the general incident angle, θ_g) computed using a larger sub-window size of 256×256 pixels in Fig. 11(b). The poor correlation of the isolated energy components can be caused when the local interrogation window is located in the area of weak intensity signals such as offshore or beach. In addition, if the local angle is deviated beyond $\theta_g \pm 15^\circ$, it is also replaced by θ_g. A resulting image after the Butterworth low-pass filtering is showin in Fig. 11(g).

3.4 Generation of cross-shore image timestack

In order to obtain physically analyzable quantities of wave crest behaviors in the wave propagation direction from the processed wave image sequences, the processed sequences in the image domain go through: 1) image rectification to transform the

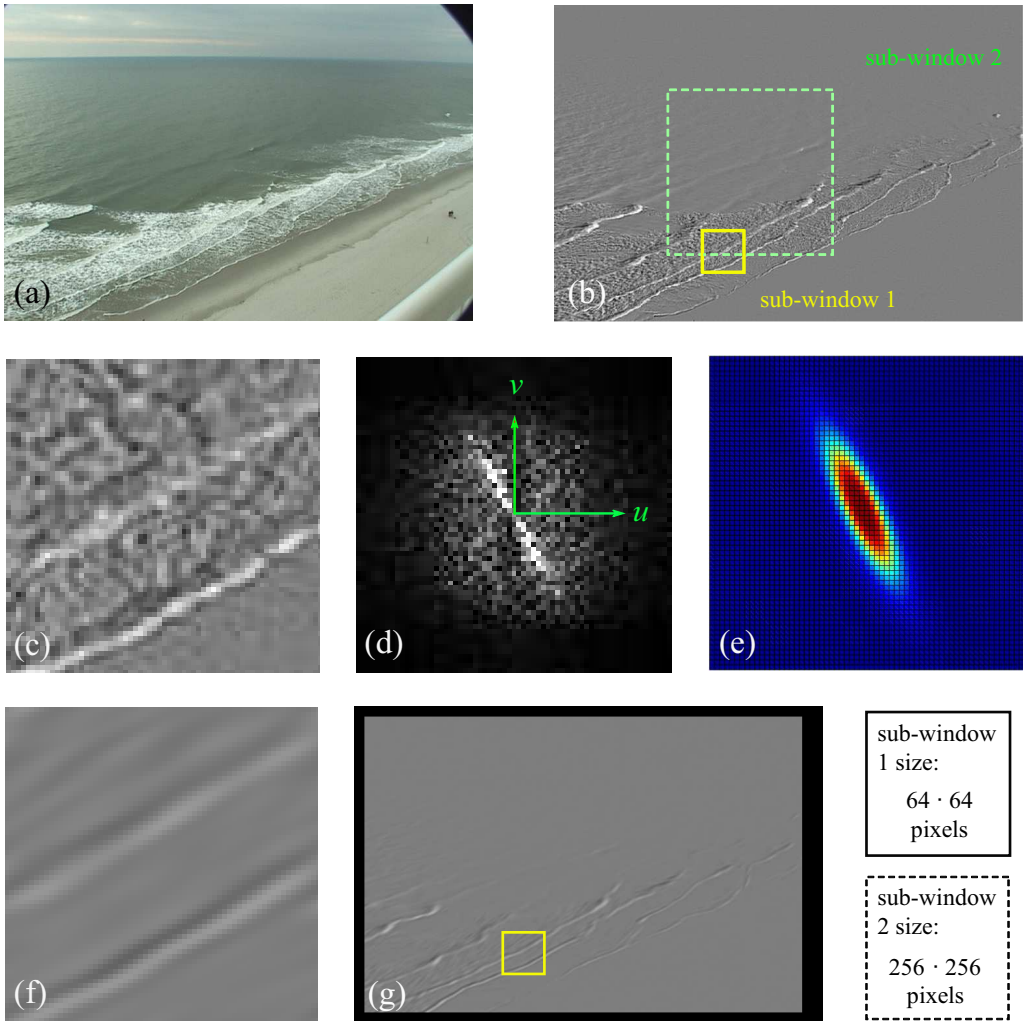

Figure 11: 2D Fourier transform of sub-window in a frame-differenced image: (a) original image, (b) frame-differenced image, (c) sub-window image of 64 × 64 pixel size in (b), (d) 2-D Fourier spectrum of (c), (e) the Butterworth filter function shown as an image, (f) filtered image of (c), (g) filtered image of (b).

image frame coordinates to the real-world coordinates, and 2) the process of the cross-shore image timestack generation.

3.4.1 Image rectification

In order to transform video frame coordinates to real world coordinates, the Direct Linear Transformation (DLT) method by Holland et al. (1997) is used. The transformation procedure includes two types of model calibration: compensation for intrinsic distortion by camera properties and calibration for geometric distortion by measurement set-up.

The camera lens distortion calibration is conducted at a laboratory by mounting a rectilinear grid plate perpendicular to the camera lens. Thereafter, the camera lens distortion is quantified by comparing the captured rectilinear image with the actual rectilinear grid plate. Holland et al. (1997) suggested the camera lens distortion as a form of radial distortion (Δr) by a two-coefficient odd-order polynomial:

$$\Delta r = k_1 r^3 + k_2 r \tag{19}$$

where r is the radius in pixels along radial line from the center of the rectilinear image, and k_1 and k_2 are model-fit parameters. k_1 and k_2 are determined by fitting Eq. 19 to the radial distortion measured using the rectilinear grid plate and its corresponding rectilinear image captured. Fig. 12 presents the measured radial distortion of video camera lens used in this study and the two-coefficient odd-order polynomial optimized from the radial distortion measurements. The camera lens distortion is compensated over the captured image domain using the determined two-coefficient odd-order polynomial.

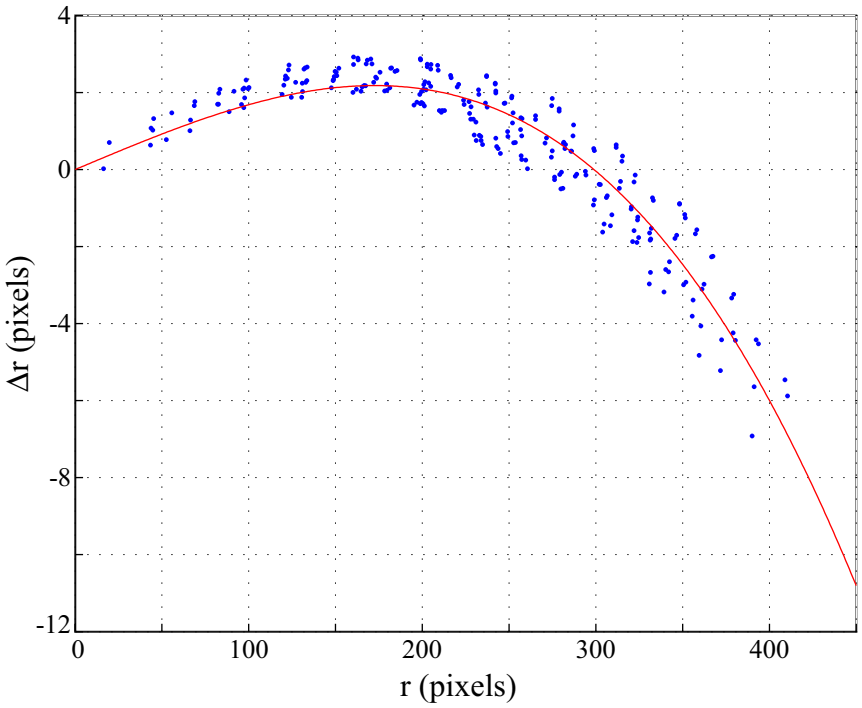

Figure 12: Radial distortion of video camera lens used in this study and the best fit odd-order polynomial (Haas et al., 2004).

The transformation of the image to world coordinates is defined by the DLT coefficients. The DLT coefficients are linearized parameters of the collinear relationship between pair of each image coordinates and their corresponding real-world coordinates. This geometric calibration is conducted under the image condition that intrinsic distortion of the camera lens is free, and a linear relationship between image and real-world coordinates can be expressed using the DLT coefficients as follows:

$$i = \frac{L_1 x + L_2 y + L_3 z + L_4}{L_9 x + L_{10} y + L_{11} z + 1}, \; j = \frac{L_5 x + L_6 y + L_7 z + L_8}{L_9 x + L_{10} y + L_{11} z + 1} \tag{20}$$

where (i, j) = image pixel coordinates, (x, y, z) = real world coordinates, and $L_k (k = 1, \cdots, 11)$ = the DLT coefficients.

The DLT coefficients are determined from Eq. 20 by using a least squares method and ground control points (at least six points) surveyed in both the field (x, y, z) and

the image (i, j) domain. Fig. 13 presents the ground control points (GCP) surveyed in the field and identified in the image domain in a dataset selected from the 2003 Myrtle video data for determining the DLT coefficients.

The transformation of image coordinates to world coordinates is also performed using Eq. 20 with the pre-determined DLT coefficients. Since the system of equations is underdetermined (two equations with three unknowns), elevation z in the sea in real coordinates needs to be constrained as zero for a mean sea level. The elevations of the beach are also constrained by the best-fit planar surface applied to the survey data of the beach topography. In Fig. 13(b), the predicted locations of the GCPs identified in the image frame after geometric calibration using Eq. 20 are presented, showing a good agreement between the measured and the predicted GCPs. In this study, the horizontal, i.e. (x, y), origin of the real-world coordinates in the rectified domain is fixed for all datasets selected from the 2003 Myrtle Beach data, which will be described later in this chapter, as the same origin established for beach morphological surveys. The vertical (i.e. z) origin of the real-world coordinates in the rectified domain is set to be the mean water level computed from the measured pressure head data of each dataset.

3.4.2 Cross-shore timestack generation

In order to investigate wave properties and water depths in the direction of wave propagation, the present video technique involves collecting time-series of pixel intensity at a pixel array taken from the rectified imagery along a cross-shore transect, yielding a cross-shore timestack (space-time image as shown in Fig. 3). This cross-shore timestack illustrates the variations of pixel intensity in time at each cross-shore location.

In the present study, a set of two cross-shore timestacks is generated from both

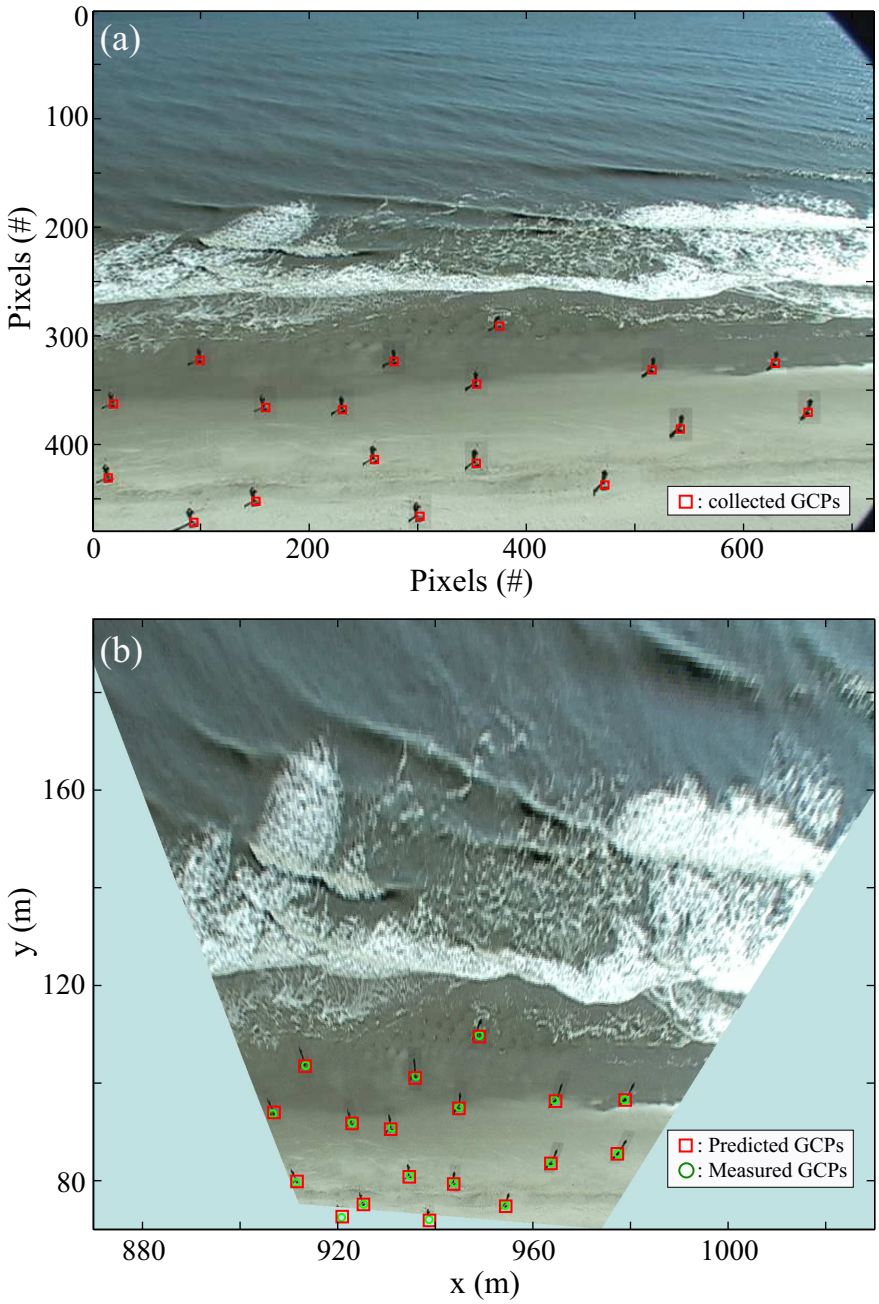

Figure 13: Ground control points surveyed in both the image domain and the physical space (Haas et al., 2004): (a) the collected GCP locations in the image domain, (b) the measured and the predicted GCPs in the real-world coordinates established based on the origin for beach morphological surveys during the 2003 Myrtle Beach data collections (hereafter, the cross-shore distance in figures is referenced to this origin).

the rectified raw and the processed image sequences. The pixel intensity time-series of the cross-shore transect array are sampled directly from the original image domain with subpixel accuracy using the method described by Chickadel et al. (2003). Fig. 14 shows segmental cross-shore timestacks collected from the Myrtle video captured on Dec. 15, 2003. Fig. 14(b) is a cross-shore timestack of the raw image sequence, and Fig. 14(c) is its paired timestack of the processed image sequence. The symbols y and t in Fig. 14 denote cross-shore distance and time within the image sequence respectively. The processed image timestack is used to extract individual wave crest tracks. The raw image timestack is used for estimating wave periods and detecting wave breaking points through association with the extracted wave crest features.

Throughout the present study, a video dataset having 6150 image frames is down-sampled to 3 Hz from the 2003 Myrtle video datasets for a depth inversion event, thereby generating a cross-shore timestack of which time-length is 2050 seconds (34.17 minutes). Four different video datasets selected from the 2003 Myrtle video datasets are used in this study. The selection of the four datasets will be described later in the subsection named Experimental datasets in this chapter. The physical resolution in the cross-shore direction in the time-stacks is selected as 0.1 m, since the resolution in the area of the shoreline captured in the video image sequence is observed to be order of 10 cm.

3.5 Extraction of wave crest tracks

Aiming to estimate wave speeds of individual shoreward wave crests, features of individual wave crest tracks are to be extracted in the processed image cross-shore timestacks as shown in Fig. 14(c).

Previously, Catalan (2005) generated mean removed cross-shore timestacks from video imagery captured in the 1-D wave flume at Oregon State University. Catalan

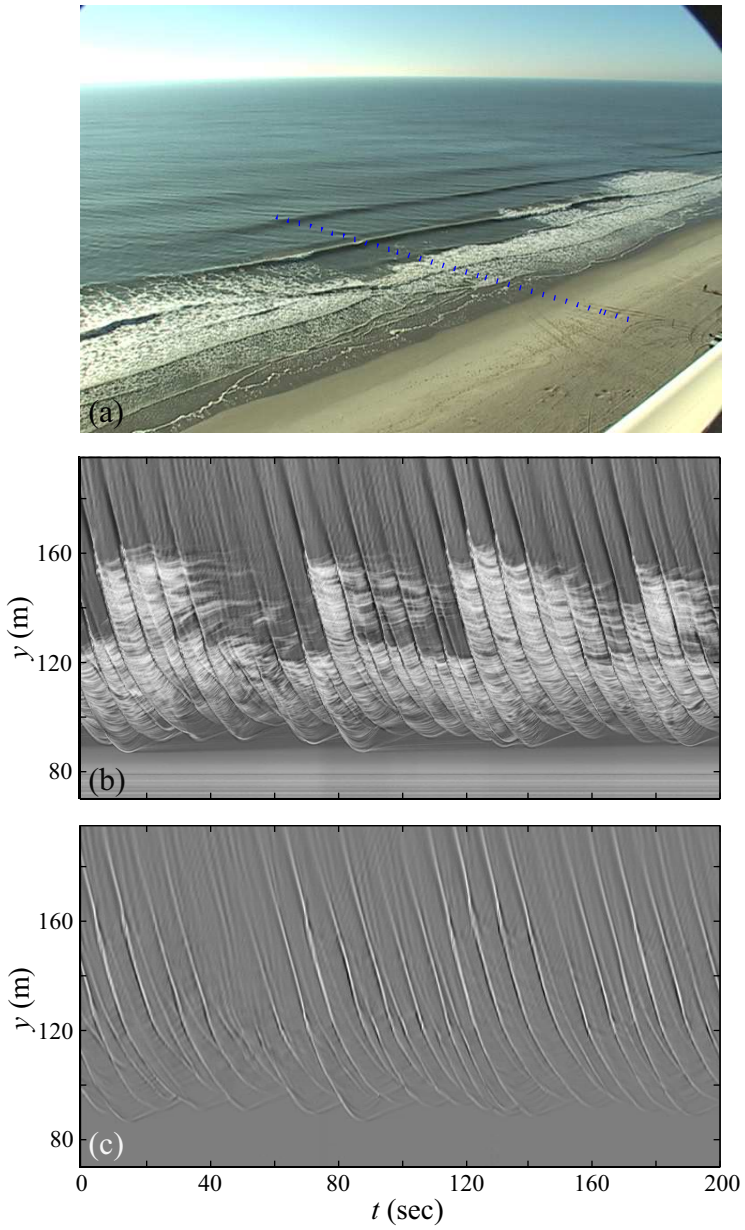

Figure 14: Segmental timestacks from Myrtle video captured on Dec. 13, 2003 (Haas et al., 2004): (a) the cross-shore transect for generating timestacks in the original image frame, (b) raw image timestack, (c) processed image timestack.

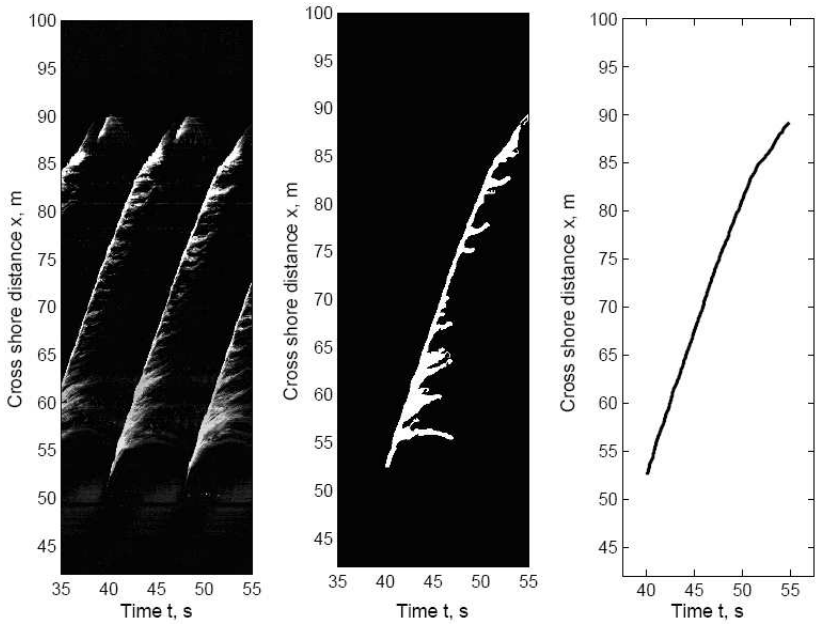

Figure 15: Detection of a wave front trajectory from a mean removed timestack: original timestack (left), a mean removed and isolated wave (middle), and the detected wave front trajectory (right) (Catalan, 2005).

(2005) extracted wave front trajectory from a binary image of the mean-removed timestack using a zero-upcrossing based edge detection method as shown in Fig. 15. Catalan (2005) used only regular wave conditions in which patterns of wave front trajectories are uniform. Catalan (2005) could easily isolate individual waves, since an incoming wave was not under influence of the persistent foam created by the previous wave.

In the nearshore field, however, the approach of Catalan (2005) is not well suited to isolate individual waves. Some incoming waves merge in the inner surf zone as shown in Fig. 14(b), and the tracks of wave crests in the raw image timestacks are hardly distinguished from the white foam patches generated by previous breaking waves, having non-uniform shape patterns of each individual wave crest trajectories. In contrast, the cross-shore image timestacks processed by the present image processing methods clearly reveal individual wave crest trajectories approaching the shoreline, having no foam patches, as shown in Fig. 14(c).

In order to detect and extract the non-uniform wave crest trajectories in the processed timestacks, a more flexible approach using a line detection method than that of Catalan (2005) is applied to the processed image timestacks. The general pattern of wave crest trajectories in the nearshore shows curved shapes as shown in Fig. 14(c). If a segment of the wave crest tracks is taken over a distance short enough, however, it can be assumed to be a straight line. Being consistent with the assumption, eye-witnessed wave crest tracks in Fig. 14(c) have local line shapes in the outer surf zone.

3.5.1 Wave crest feature detection by Radon transform

In order to detect and extract wave crest tracks having non-uniform patterns, the Radon transform is applied. The Radon transform implementation converts lines in the 2-D images into points having high energy peaks, using two line parameters, ρ and Θ, in the Radon transformed domain. Fig. 16 describes the Radon transform and the two line parameters. The line is expressed in the form of $\rho = i \times cos\Theta + j \times sin\Theta$, and the two parameters Θ and ρ denote the angle and the distance normal to the lines from the origin of the coordinates in the image domain respectively. The Radon transformed energy of the line, $R(\rho, \Theta)$, is computed by the line integral through the image, $f(i, j)$, in which the integral projection is positioned corresponding to the values of ρ and Θ:

$$R(\rho, \Theta) = \int_{-\infty}^{\infty} f\left(\rho \cdot cos\Theta - s \cdot sin\Theta,\ \rho \cdot sin\Theta + s \cdot cos\Theta\right) ds \tag{21}$$

where $s = -i \times sin\Theta + j \times cos\Theta$, and denotes the axis of the line integral normal to the axis of ρ. Inversely, if the values of ρ and Θ of the highest energy peak is obtained in the Radon transformed domain, the line corresponding to the two line parameters can be extracted in the original image domain.

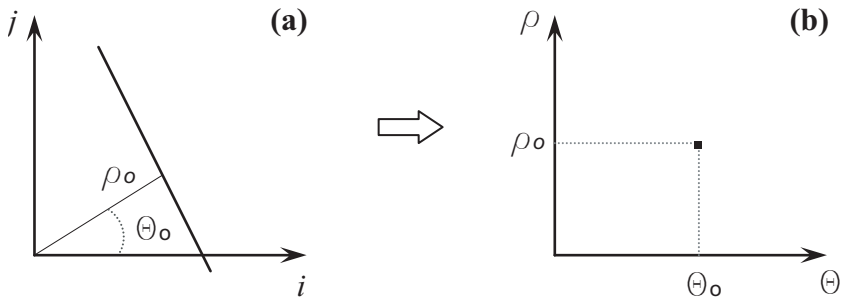

Figure 16: Concept of Radon transform: (a) a line in a image, (b) a point having the highest energy peak in the Radon transformed domain.

The application of the Radon transform to detect wave crest features in the processed timestack is illustrated in Fig. 17. The size of the interrogation window (hereafter, referred to as a crest tracking sub-window) is selected to be 50 × 50 pixels of which physical dimensions are 5 m × 16.67 s ($H \times W$). Image pixel coordinates of timestacks are denoted x_p for the t-axis and y_p for the y-axis. The reason for selecting the crest tracking sub-window size as 50 × 50 pixels will be discussed in Chapter VI by investigating the effects of different crest tracking sub-window sizes on wave crest identification.

Fig. 17(c) and (d) present an image in the crest tracking sub-window shown in the processed timestack (a) and its Radon transformed energy spectrum respectively. Prior to the Radon transform, the intensity of the crest tracking sub-window image is subtracted by the image brightness enhancement constant, $K = 127$. By this subtraction, the energy values in the Radon transformed spectrum corresponding to wave crest trajectory lines tend to be positive, while the energy values corresponding to wave troughs tend to be negative. The highest energy peak in the Radon transformed spectrum provides its corresponding two line parameters, ρ and Θ, to detect line feature of a wave crest track in the crest tracking sub-window.

Tracking of the wave crest trajectories starts at the offshore boundary in the processed image timestack. Offshore starting points of the wave crest tracks in Fig.

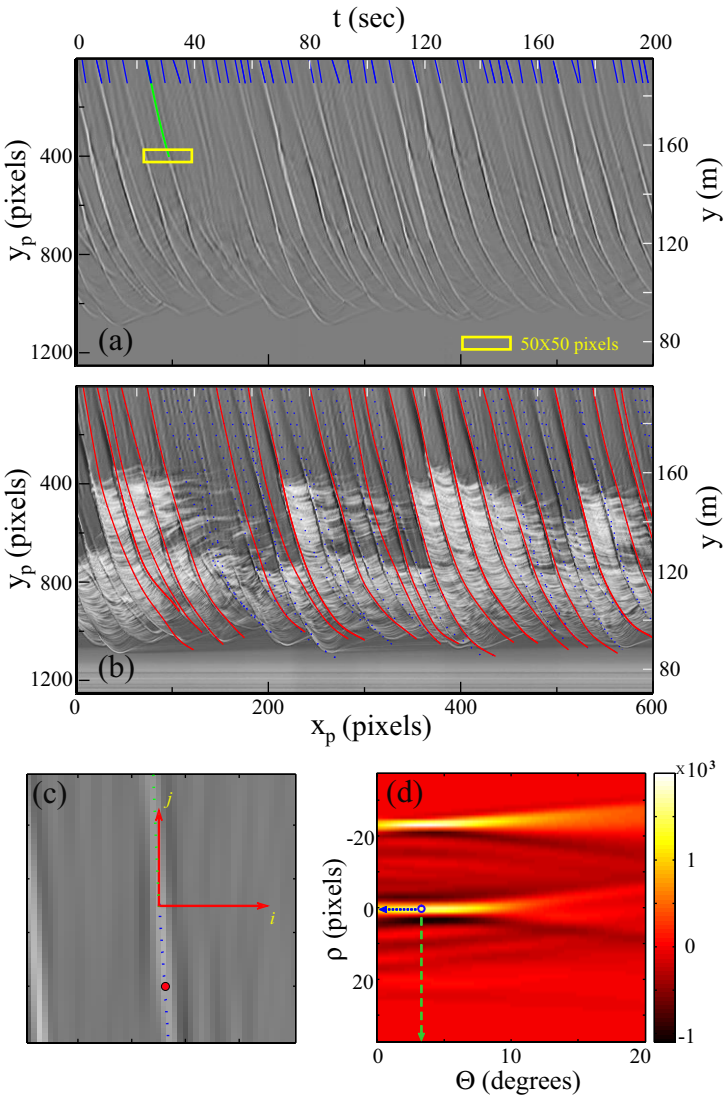

Figure 17: Application of the Radon transform to the processed timestack: (a) processed image timestack with (blue lines 100-pixel-long) starting points of wave crest tracking, (green line) partially extracted wave crest track, and (yellow box) crest tracking interrogation window, (b) extracted wave crest tracks in the raw image timestack with (blue dot line) filtered out tracks, and (red lines) retained tracks after filtering, (c) image of crest tracking interrogation window shown in (a) with (green dot line) old line, (blue dot line) newly detected line, and (closed red circle) new origin of the interrogation window center, (d) result of the Radon transform of (c) with (opened blue circle) high energy peak for detecting the new line in (c).

17(a) with 100-pixel-long blue lines are determined by applying the Radon transform with an other sub-window size of 100×180 pixels ($H \times W$) (hereafter, referred to initial line detection sub-window), sliding the initial line detection sub-window in the direction of the positive x-axis with 10% overlapping. Peak energy values in the Radon transformed spectrum to detect the initial lines are confined to be above 100 (counts). Throughout this study, incident wave period range of $3 \sim 15$ seconds is assumed. In addition, the number of initial lines in the offshore boundary is selected to be the smaller of either 683 or the number of lines detected by sliding the initial line detection sub-window with the threshold value of high peak energy. The number 683 is selected based on the time-length of the video datasets divided by the lowest cut-off wave period, i.e. $683 = 2050 \text{ s} \div 3 \text{ s}$. If the number of lines detected by the initial line detection window is larger than 683, the initial lines with the first highest 683 peak energy values are used as starting points of the wave crest tracks.

In order to track individual wave crest trajectories starting from the offshore boundary, the center (the origin) of the crest tracking sub-window is located at the ending point of an initial offshore line. The intensity matrix within the crest tracking sub-window is input to the Radon transform to obtain the next new line segment as shown in Fig. 17(c)(d). The high peak energy components of ρ and Θ for detecting the new line are obtained such that the ρ value is in the range of $-3 \sim 3$ pixels with regard to ρ-axis and the Θ value is within $\Theta_\circ \pm 3.5^\circ$ in terms of Θ-axis in the Radon transformed domain where $\Theta_\circ$ is the Θ value of the previous line detection. The newly detected line in the crest tracking sub-window is 25 pixel-long in height, i.e. the length of lower half of the crest tracking sub-window. The first half (12 pixel-long) of the new line (25 pixel-long) from the present origin (i.e. the center) of the sub-window is taken as a valid new track, and the middle point of the new line substitutes the present origin of the sub-window center as the next new origin as shown in Fig. 17(c) with the closed red circle.

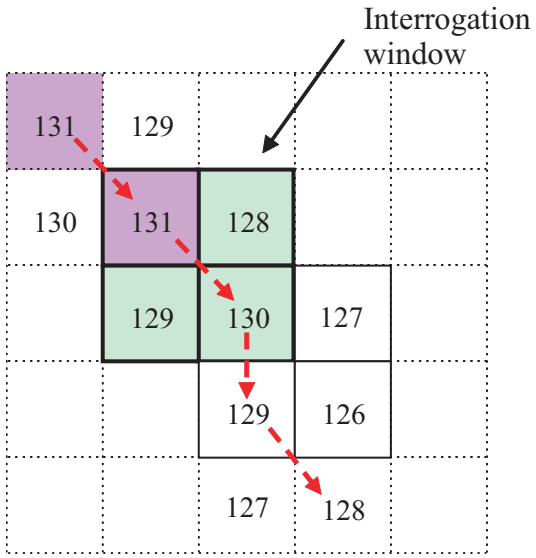

Figure 18: Tracking highest intensity values within the movable interrogation window (number in each cell represents image intensity).

As the wave crest tracks approach the shoreline, the angle Θ is getting larger and changes rapidly within the crest tracking sub-window of Radon transform. So, if the angle Θ is larger than 15°, the crest tracking sub-window is substituted by a smaller interrogation sub-window of 2×2 pixel size. The wave crest tracks continue to be extracted by tracking pixels of highest intensity values within the movable interrogation sub-window on the processed image timestacks. Once the upper left pixel of the interrogation window is placed at the ending point of a wave crest track extracted by the Radon transform, the location of the highest intensity value in the rest 3 pixels in the sub-window will be selected as the next location of the upper left pixel of the sub-window. Thereby, the sub-window will be shifted such that the upper left pixel of the sub-window is located at the selected new location as illustrated in Fig. 18. The rest of the wave crest track is extracted by following the newly detected highest intensity locations up to the shoreline having the intensity values less than 127.

The individual wave crest tracks extracted using the crest tracking sub-window

consist of partial lines 12 pixel-long (physically 1.2m-long) in the y_p-axis. This line segmentation of the wave crest tracks can cause discontinuity of physical quantities estimated from the partial line segments. Since the discontinuity is not likely to be in the physical world, the discontinuity points are smoothed out and interpolated using a cubic smoothing spline method (Eubank, 1988).

3.5.2 Removal of erroneous tracks

The wave crest tracks are extracted from the processed image timestacks by detecting and tracing high intensity pixels in the interrogation windows. The foam patches in the breaking zone tend to be filtered out through the image processing, but are not completely removed. False tracking of wave crest trajectories can be caused by the retained foam signals having high intensity values in the processed image timestacks. In addition, the offshore starting points of wave crest tracking are detected through the Radon transform with the transformed energy threshold. The number of the tracking starting points in the offshore is set to accept all possible cases of incident waves, based on the cut-off high wave frequency. It may also cause unrealistic offshore starting points and wave crest tracks, since all of incident waves are not discernable in a video image sequence. Hence, erroneous wave crest tracks need to be filtered out in order to reduce errors of the physical quantities estimated from them.

Erroneous wave crest tracks are filtered out through two steps: high intensity validation of the extracted tracks and pattern repeatability validation of the extracted track shapes. The first step validates intensity of the extracted wave crest tracks if their intensity is higher than their background during their propagation toward the shoreline or not. If not, that wave crest track is removed. The second step tests if the extracted track shape is found repeatedly over the dataset time-span, and accepts repeatedly found shapes of the extracted tracks.

3.5.2.1 High intensity validation of extracted tracks

The offshore initial lines for individual wave crest tracking are extracted using the Radon transform, having a length of 100 pixels long at the offshore boundary. The Radon transform detects line features having higher intensity in the processed image timestacks, and wave crest tracking starts from the initial lines. The realistic wave crests are assumed to maintain higher intensity during their propagation toward the shoreline, compared to their front and rear faces. This assumption is used to confirm the initial lines as actual starting points and remove erroneous wave crest tracks.

Fig. 19 shows removal of the erroneous wave crest tracks through the high intensity validation. Intensity profiles of wave crests in the cross-shore direction are obtained by following the extracted wave trajectories in the processed image timestack as shown in Fig. 19(a) with blue and red lines. In the same way, pink dotted and blue dotted lines in Fig. 19(a) provide intensity profiles of the crest front and rear faces respectively. The pink dotted lines, i.e. front face tracks, are obtained by translating the crest tracks in the negative direction of the x_p-axis as much as $(x_p - 4)$ or $(t - 4 \cdot dt)$ in terms of the time (t) axis. By shifting the crest tracks $(x_p + 4)$ in the x_p-axis, the blue dotted lines, i.e. front rear tracks, are obtained.

Fig. 19(b) and (c) present intensity profiles of a realistic and an erroneous wave crest tracks, respectively. The intensity profile of the realistic wave crest (red line) in Fig. 19(b) is higher than those of the wave crest and rear face trajectories in the offshore area within 200 pixel-length from the offshore boundary. However, the erroneous crest track (blue line) in Fig. 19(c) has lower intensity values at some points than those of the wave crest and rear face trajectories in the offshore area within 200 pixel-length from the offshore boundary. For this step filtering, comparison between the wave crest intensity profile and the intensity profiles of the wave crest and rear

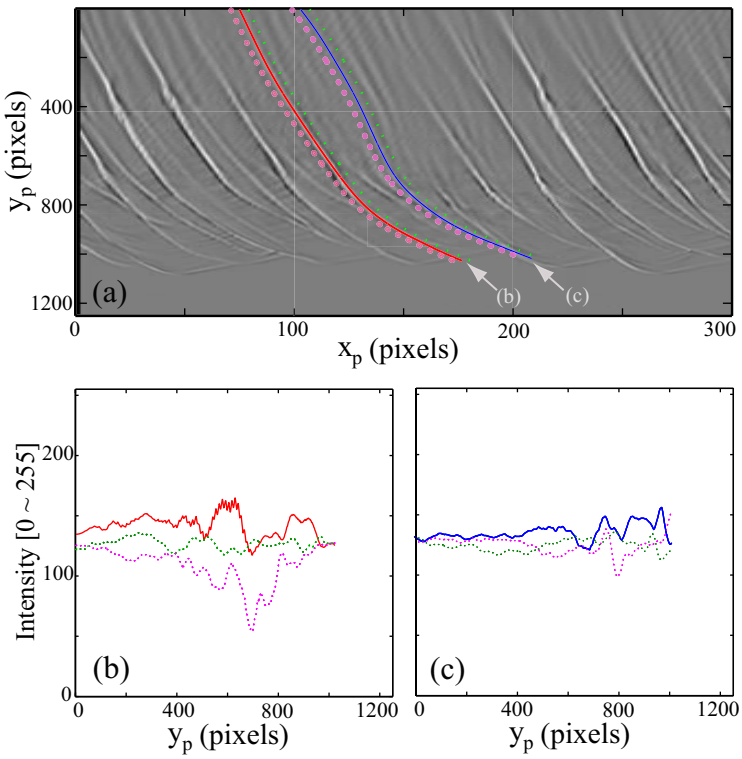

Figure 19: Removal of erroneous wave crest tracks through high intensity validation: (a) processed image timestack used to determine (red solid) valid and (blue solid) erroneous tracks with (pink dot) wave front and (green dot) wave rear face trajectories, (b) (red solid) intensity profile of valid wave crest track compared to its (pink dot) wave front and (green dot) wave rear intensity profiles, (c) (blue solid) intensity profile of erroneous wave crest track compared to its (pink dot) wave front and (green dot) wave rear intensity profiles.

face trajectories is conducted in the offshore area within 200 pixel-length from the offshore boundary of the y_p-axis throughout the present study, since wave breaking events causing high intensity noise are free in that offshore area.

3.5.2.2 Pattern repeatability validation of extracted track shapes

Erroneous wave crest tracks may still remain, even after the first step of track filtering is applied. The second step filters out the erroneous crest tracks on a physical basis. Random waves in the nearshore can be regarded as composed of multiple regular waves, having long-term regularities. Consecutive incident waves may show different wave breaking patterns in sequence, having different shapes of consecutive wave crest tracks. In the long term, such as the image dataset time-span of 34.2 minutes, however, each pattern of the different crest tracks is assumed to be repeated more than at least one time, since incident random waves consist of regular wave components. Hence, the extracted individual wave crest tracks can be grouped to the similar patterns of the crest track shapes. False tracking of the wave crests can be caused eventually by unexpected noisy intensity signals. A similar pattern of an erroneous tracking pattern will happen at most a couple of times during the dataset time-span. In order to remove those eventual tracking patterns, it is assumed that a real wave crest track shape is repeated more than 5 times during the dataset time-span in the present study. The reason for selecting the minimal pattern repeatability number 5 will be discussed in Chapter VI by investigating the effects of different numbers on filtering the extracted wave crest trajectories.

The extracted wave crest tracks can be grouped into the similar shape pattern groups by using an unsupervised learning and clustering analysis. Clustering processes organize objects into groups whose members are similar between them. In this study, the k-means clustering method is used. The k-means method is an algorithm

for partitioning the data points in a data matrix of $l \times m$ ($vertical \times horizontal$) cell size into L clusters where l is the number of subsets (i.e. the number of the extracted crest tracks), m is the number of data points contained in a subset, and L is the number of clusters (i.e. the number of the shape pattern groups). The algorithm minimizes the sum-of-squares criterion J:

$$J = \sum_{j=1}^{L} \sum_{n=1}^{m} \left| a_n^j - \mu_j \right|^2 \tag{22}$$

where a_n^j is the n^{th} data point of a cluster of j, and μ_j is the cluster center. The criterion indicates the distance of the $l \times m$ data points from their respective cluster centers. In the present study, the centroid in each cluster is computed using the squared Euclidean distance.

Prior to application of the k-means clustering method, the data matrix of $l \times m$ cell size should be prepared from the extracted crest tracks. The local slopes of each wave crest trajectory in the cross-shore timestack image domain are computed as the follows:

$$S^k\left(y_p\right) = \frac{dy_p^k\left(x_p\right)}{dx_p} = \frac{\Delta y_p^k}{\Delta x_p} \tag{23}$$

where $y_p^k\left(x_p\right)$ denotes the k^{th} wave crest trajectory, and $S^k\left(y_p\right)$ denotes local slopes of the crest trajectory. The computed local slopes, $S^k\left(y_p\right)$, with regard to y_p-axis are horizontal components of the k^{th} row in the data matrix.

The number of clusters is set to be the nearest integer to $l/5$. After applying the k-means clustering analysis, if members of a cluster are less than 5, those members of wave crest tracks are removed. An example of the wave crest tracks filtered through high intensity and pattern repeatability validations of the extracted crest tracks are shown in Fig. 17(b).

3.6 Experimental datasets

Nearshore video and field data used in this study are from measurement campaigns conducted at Myrtle Beach (SC) by coastal scientists from the University of South Carolina and Georgia Institute of Technology Savannah, in December, 2003. During the campaigns, hydrodynamic and bathymetric data were collected in the nearshore. The video wave imagery was also recorded by a camera mounted on a high building. The details of experimental methodology and results are found in research reports by Haas et al. (2004) and Obley et al. (2004). A brief description of the experimental methodology is given in this subsection. For this study, 4 different video and field datasets were selected from the 2003 Myrtle Beach data. So, characteristics of the 4 video and field datasets are also described.

3.6.1 In-situ measurements

Two types of in-situ experimental instruments were used to measure hydrodynamic data: two Nortek Aquadopp upward-looking current profilers and two Sontek Triton downward-looking Acoustic Doppler Velocimeters (ADV). During the 2003 experiments, the current profilers measured the profiles of three component velocities in 40 cm bins beginning 40 cm above the bottom. The ADVs measured three component velocities at a point around 20 cm above the bed. The four instruments were deployed in the surf zone along a beach profile, spanning approximately 80 m in distance and 2 $\sim$ 4 m in depth. Both the profilers and ADVs also collected pressure, water temperature, heading, pitch, and roll data. The profilers measured the hydrodynamic data at 1 Hz, and the ADVs at 2 Hz. Fig. 20 shows general locations of field experiments and instrumentations.

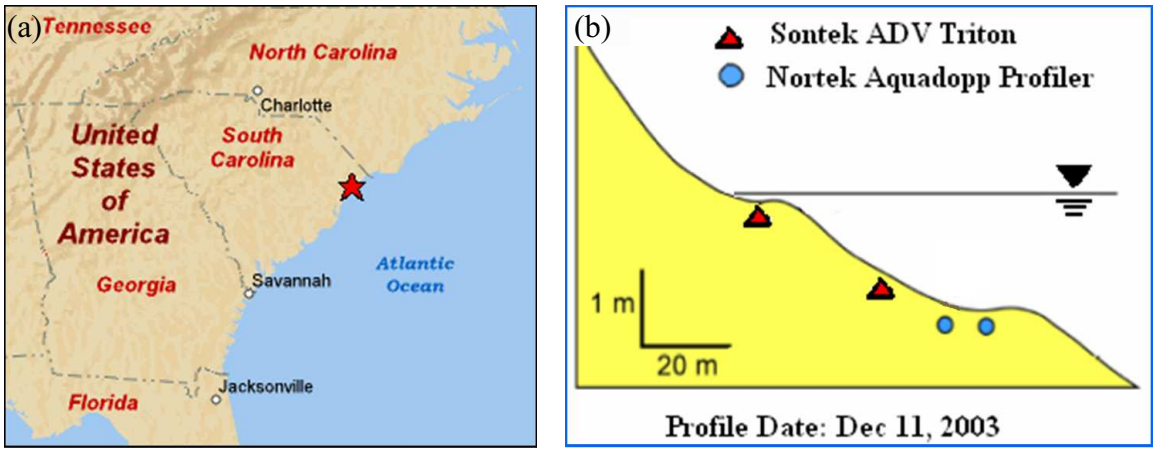

Figure 20: Approximate locations of field experiments and instrumentations: (a) Myrtle Beach location (star symbol), (b) brief beach profile and locations of the deployed instruments.

Intertidal and subtidal beach bathymetry was daily surveyed using Global Positioning System (GPS) and a Total Station (TS) system during the period Dec. 10 to Dec. 15, 2003. Components of the TS system are a Sokkia SET610 Total Station and 2 sets of single prisms on poles. The TS system was used to measure beach profiles and general beach bathymetry including the surf zone up to 1.5 m in water depth during low tide. The covered area of its measurements is 500 m alongshore and 200 m along cross-shore.

The GPS consists of two Ashtech Z-12 GPS receivers: one as a base station at a known geometric control point, and the other as a rover running in real time kinematic mode. Both the base and rover stations collected geometric position data at 0.1 and 1 Hz, respectively. The measurements covered an area from aerial beach to knee-level water depth at low tide, expanding about 100 m along aerial and intertidal cross-shore, and approximately 1,600 m alongshore.

In this study, the pressure head data and the three water velocity components collected by the instruments are used. From the pressure head data, water surface elevations and wave heights are computed by subtracting the tidal trend from the

pressure head data and counting waves via zero down-crossing method, respectively. Wave directions are computed using the pressure and two horizontal velocity component data. These wave data obtained from the in-situ measured pressure and water velocity data are compared to video-derived wave properties through this study. Beach profiles measured in the surf zone by the Total Station system are used primarily for comparison with the inverted depths from video imagery. In addition, the measured beach profiles are used to compute shallow water wave theories (linear and nonlinear)-based celerity.

3.6.2 Optical experiments

The equipments used for capturing nearshore video are a Sony TRV-900 camera equipped with a Raynox 0.66 wide angle and a PC set for storing video data. The camera was mounted atop a tripod on the balcony of the top floor of a condominium building. The place of the camera mounted was approximately 44 m high above the mean sea level. The digital video was recorded at 30 Hz in real-time scale as an AVI file. The resolution of video imagery is 720 $\times$ 480 pixels.

3.6.3 Selection of four video and field datasets

Four video and field datasets for this study were selected from the 2003 Myrtle video datasets such that their wave and imaging conditions represented a range of conditions. With regard to imaging conditions, image views with different camera angles and weather conditions were considered as the imaging factors. As for wave conditions, wave periods, wave heights, and depths of the breaking zone were considered for the dataset selections.

Table 1 gives a list of the four video datasets with collection dates, start times, durations, image down-sampling rates, image sizes, image views of camera and weather

Table 1: Video datasets used for the present study.

Case No.	I	II	III	IV
Date	12/11/2003	12/13/2003	12/15/2003	12/14/2003
Start time	17:27 GMT	17:30 GMT	16:30 GMT	15:10 GMT
Duration	34.2 min.	34.2 min.	34.2 min.	34.2 min.
Re-sampling rate	3 Hz	3 Hz	3 Hz	3 Hz
Image size (H x W)	480 x 720 pixels	480 x 720 pixels	480 x 720 pixels	480 x 720 pixels
Camera view	oblique-top	oblique-side	oblique-side	oblique-side
Weather	sunny	cloudy	rainy	sunny

conditions. The the image dataset time-spans, image re-sampling rates and image sizes are maintained at 34.2 minutes, 3 Hz, and 480×720 pixels respectively. The image dataset time-span of 34.2 minutes corresponds to 2048 data points for the deployed Aquadopp instruments which collected hydrodynamic data at 1 Hz.

Table 2 lists wave conditions for the four datasets obtained from hydrodynamic data collected by the offshore instrument, Aquadopp B, as indicated in Fig. 22. H_{max}, $H_{1/10}$, H_s, H_{rms}, T_p, and T_m denote the maximum wave height, the first highest 1/10 wave height, the significant height, the root-mean-square height, the peak period, and the mean period respectively. Those wave height statistics were computed from pressure head (m) time-series measured by the offshore instrument. Water surface elevation (m) time-series was obtained by subtracting the tidal trend from the pressure head data in each dataset. The number of waves in each water surface elevation dataset was counted using the zero down-crossing method. Heights (H) of the waves

Table 2: Sea states of each dataset obtained from the water pressure data collected by the offshore instrument Aquadopp B.

Case No.	I	II	III	IV
H_{max} (m)	0.49	0.87	1.21	0.69
$H_{1/10}$ (m)	0.44	0.64	0.89	0.56
H_s (m)	0.38	0.52	0.78	0.43
H_{rms} (m)	0.29	0.39	0.60	0.31
T_p (s)	8.2	5.6	8.4	8.3
T_m (s)	6.4	5.2	7.9	8.0
Water depth* (m)	1.09	2.31	2.78	2.11
Tide	Low	mid	high	mid
Notes	* : deployed depth of the instrument Aquadopp B.			

counted were in the range of $0.01 \cdot H_{max} \leq H \leq H_{max}$. Based on the number of waves counted and the computed wave heights in time sequence, H_{max}, $H_{1/10}$, H_s, H_{rms}, and T_m were calculated. T_p was obtained by spectral analysis of the wave surface level time-series.

Selection of the four different video datasets with consideration of their sea states and imaging conditions is for investigating: first, effects of imaging and wave conditions on wave crest detection in image sequences; second, applicability of the present wave property estimation methods to various wave image datasets; lastly, robustness of the present nonlinear depth inversion algorithm to various video datasets. In this

chapter, the first intent is primarily investigated.

3.6.4 Visibility of waves in the four datasets

The effects of imaging and wave conditions on wave crest detection in image sequences are investigated by looking into: 1) the effect of imaging conditions on visibility of waves in image sequences, 2) the effect of wave conditions on visibility of waves in the video imagery, and 3) dominance of either imaging conditions or wave conditions on the visibility of waves.

As for the effect of imaging conditions on visibility of waves in image sequences, the sunlight illumination, depending on daily weather, and the image view, depending on camera angle, are considered as factors affecting imaging conditions, since they were only changed in the 2003 video experiments. Fig. 21 presents a single snapshot of each dataset showing its camera view and weather condition. Cases I and IV were recorded on clear and sunny days, having good image contrast. Cases II and III were dark, providing less illumination for video imaging. Hence, they have poor image contrasts. Image contrast differences caused by the different weather conditions are clearly observed even by the naked eye. Obviously, it is observed that good weather conditions provide good imaging conditions, enabling the video camera to capture more waves in the image frame.

Cases I and IV in Fig. 21(a)(d), each having good image contrast, are compared to each other to investigate the effect of different camera angles on the wave visibility in images. Both display clearly discernable wave crests and troughs, even though waves are in the offshore or have small wave heights. Table 2 indicates that wave heights in Cases I and IV are much less than those in the other two cases. After the image rectification, wave crests and troughs with the small heights in Cases I and IV are still clearly visible without any large differences as shown in Fig. 22(a)(d). The

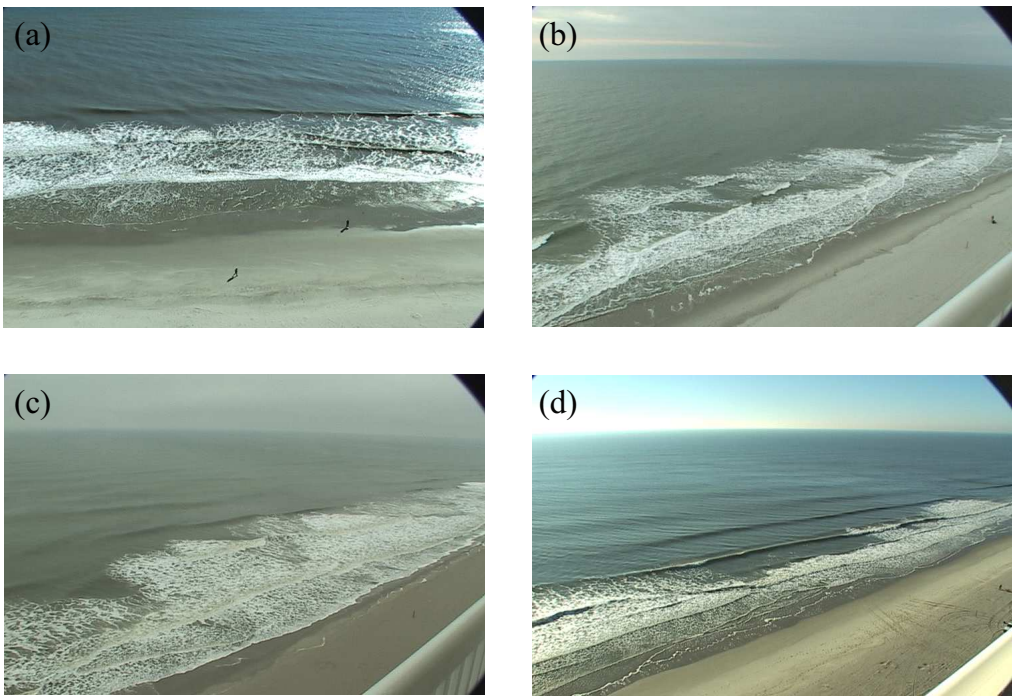

Figure 21: Instantaneous wave image snapshots from the four video datasets: (a) Case I, (b) Case II, (c) Case III, (d) Case IV.

distances between the camera and the surf zone of interest in the two cases are within 10 % of one another. Hence, it is concluded that the image view of camera is not a significant factor influencing visibility of waves in image sequences, if areas of interest are almost at the same distance from the video camera.

Regarding the effect of sea state conditions on wave visibility in the video imagery, the sea state parameters considered are the wave height, the wave period and the tidal state. Table 2 indicates that waves in Cases I and IV have relatively smaller wave heights compared to the other two cases. Case II has shorter wave period than the other three cases. The tidal levels in Cases I and IV are lower than the other two cases. In consideration of differences in the sea state paramters, it is observed from Figs. 21 and 22 that the wave visibility in images dominantly depends on the wave heights among other sea state parameters.

With regard to dominance of either imaging conditions or wave conditions on

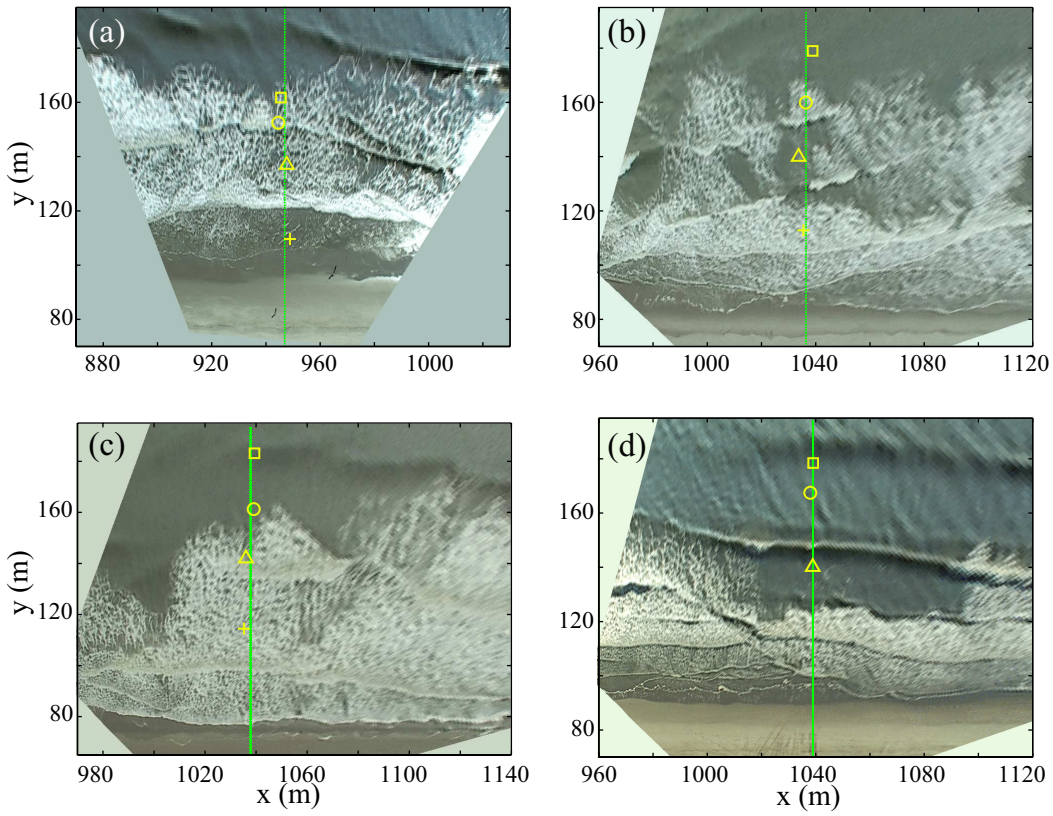

Figure 22: Rectified images of the original instantaneous snapshots from the four video datasets with (green lines) cross-transects to generate time-stacks, and locations of deployed instruments of (+) ADV 1, (△) ADV 2, (◯) Aquadopp C, and (□) Aquadopp B: (a) Case I, (b) Case II, (c) Case III, (d) Case IV.

visibility of waves, comparisons of the effects of the imaging and wave conditions on the captured wave images through bare eye-witnessing from Fig. 21 (or Fig. 22) and Table 2 indicate that the imaging conditions are more important than the wave conditions. The wave crests and troughs with even smaller wave heights in Cases I and IV are visible in the offshore. However, in Cases II and III having relatively high wave height conditions, only highest waves are discernable, since the sunlight illumination is not enough to capture small waves due to cloudy and rainy weathers.

Comparisons of the sea state and imaging characteristics of the four datasets are summarized in Table 3, indicating that the visibility of waves in the image sequences is dominantly influenced by the imaging conditions, i.e. the sunlight illumination, rather than the sea state conditions. Waves in Cases I and IV have smaller wave heights than those in Cases II and III to be captured in images. Meanwhile, Cases I and IV have better illumination than the other two cases. Thus, from the comparisons, it is observed that the visibility of waves in video image sequences is strongly affected by the sunlight illumination rather than other wave conditions. Quantified comparisons regarding the effects of image and sea state conditions on wave crest detection are discussed in the next subsection.

3.6.5 Errors in in-situ measurements

When video-derived wave height and water depth estimates are compared to in-situ measurements in this study, the measured pressure head data and surveyed beach profiles are used. In order for these comparisons to be validated, identification of possible error sources in the measure pressure and bathymetry data, and attempt to evaluate the magnitude of each are essential prior to comparisons between them.

Possible error sources in obtaining wave heights from the measured pressure data are: 1) errors in calibrating the pressure sensor, 2) errors in converting the pressure

Table 3: Comparisons of sea state and imaging charateristics of the four datasets.

Case No.	I	II	III	IV
Wave period	↑	↓	↑	↑
Wave height	↓	↑	↑	↓
Tide	↓	↑	↑	↓
Surf-zone width	↓	↑	↑	↓
Sun light	↑	↓	↓	↑
Visibility of waves in image	↑	↓	↓	↑
Notes	↑ : relatively more positive quantity compared to the others. ↓ : relatively smaller or less quantity compared to the others.			

data to wave heights, 3) errors in measuring pressure data by pressure sensors.

Since pressure sensors are calibrated before deployment through several trial tests, the calibration errors can be minimized as much as the manufacturers documented, thereby being negligible compared to the accuracy of pressure sensor itself. Wave instruments were deployed in shallow water, i.e. in the surf zone, during the 2003 Myrtle Beach data collections. So, it can be assumed that there is no attenuation of pressure data measured by the deployed pressure sensors. Consequently, water surface level data can be obtained directly from the pressure head data, based on the no attenuation assumption. Lastly, errors in measuring pressure data by pressure sensors are associated with accuracy of pressure sensors. If the first and second error sources mentioned above are considered to be negligible in shallow water, errors by accuracy of pressure sensors are most significant. In case of Aquadopp instrument, pressure sensor accuracy is $\pm 0.25\%$ (Obley et al., 2004). If the maximum wave height 1.21 m among the four datasets is considered, the maximum error magnitude in the wave height data for the four datasets is 0.003 m.

Error sources in the bathymetric data are: 1) human errors in handing the Total Station system, 2) errors by accuracy of the Total Station system.

Human errors, such as misreading a scale, can be introduced to the bathymetric data. If scientists handling the Total Station system are well educated and trained to survey bathymetry, the human errors can be assumed to be minimal. Errors by accuracy of the Total Station system correspond to roundoff errors of the measuring scale. The roundoff errors by the rod and level system was reported to be by up to 0.005 m in the vertical and by up to 0.05 m in the horizontal (Work, 1992).

3.7 Results and discussion

Nearshore video wave images contain foam patches which complicate tracking of the wave crests approaching the shoreline in the breaking zone. In order to reduce the

effects of noise in the image sequences, the image frame differencing method and the elliptic low-pass filter were applied to the image sequences. Thereafter, wave crest tracks were detected and extracted from the processed timestacks primarily by applying the Radon transform. Four different video datasets having various sea state and imaging conditions were used.

3.7.1 Results of foam removal

Through the image frame differencing and the directional low-pass image filtering (the elliptic Butterworth filter), 6150 original wave images of each video image dataset were processed to reduce visual noise from foam. The processed images were used to generate cross-shore timestacks.

A segment of the image intensity time-series after the image frame differencing and the elliptic low-passing filtering is shown in Fig. 23(b). Fig. 23 presents a comparison of the water surface level (η) and the image intensity time-series at the location of the offshore instrument in Case I. The time offset between the image intensity and the water surface elevation time-series was computed using the cross-correlation analysis, thereafter they were synchronized. In the original intensity time-series in Fig. 23(a), the high intensity values caused by the foam patches last up to $10 \sim 15$ seconds after instantaneous intensity peaks (red open circles) due to wave breaking. After applying the image processes (Fig. 23(b)), the high intensity levels due to foam patches were removed. Consequently, high peaks in the processed intensity time-series indicate wave crest peaks measured by the instrument more clearly. However, the wave form shape in the processed intensity data doesn't fit to that of natural waves very well. Due to this wave shape disagreement, spectral analysis of the processed intensity data in the frequency domain will result in wave property estimates different from actual wave properties.

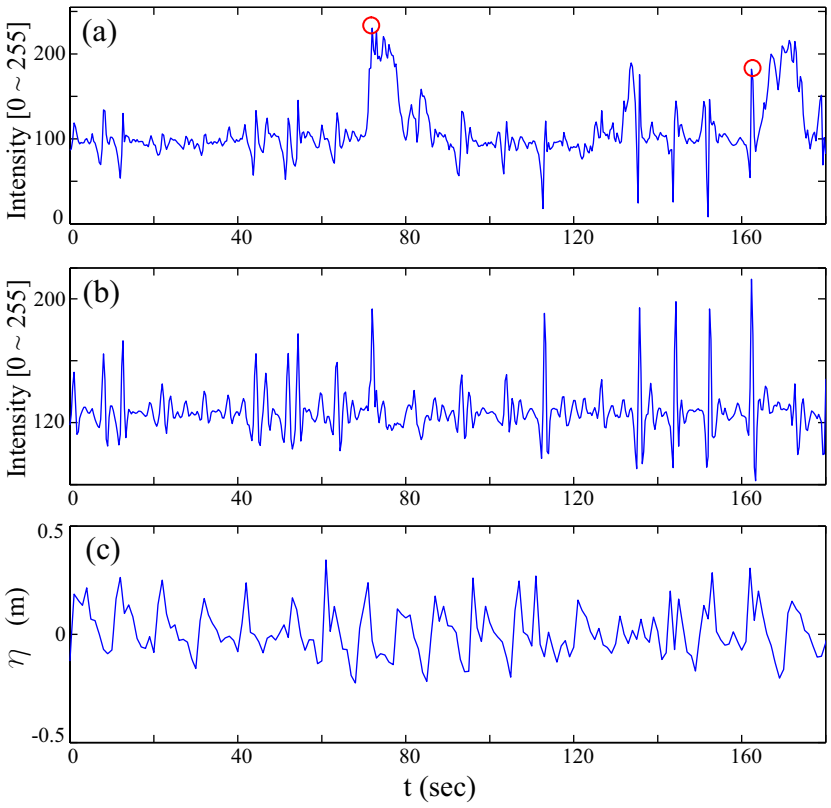

Figure 23: Comparison of pixel intensity and water surface level time-series of Case I: (a) original intensity time-series of Aquadopp B with (◯) wave breaking moments, (b) processed intensity time-series, (c) water surface level time-series from the pressure data of Aquadopp B.

3.7.2 Results of extracting wave crest tracks

Features of the individual wave crest trajectories were detected and tracked by applying the Radon transform starting from the offshore boundaries of the processed timestacks. The extracted crest tracks were filtered through the high intensity validation of the wave crests and the pattern repeatability validation of the crest trajectories.

After extracting wave crest tracks in the processed image timestacks, the erroneous crest tracks were first identified by checking whether wave crests maintain higher intensity as they propagate. Fig. 24(a)(b) shows all of the extracted crest tracks in Case IV and the result of the extracted crest track filtering by the high intensity

confirmation of the wave crests. The extracted crest trajectories in Fig. 24(a)(b)(c) were represented by the local slope profiles, S, obtained by Eq. 23. The second filtering of the extracted crest tracks was conducted by assuming that one of valid crest tracks is repeated more than 5 times during the dataset time-span. Fig. 24(c) presents the result of the second filtering of the filtered crest tracks in Fig. 24(b), consequently, showing that the unrealistic wave crest tracks having local slope profiles strongly deviating from the main pattern were filtered out.

In order to compare the wave crest track extraction results with in-situ measurements, the number of extracted wave trajectories in each dataset was compared to the number of waves counted from the measured pressure head data by the offshore instrument. Table 4 presents comparisons of the in-situ measured wave and extracted wave crest track numbers. Reasonably, the numbers of waves (N_w) having higher frequencies (Cases I and II) were counted more than those in the other two in-situ measured datasets. The mean periods T_m of Cases I and II are 6.4 and 5.2 seconds, while the periods of Cases III and IV are 7.9 and 8.0 seconds respectively.

Similarly, the numbers of the wave crest tracks (N_v^3) retained after the second crest track filtering in Cases I and II are larger than the other two cases. This indicates that high frequency waves provide more chances of detection of the wave crest tracks. However, the ratios of the realistic crest track number to the in-situ wave number (N_v^3/N_w) show that video imaging with better illumination conditions (Cases I and IV) captures more waves per given number of waves.

From those quantified comparisons, it is concluded that the imaging conditions with better sunlight illuminations are more important than the other wave conditions. Besides, the numbers of the realistic extracted wave crest tracks (N_v^3) approximate the number of the first highest 2/3 wave heights ($N_{2/3}$) from the ratios of $N_v^3/N_w \simeq 0.67$, since the high coherence between image intensity and wave height data (Lippmann and Holman, 1991) suggests that wave crests with higher wave heights can be more

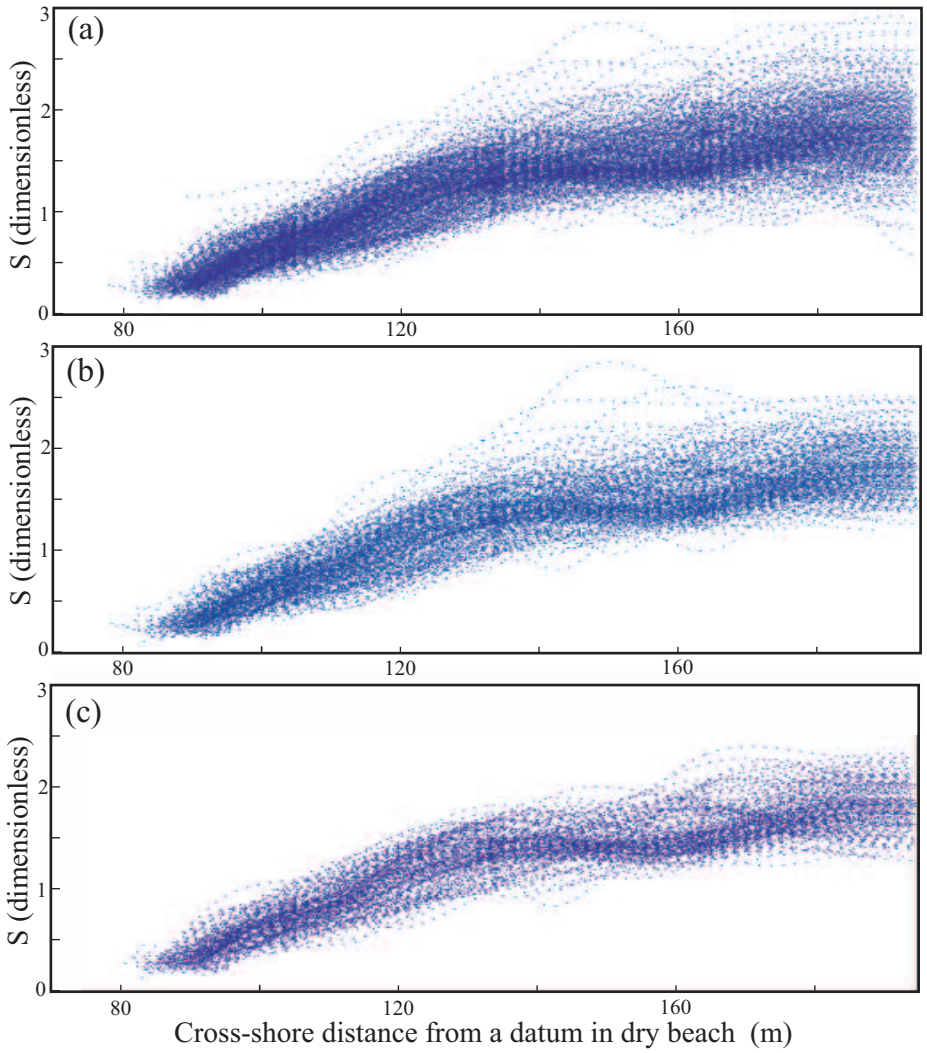

Figure 24: Accumulated profiles of local slope of individual wave crest tracks of Case IV : (a) initially extracted individual wave crest tracks, (b) wave crest tracks after the filtering by the high intensity validation, (c) wave crest tracks after the filtering by the pattern repeatability validation.

Table 4: Results of wave crest tracking and the crest track filtering.

Case No.	I	II	III	IV
N_w	302	415	259	253
$N_{1/3}$	101	138	86	84
N_v^1	544	643	521	541
N_v^2	295	362	257	309
N_v^3	203	266	147	196
N_v^3 / N_w	0.67	0.64	0.57	0.77
Notes	N_w : number of waves in the record of the Aquadopp B. $N_{1/3}$: number of the first highest 1/3 wave heights in record. N_v^1 : number of the initial starting points of the crest tracking. N_v^2 : number of the crest tracks after the first track filtering. N_v^3 : number of the crest tracks after the second track filtering.			

clearly visible and more likely detected as realistic wave crest tracks.

3.8 Summary

The experimental field data were selected from a 2003 Myrtle Beach video datasets for this study. The four video datasets have different sea state and imaging conditions. The image frame differencing method and the elliptic Butterworth filter were developed to reduce the effects of visual noise due to foam in the image sequences. After processing the image sequences by the present image processing methods, cross-shore timestacks were generated from the processed image sequences to obtain analyzable physical quantities associated with incoming waves in the cross-shore direction. Thereafter, wave crest tracks were detected and extracted from the processed timestacks primarily by applying the Radon transform. Features of the individual wave crest trajectories were detected and tracked by applying the Radon transform starting from the offshore boundaries of the processed timestacks. The extracted crest tracks were filtered through the high intensity validation of the wave crests and the pattern repeatability validation of the crest trajectories.

The numbers N_v^3 of the retained wave crest tracks after the second crest track filtering were compared to those N_w of the waves counted from the in-situ measured pressure head data. The ratio N_v^3/N_w was approximately 0.67, ranging from 0.57 to 0.77 for the four datasets, indicating that the number of the extracted wave crest tracks retained after the second step track filtering is about twice the number of the 1/3 wave heights. The ratios N_v^3/N_w in the video datasets having better illumination conditions were commonly found higher, meaning that video imaging in clean weather captured more waves per given number of waves than in cloudy weather.

CHAPTER IV

WAVE PROPERTY ESTIMATION

4.1 Introduction

Wave properties such as wave celerity, wave period, and wavelength have been derived from remotely sensed imagery for the depth inversion purposes (Piotrowski and Dugan, 2002; Stockdon and Holman, 2000; etc.). Most of the former property estimation methods are implemented in the frequency domain, assuming that wave fields are stationary over the whole time domain. In contrast, individual wave crest tracks are traced along the cross-shore in the time domain. Each wave in random wave fields may have different properties in sequence, requiring a wave-by-wave approach to estimate consecutive wave properties. In the present study, each wave crest property is estimated in time sequences and traced along the cross-shore using the nearshore image timestacks and the extracted individual crest trajectories.

This chapter describes the methods of estimating wave properties (i.e. wave celerity, wave period, wavelength and incident wave angle) using the extracted wave crest trajectories, the original image timestacks, and the processed image sequences. The timestacks are in the space-time domain, being physically and quantitatively analyzed to obtain wave celerity and wave period. The incident wave angle is estimated in the space-space image domain. Fig. 25 contains a diagram illustrating estimation of wave properties from the input of nearshore video image data.

The wave crest trajectories extracted in the cross-shore time stack domain are used to estimate individual wave celerity profiles ($c_y(y)$ where c_y = y-component of wave celerity vector c). Wave breaking points (y_b) of individual wave crests are determined using wave crest trajectories and their intensity profiles obtained from the

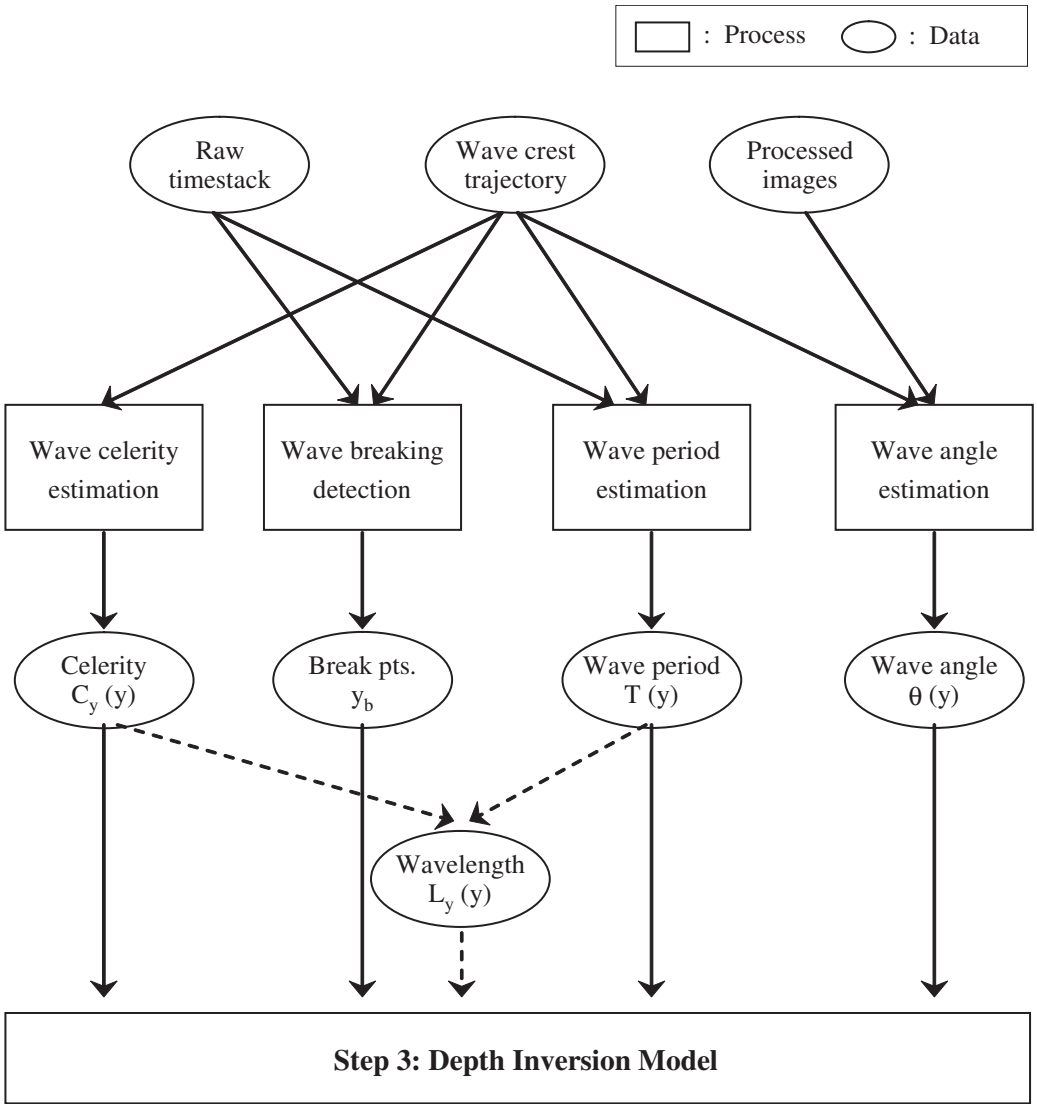

Figure 25: Diagram describing wave property estimation procedures along with data inputs and outputs.

raw image timestacks. Intensity time-series at each location in a raw image timestack are used to analyze wave periods using the wavelet analysis method, resulting in a transient wave period map in the space-time domain (i.e. timestack domain). Tracing each wave crest trajectory in the wave period map provides its wave period profile $T(y)$. Wavelength profile for each wave crest trajectory is obtained by the product of $c_y(y)$ and $T(y)$. With regard to incident wave angle estimation, the wave angle at each time-point of a wave crest trajectory is computed from the processed image corresponding to each point in time. The more detailed explanations of wave property estimation will be described in the subsequent subsections.

4.2 Estimation of wave phase speed

Wave phase speed measured by remote sensing techniques has been used as a key parameter to determine nearshore bathymetry since World War II. In general, water surface level data in time-series are required to calculate wave celerity. Various methods to retrieve wave properties from the wave surface level data have been suggested. For monochromatic waves, once the wave period T, and the wavelength L are obtained from the water surface data, wave celerity c can be simply calculated as c = L/T (Eq. 2).

4.2.1 Wave image based celerity estimation

In contrast to monochromatic waves, waves in the nearshore have random periods and lengths. Suhayda and Pettigrew (1977) photographed a series of wave poles deployed along cross-shore in the breaking zone to measure wave phase speeds. The wave crest speed between poles from the photographic record was determined.

Stockdon and Holman (2000) applied a spectral analysis method to the pixel intensity time-series at each location in a cross-shore timestack used as a proxy of the

water surface elevation data to evaluate peak wave period in the nearshore field. For estimating wavenumbers in the cross-shore direction, Stockdon and Holman (2000) applied CEOF analysis to the cross-shore timestack, thereafter computing dominant wave phase speeds along the cross-shore by Eq. 2.

Cross-spectral methods to measure dominant wave phase speeds from the water elevation data collected at two locations have been applied to the remotely sensed wave image data, e.g. video imagery (Lippmann and Holman, 1991) and X-band radar imagery (Bell, 1999). Holland (2001) investigated nonlinear amplitude dispersion effects by analyzing wave phase speeds with the application of the cross-spectral method to the pressure sensor signals collected at known depths in the nearshore.

Catalan (2005) estimated local phase speeds by calculating the local slopes of the wave front trajectories detected from the mean-removed cross-shore timestack in the space(y)-time(t) domain as defined in Eq. 24, assuming no shape change of a wave form during the time interval Δt:

$$c\,(y,t) = \frac{dy}{dt} = \frac{\Delta y}{\Delta t} \tag{24}$$

The pixel intensity time-series in the processed imagery timestacks by the present image processing methods cannot be used as a proxy for the free surface elevation data, even though visual noisy signals due to foam were removed in the processed image sequences. This is because the pixel intensity signals are strongly reformed through the image processing procedure, having wave forms different from natural wave shapes. So, it is not reasonable to apply spectral analysis methods for estimating wave phase speeds to the processed pixel intensity data. In the present study, similarly to the wave phase speed estimation by Catalan (2005), local wave phase speed is calculated by taking the first derivative at each location of the wave crest trajectories extracted in the space(y)time(t) domain (hereafter, referred to the wave crest trajectory method).

4.2.2 Wave celerity transition across the breaker points

The wave form changes as waves move toward the shoreline (Sevendsen et al., 1978). In particular, wave steepness increases rapidly and the wave crest front surface is overturned at the moment of wave breaking, causing a phase shift of the wave crests. Overturning of the wave front face is pronounced in plunging breaking. In this area of energetic wave breaking, wave crest speeds have been observed to be larger than the nonlinear shallow water wave equations (NSWE) based wave celerity which can be expressed as an approximated local phase speed $C = \sqrt{g(h + \eta_c)}$ (hereafter, referred to as the NSWE based local wave celerity) where η_c is the elevation of the wave crests above the mean water level.

Chang and Liu (1998) measured the speed of the overturning monochromatic wave crests using the PIV analysis method. The speed of the overturning crests reached 1.68 times the wave celerity computed by linear wave theory. The overturning crest speed corresponds to 1.1 times the wave celerity computed using the solitary wave theory-based celerity celerity approximation $C = \sqrt{g\,(h + H)}$. The use of the solitary wave theory-based celerity approximation for regular waves is based on that the wave crest elevations above the mean sea level reaching almost the wave heights (Hansen, 1990), i.e. $\eta_c \approx H$, at the breaker points owing to extensive wave shoaling. Suhayda and Pettigrew (1977) observed wave heights and wave celerities across the surf zone in field using a series of 22 wave poles. Fig. 26 presents their measurement results showing that the measured celerity around the breaker point reached 1.2 times the nonlinear shallow water wave equation-based local wave celerity $\sqrt{gh_c}$ where $h_c = h + \eta_c$. In the video experiments of Catalan (2005), the celerity profiles measured along the 1-D wave flume also show wave celerity transitions across breaker points $1.17 \sim 1.45$ times higher than a finite amplitude dispersion (composite dispersion)

based nonlinear wave celerity, depending on wave heights and wave periods.

In the area of wave celerity transition across the breaker points, waves experience accelerated wave phase speeds even larger than 1.2 times the nonlinear shallow water wave equation-based local celerity as mentioned above. Thus, the nonlinear shallow water wave equation-based depth inversions merely using the measured celerity may have a tendency to over-predict water depths around the breaker points in the nearshore if the accelerated celerity transition is not considered properly. The present study considers the wave celerity transition around the breaker points in individual celerity profiles to reduce the errors of nonlinear depth inversion. In order to reduce the wave celerity transition effect from each celerity profile derived from video image data and derive the remote sensing-based nonlinear depth inversion successfully, the wave breaking points need to be identified along the cross-shore celerity profile.

4.2.3 Detection of wave breaker points

During wave breaking, wave form asymmetry becomes greatest, resulting in saw-tooth shapes. At the moment of wave breaking, the wave crest front faces are commonly overturned, resulting in a dark shadow in front of the faces. The dark shadow at the breaker point is observable in a raw image cross-shore timestack. In contrast, the wave crests become brighter after wave breaking than before wave breaking. Consequently, the pixel intensity of wave crests increases abruptly just inshore of the breaker point. In addition, the wave phase speed of each wave crest exhibits local maxima at the breaker points. Monochromatic waves show uniform patterns of wave breaking near a well-defined certain breaker point. So, the breaker point is easily identified from wave image sequences in this case. However, in the random wave field, the wave breaking mechanism is complicated. Wave breaking occurs at different locations as shown in Fig. 27(a), generally depending on wave properties (primarily wave height)

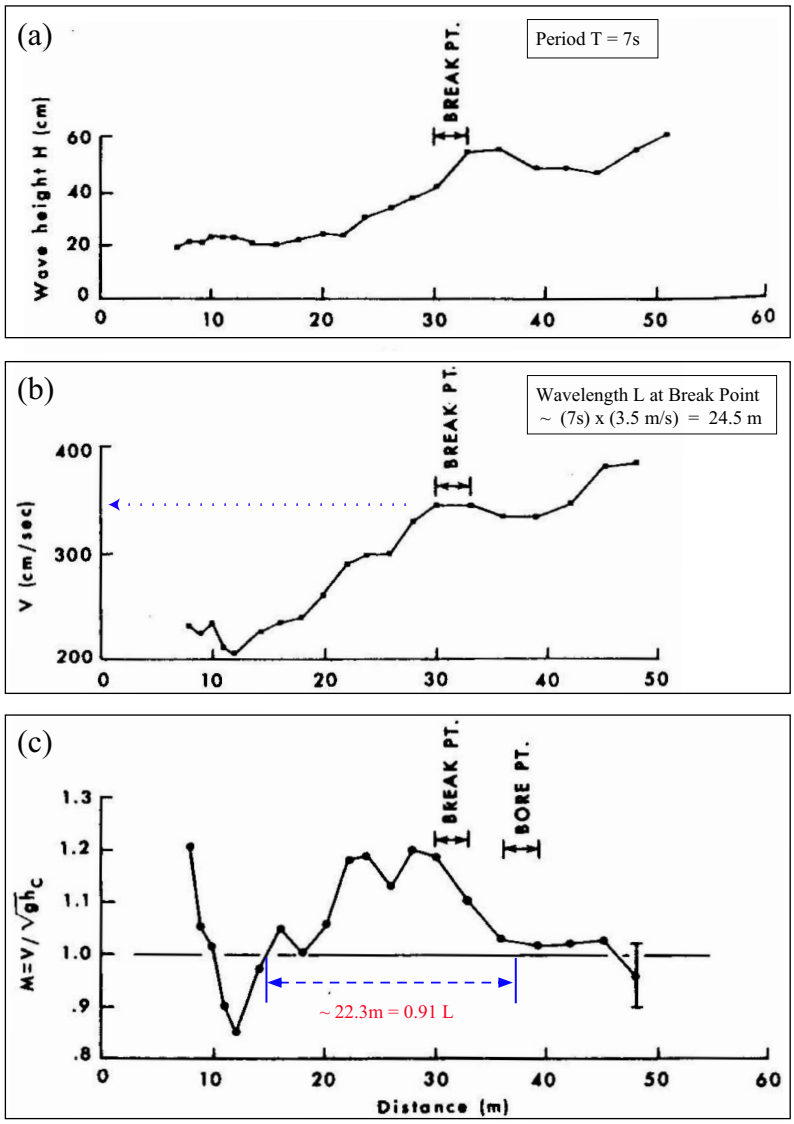

Figure 26: Observation of wave height and wave celerity in the surf zone (Suhayda and Pettigrew, 1977): (a) wave height, (b) wave celerity, (c) the ratio of measured celerity to the nonlinear wave celerity.

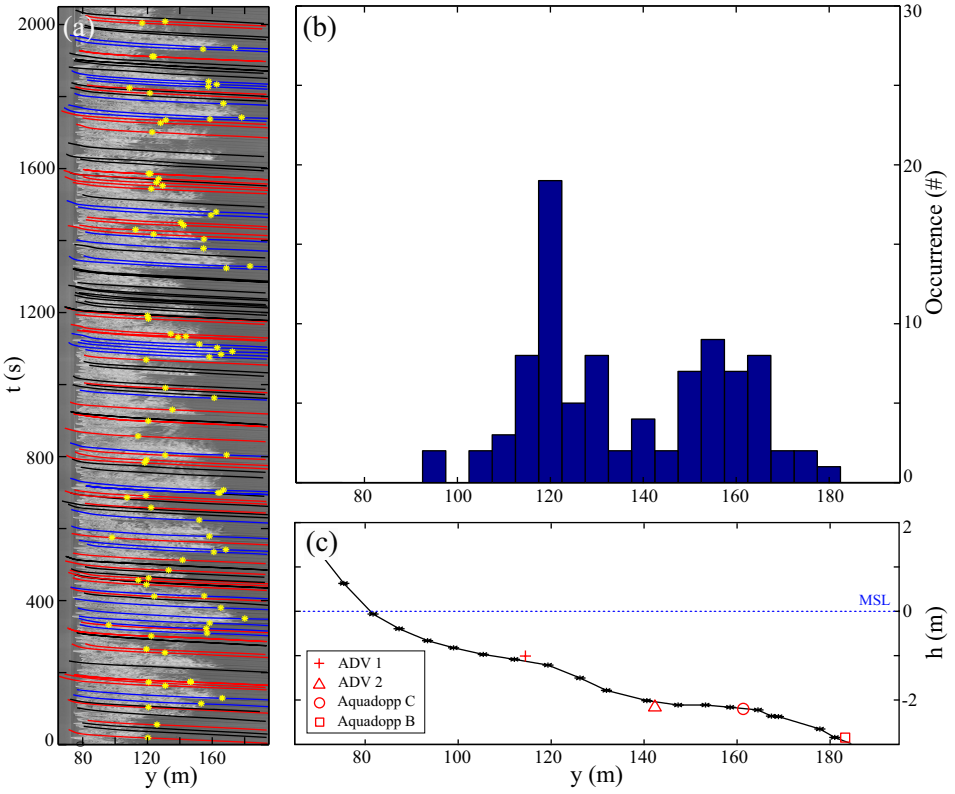

Figure 27: Wave breaking points detected from wave image data in Case 3: (a) raw image time stack with (blue line) outer breaking waves, (red line) intermediate breaking waves, (black line) inner breaking waves, and (yellow star) breaking points, (b) histogram of wave breaking occurrences along the cross-shore with a bin width of 5m, (c) the measured beach profile.

and water depths. If a wave breaks in the area of white foam patches generated by precedent wave breakings, its breaking event does not look obvious in original wave image sequence. In contrast, waves breaking in the area having few white foam patches like the outer surf zone results in an abrupt change of image pixel intensity across the breaker point, enabling the breaker point to be detected readily.

The surf zone can be divided into 2 sub-regions: inner breaking and outer breaking zones. The inner breaking zone including the swash zone is regarded as the saturated breaker zone where most of waves are collapsed and dissipating. In the outer breaking zone generally wider than the inner surf zone, only some portion of waves are breaking, having the breaker points spread out over the zone. In this study, the surf zone is

divided into three sub-regions for the purpose of wave breaking point detection: inner breaking, intermediate breaking and outer breaking zones. The inner breaking events happen in the saturated breaker zone, i.e. the area of white foam. It is hard to identify the breaker points of those inner breaking waves from the raw imagery. Thus, the present study will not detect the breaker points of inner breaking and discard inner breaking waves in the nonlinear depth inversion in Chapter V. The outer breaking occurs around the seaward boundary of the surf zone. The intermediate wave breaking occurs between the inner breaking zone and the outer breaking zone.

In order to detect the breaker points, individual wave crest trajectories, celerity profiles and raw image cross-shore timestacks are used. Detection of the breaker points is conducted through four steps: 1) grouping individual waves into three wave breaking groups, 2) identifying the local maximum point of each wave celerity profile in its breaking area, 3) collecting the intensity profile of each wave crest using its trajectory and raw image timestack, 4) identifying abrupt changes in pixel intensity along the intensity profile. The local celerity maximum or the abrupt intensity change point is accepted as the wave breaking point.

The wave celerity transition across the breaker points provides wave breaking related unique feature, i.e. local celerity peak to each celerity profile. This indicates that if multiple wave celerity profiles have the breaker points at a certain location, they will have a similar pattern of the celerity profile shapes. In this study, patterns of individual wave celerity profiles in each of the four datasets are clustered into the three groups (i.e. inner breaking, intermediate breaking, and outer breaking groups) by applying the k-means unsupervised learning and partitioning method (Spath, 1985) used to validate pattern repeatability of the extracted wave crest track shapes in Chapter III (Eq. 22).

For instance, Fig. 28 presents the results of partitioning individual celerity profiles into the three groups in Case 3 using the k-means partitioning method. Each group

partitioned from the wave celerity profiles is represented by a locally averaged celerity profile in Fig. 28(b). The averaged celerity profile in each group shows the local celerity peak in its breaking area. The celerity profile of the outer breaking group (solid line with diamond symbols) has the local peak in the outer surf zone, and the intermediate breaking group celerity profile is locally peaked between the other two celerity group peaks. Fig. 28(a) presents the intensity profile of each wave breaking group. Reasonably, the intensity profiles show rapid intensity increasing across the local celerity peak positions observed in Fig. 28(b). The intensity profile of each group is obtained by collecting the intensity profiles of individual wave crest trajectories in each group from the raw image timestack and locally averaging the collected intensity profiles.

The celerity profile of the inner breaking group has the lowest celerity in the intermediate and the outer breaking zones, and its local peak caused by the accelerated wave celerity transition across the breaker points (90 m $\leq y \leq$ 120 m) is almost flat compared to those of the other two groups. This fact indicates that the inner breaking waves have smaller wave heights than the other two groups, consequently experiencing weaker wave celerity transition than those of the other two groups. In addition, the intensity profile of the inner breaking group shows a rapid intensity increase right after the breaker points of the intermediate group, having almost the same profile shape to the intensity profile of the intermediate breaking group. This indicates that image pixel intensity of the inner breaking waves is influenced by foam having high intensity generated by the intermediate breaking waves, resulting in the similar intensity profile. Hence, in the inner breaking group case, it is difficult to identify the local celerity peaks and wave breaking related rapid intensity increase points.

In this study, the breaker points of individual waves are primarily identified with the local celerity peak points in their breaking region. If the local celerity peak points

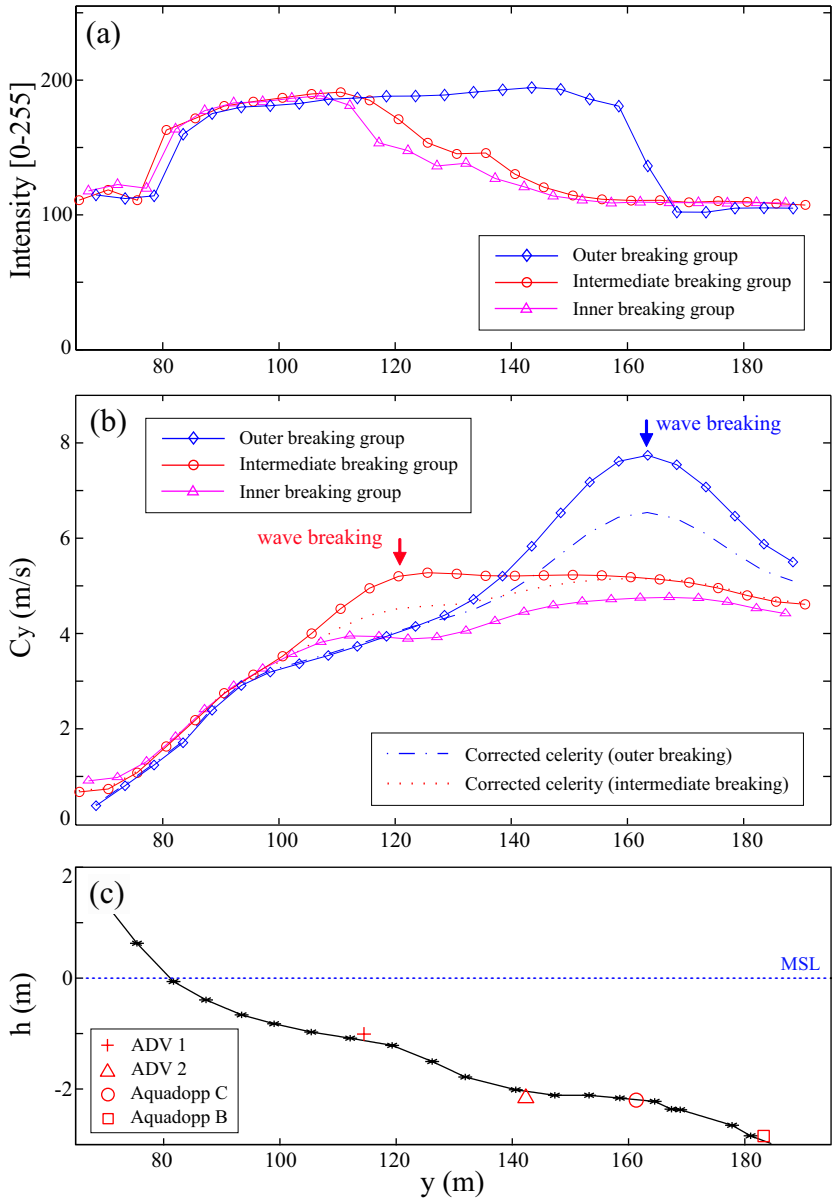

Figure 28: Grouping wave celerity profiles into 3 groups based on the breaker point in Case 3: (a) Intensity profiles of 3 groups, (b) celerity profiles of 3 groups, (c) the measured beach profile.

are not detected in their breaking zone, rapid intensity increase points are accepted as the breaker point. This is because some of the celerity profiles in the outer breaking group do not have the local celerity peaks, showing a continuously increasing trend. Throughout the present study, the intensity profile is median filtered using a sliding interrogation window 5m-long, and the abrupt intensity increase point is defined as $dI/dy(= \Delta I/\Delta y) = \Delta I/(5m) = 10/(5m)$ where I = pixel intensity. If the abrupt intensity increase points are not found in their breaking region, those waves are discarded from their group and not considered in the nonlinear depth inversion in Chapter V.

4.2.4 Correction of wave celerity transition at the breaker points

In order for the nonlinear shallow water wave equation-based depth inversion using the remotely sensed celerity profiles to perform properly, the accelerated wave celerity transition across the breaker points should be adjusted to be comparable to the nonlinear shallow water wave equation-based celerity approximation. However, research defining the wave celerity transitions across the breaker points is not well documented. Hence, this study models wave celerity transition based on the previously measured data of wave celerity in the surf zone.

The previous studies observed that wave celerity across the breaker point exceeds 1.2 times the nonlinear shallow water wave equation-based predicted celerity, ranging up to 1.45 times. The wave celerity transition, which is larger than the nonlinear shallow water wave equation-based predicted celerity across the breaker point, continued to occur over a certain distance, named the wave celerity transition distance for this study. The in-situ field measurements of wave celerity by Suhayda and Pettigrew (1977) suggest that the transition distance be $0.91L_b$ where L_b = wavelength at the breaker point as shown in Fig. 26. The optical celerity measurements by Catalan

(2005) show that the celerity transition distance ranges approximately from $0.4L_b$ to $0.9L_b$.

In this study, the ratio of the measured wave celerity to the nonlinear shallow water wave equation-based local wave celerity at the breaker points (y_b) is set to be 1.2, and the wave celerity transition distance (D_b) across the breaker points is assumed to be $1.0L_b$. The wavelength L_b at the breaker points is computed by multiplying the celerity $c_y(y_b)$ by the wave period T. Using those celerity transition related parameters, the ratio ($r_c(y)$) of the measured wave celerity to the nonlinear shallow water wave equation-based local celerity across the celerity transition distance is modeled to have a parabolic variation form similar to the observation of Suhayda and Pettigrew (1977) in Fig. 26(c):

$$r_c\,(y) = 1.2 - \frac{0.2}{(0.5L_b)^2}|y - y_b|^2\ , \quad for \quad |y - y_b| \leq \frac{L_b}{2}\ . \tag{25}$$

Hence, the measured wave celerity across the celerity transition distance is adjusted as follows, to be used in the nonlinear wave theory-based depth inversion:

$$c_y^c\,(y) = \frac{c_y^m\,(y)}{r_c\,(y)} \tag{26}$$

where c_y^c is the adjusted celerity and c_y^m is the remotely measured celerity. In Fig. 28(b), for instance, the celerity profiles adjusted by Eq. 26 of the dataset Case 3 are presented. The adjusted celerity profiles are significantly lower than the original celerity profiles across the breaker points.

4.3 Estimation of wave period

The dominant wave period can be obtained by applying a spectral analysis to the water surface elevation data. The peak period T_p by the spectral analysis is commonly represented as the most energetic wave period. Remote sensing-based coastal research

has estimated the peak period from wave imagery. Lippmann and Holman (1991) showed that the relationship between the video image intensity and pressure sensor data has high coherence of cross spectra between them. Stockdon and Holman (2000) applied the spectral analysis to the pixel intensity time-series at each location in a cross-shore timestack. Stockdon and Holman (2000) averaged the peak period values of all location points along a cross-shore transect and adopted the mean as the dominant incident wave period.

The present study also intends to determine wave period using video image data. Fig. 29 presents a preliminary test result to compare spectral analysis results of the in-situ measured pressure head and video image intensity data of the dataset Case 4. The spectral result of video data reasonably indicates peak frequency and even the second harmonic obtained by the spectral analysis of the in-situ measured data, suggesting that the present video data can be used to determine the peak wave period.

The implicit assumption in the spectral analysis is that the wave field is stationary, not having temporal change of wave properties within the period being analyzed. However, in a random wave field, the time intervals between two consecutive wave crests passing by a certain location vary arbitrarily in terms of time sequence, and the peak period by the spectral analysis is not representative of every wave. In order to comply with the wave-by-wave approach throughout the present study, it is required to determine the sole wave period of each wave under the random wave circumstance.

4.3.1 Time varying wave characteristics

In reality, transitory groups of incident waves exist and are observed in the nearhsore, having various wave breaking locations over the surf zone. Svendsen and Veeramony (2001) showed that grouping of the incident waves affects the locations of individual

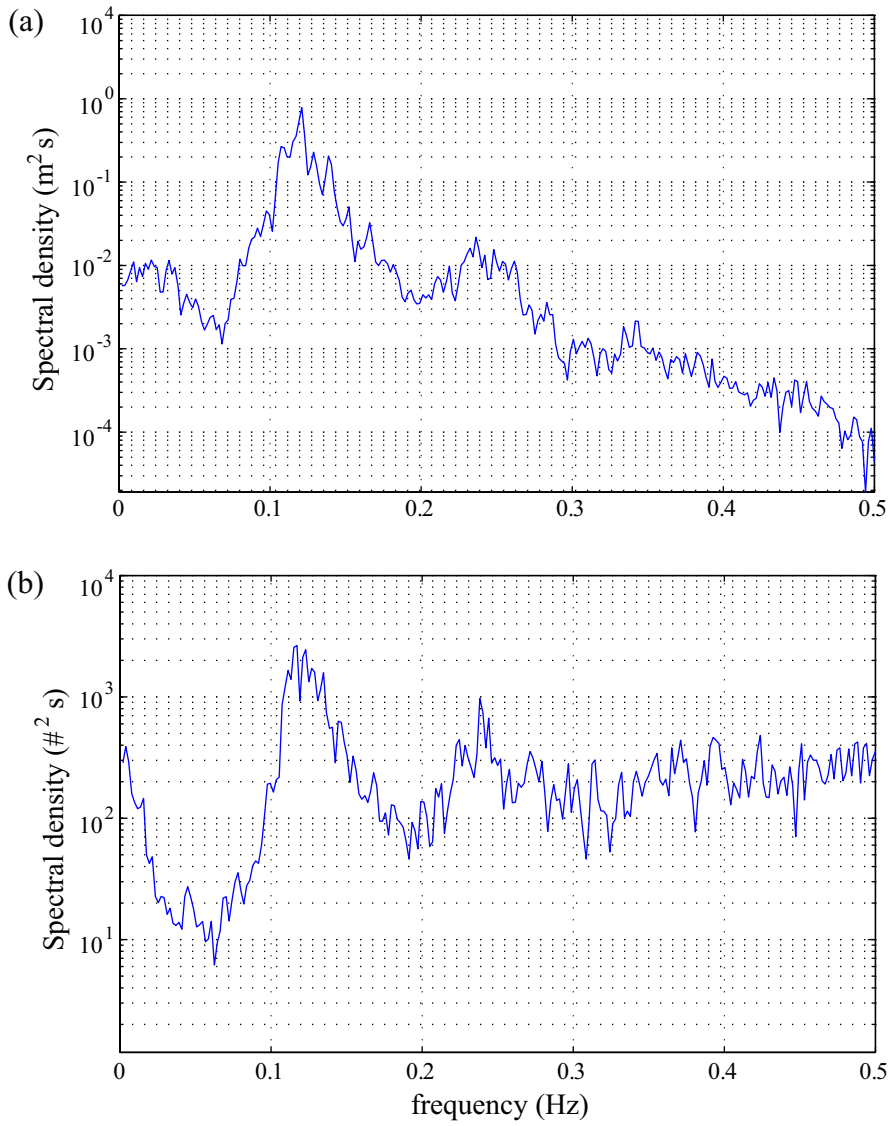

Figure 29: Spectral analysis of in-situ measured pressure head (Aquadopp B) and video image intensity data from Case 4: (a) frequency spectrum of the measured pressure head data, (b) frequency spectrum of intensity data.

wave breaking. For instance, Fig. 30(a)(b) presents different locations of wave breaking influenced by the wave grouping in the surf zone. The raw imagery cross-shore timestack in Fig. 30(a) confirms different locations of wave breaking in groups such that some wave groups break earlier in the outer surf zone but other groups break later in the inner surf zone. The outline of the intensity signals in Fig. 30(b) obtained at a location in the surf zone (i.e. along the slice of the timestack with a yellow dotted line in Fig. 30(a)) present those wave group envelops having different sizes and lengths varying in time.

In order to investigate characteristics of wind waves in intermittent groups, Liu (2000) adopted a wavelet analysis. Throughout the application of the wavelet analysis, Liu (2000) suggested time localized terms for characterizing each wave group such as the dominant group frequency f_g, the group duration t_g, the dominant group wave height h_g, etc. The dominant group frequency f_g is defined as the frequency of the peak energy over the time length t_g. The detailed definitions of the other terms are found in the cited reference.

4.3.2 Transient wave period by wavelet analysis

In this study, similarly, a wavelet analysis is applied to video image intensity data to obtain transient peak periods T_t which are defined as a wave period of the instantaneous peak energy in the wavelet spectrum at each time point. The use of the wavelet analysis in this study involves the use of the continuous wavelet transform based on a wavelet function of the Morlet wavelet (Morlet et al., 1982) which is useful for time-series analysis and for capturing oscillatory behavior (Torrence and Compo, 1998). The details of the wavelet analysis used in this study are found in the reference of Torrence and Compo (1998).

In order to determine the transient peak period for each wave crest, its trajectory

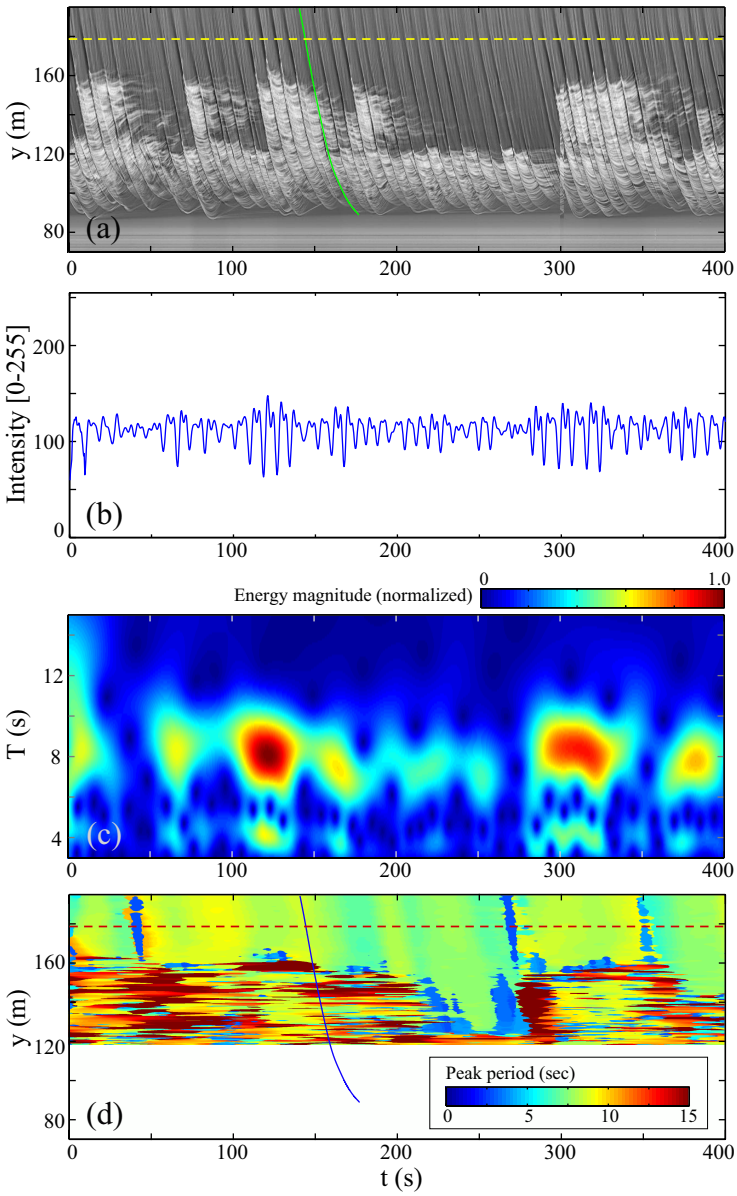

Figure 30: Morlet wavelet analysis of original pixel intensity time-series from video data of Case 4: (a) Original image cross-shore timestack with (yellow dotted line) a slice of intensity time-series and (green solid line) a wave crest track, (b) pixel intensity time-series from the slice in (a), (c) wavelet spectrum of (b), (d) transient peak period map of (a).

and the original image cross-shore timestack are used. To begin with, from the original image timestack, a slice of pixel intensity time-series at a location in the cross-shore direction is taken out as shown in Fig. 30(a)(b). Thereafter, the wavelet analysis is applied to the intensity time-series to obtain their wavelet spectrum in Fig. 30(c). From the wavelet spectrum, wave period corresponding to the peak energy at each time point is selected as the transient peak period. Consequently, a transient peak period time-series is produced from the wavelet spectrum.

The transient peak period time-series is put into a 1-D data array (red dotted line) at the same cross-shore location in the domain of the transient peak period map in Fig. 30(d). The red dotted line corresponds to the location in the cross-shore at which the pixel intensity time-series is taken out. By moving the pixel intensity time-series slice in Fig. 30(a) from the offshore boundary to the inner breaking seaward boundary, the transient peak period map in Fig. 30(d) is generated. Lastly, using each wave crest trajectory in the timestack domain of the transient peak period map, its transient peak period profile is obtained. Fig. 31 presents the transient peak period profile obtained along the wave crest trajectory (blue solid line) presented in Fig. 30(d). The transient peak period is almost a constant value along the crest trajectory up to the breaker point.

As Fig. 31(b) shows the transient peak period profile during propagation of a wave, the peak period map in Fig. 30(d) has a tendency to maintain consistent wave period values up to the wave breaking points in the wave propagation direction. This indicates that each wave maintains its sole wave period during its propagation to the shoreline. Hence, in this study, the wave period for a wave crest trajectory is selected as the median value of the transient peak period profile in the offshore region within 5m from the offshore boundary. In addition, incident wave period range of 3 to 15 seconds is considered throughout the study. The computed wave period for each wave crest trajectory is used along with its wave celerity profile to calculate its

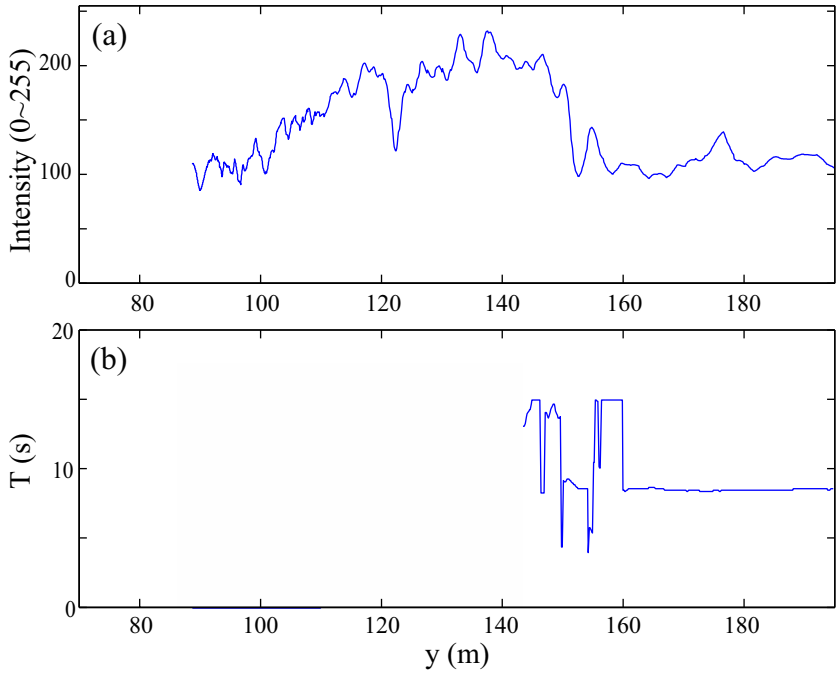

Figure 31: Intensity and transient peak period profiles obtained along a wave crest trajectory in Fig. 30(a) and (d) respectively: (a) intensity profile, (b) transient peak period profile.

corresponding wavelength profile in the cross-shore direction and will be an input to the depth inversion model in Chapter V.

4.4 Estimation of wavelength

The wavelength can be obtained by applying the frequency domain complex empirical orthogonal function analysis to a cross-shore array of pixel intensity time-series (Stockdon and Holman, 2000). However, either the raw or the processed pixel intensity data in the wave breaking region cannot be used as a proxy for actual wave data and be input to the complex empirical orthogonal function analysis. This is because the form of the intensity signals does not correspond to the shape of the actual waves due to the foam patches and the intensity signal reformation by image processing. Instead, the wave length L is calculated using Eq. 27 in which wave phase speed C

and wave period T are estimated via techniques described in the previous sections.

$$L = C \times T \tag{27}$$

The wavelength profile determined for each wave crest trajectory using the above equation is also used as an input to the depth inversion model in Chapter V. Since the wavelength profile for each wave trajectory is obtained from its celerity profile multiplied by its sole wave period which is constant, the wavelength profile result is similar to the celerity profile result.

4.5 Estimation of incident wave angle

Incident wave angle can be estimated by conventional 2-D (frequency and direction) spectral analysis (Longuet-Higgins et al., 1963 among others). This directional wave spectrum analysis uses the assumption that the wave field is stationary over the time period considered. Hence, the directional spectrum analysis cannot provide time varying dominant wave angles required to comply with the wave-by-wave approach in the present study.

In this study, incident wave angles are estimated by extracting linear wave crest signatures in the space domain. The direction of incident waves is assumed to be perpendicular to elongated wave crests. Thus, the incident wave angle at a location is obtained by computing directions of the elongated wave crests, i.e. slopes of the wave crest lines in the real world coordinates.

In order to obtain incident wave angle profiles of individual waves, their crest trajectories and processed image sequence are used. Figs. 32 and 33 present the procedure to obtain the incident wave angle profile for each wave crest trajectory from the sequential processed images. To begin with, using space-time information of each crest trajectory in the timestack domain, the crest location at each time

point (for instance, i^{th} time point in the t-axis) is obtained as shown in Fig. 32(a). Thereafter, the processed image corresponding to each time point is called in to extract the elongated crest feature starting from the crest location (Fig. 32(b)).

Instead of using the rectified-processed images, the unrectified-processed images are used to extract the crest feature in this study, since the unrectified images have better homogeneous image quality. Extraction of the elongated crest feature is conducted within the sub-window of 51 $\times$ 51 pixel size centered at the crest location as shown in Fig. 32(b)(d).

The crest feature is extracted by tracing pixels of highest intensity values within a movable interrogation window of 3 $\times$ 2 pixel ($H \times W$) size as shown in Fig. 32(c). The interrogation window is moved to both directions, first to the right, second to the lelf, starting from the center point, searching for highest intensity pixels. For the first half search, the left center cell of the interrogation window is placed at the center of the sub-window, and the cell of the highest intensity value in the rest 5 pixels is selected as the next location for the left center cell of the interrogation window. Thereby, the right half of the crest feature is extracted by tracking the newly detected highest intensity pixels. Similarly, the left half of the crest feature is extracted by moving the interrogation window to the left direction. Fig. 32(d) presents the extracted feature of the elongated wave crest within the sub-window.

After the wave crest feature is extracted in the image frame, the feature is rectified into the real world coordinates by the DLT method of Holland et al. (1997) which is used to generate the cross-shore image timestacks in Chapter III. The feature in the rectified domain is filtered and interpolated using the cubic smoothing spline method, since the feature is re-sampled in the rectified frame by the rectification process, having discontinuity points in it. The line (thick red) centered within the box (dark green) of 10 m $\times$ 10 m size in Fig. 33 is the crest feature obtained after image rectification and the smoothing-spline based curve fit to the extracted crest

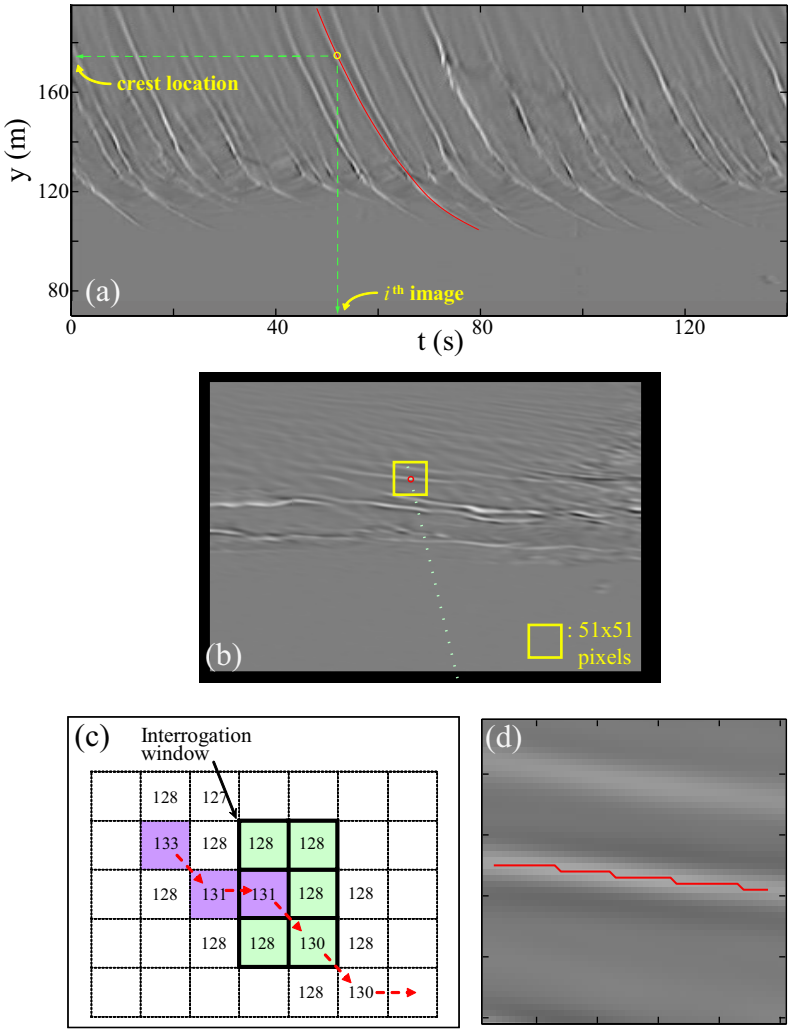

Figure 32: Extraction of the elongated wave crest feature in the image domain for wave angle estimation: (a) a wave crest trajectory in the timestack domain to obtain the crest location at each time point, (b) unrectified-processed image corresponding to each time point with (yellow box) sub-window, (red circle) the crest location, and (green dotted line) cross-shore transect, (c) tracing highest intensity pixels using the interrogation window of 3 $\times$ 2 pixel size (number in each cell represents image intensity), (d) (red line) the elongated wave crest feature extracted in the sub-window image.

feature as shown in Fig. 32(d).

The incident wave angle θ along the cross-shore transect is obtained by computing the slope of the crest feature, i.e. the first derivative of the feature as shown in Fig. 33(b). Fig. 33(c) presents the estimated incident wave angle profile using the sequential wave crest features in Fig. 33(a) extracted along the crest trajectory in Fig. 32(a). Throughout the present study, the wave angle for the cross-shore direction normal to the shore line is set to be 0°, the counterclockwise direction from the cross-shore transect is set to be positive up to 180°, and the clockwise direction is set to be negative up to −180°. In addition, the estimated wave angle profiles are mean-filtered and linearly interpolated using a sliding window 10m-long, since the estimated wave angle at each time point is not continuous along the cross-shore transect as shown in Fig. 33(c).

4.6 Results and discussion

Wave celerity, period, wavelength, and incident angle were estimated using a wave-by-wave approach, with individual wave crest trajectories identified in the space-time timestack domain. Wave celerity, wave period, and wavelength profiles corresponding to each wave crest trajectory were obtained from each of the four video datasets respectively. Incident wave angles were estimated in Cases 1 and 2 which have relatively larger angles deviating from the shore normal direction than the other two cases. In this subsection, the results of the estimated wave celerity profiles are compared to the linear wave theory-based wave celerity computed using the measured beach profile. The estimated wave period results are compared to the wave periods obtained from the pressure head data measured by the instruments. In addition, the incident wave angle results are compared to the results by directional wave spectrum analysis. The

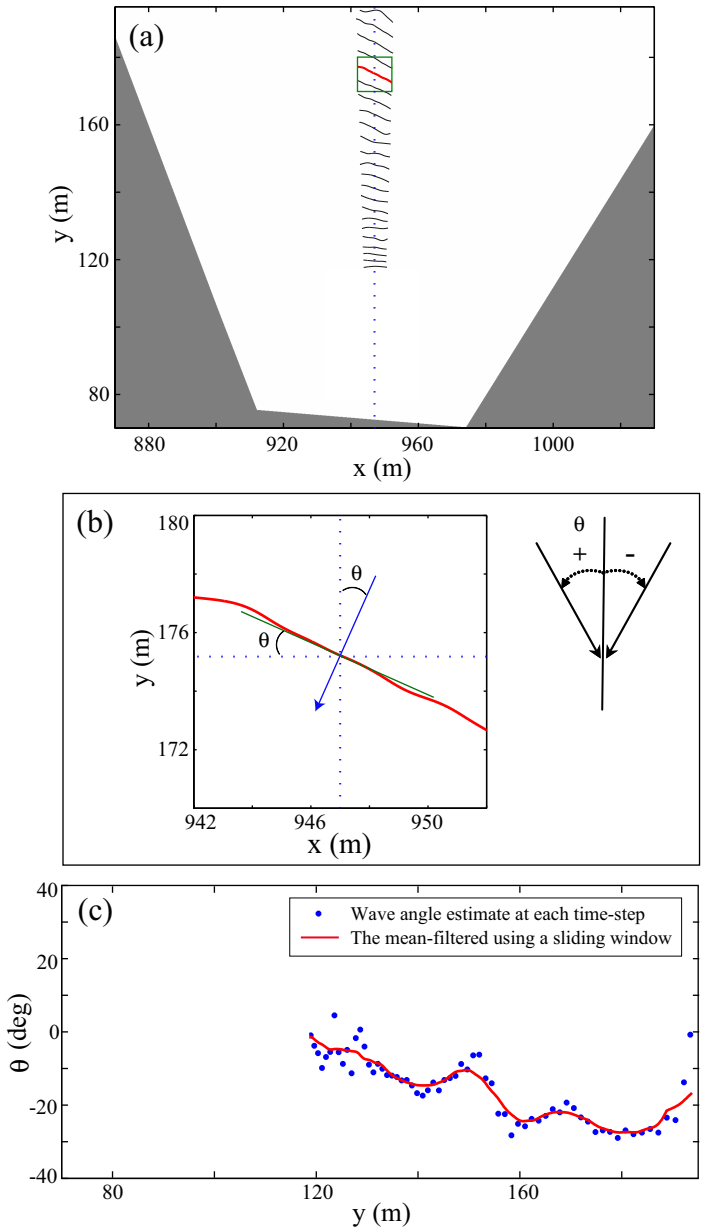

Figure 33: Incident wave angle estimation using the extracted wave crest feature: (a) extracted wave crest feature sequence with 1s time-step increment along the crest trajectory in Fig. 32(a), (b) incident wave angle measurement, (c) incident wave angle profile obtained using the wave crest feature sequence in (a).

wavelength results are not presented, since the wavelength is computed by the product of the celerity and the wave period, and comparisons in the celerity and the wave period results with the in-situ measured data reflect comparison of the wavelength results to in-situ measurements indirectly.

4.6.1 Results of wave celerity estimation

The estimated wave celerity results obtained from each of the four video datasets are compared to the wave celerity results computed from the in-situ measured water depths (h_m) using shallow water linear wave theory. In addition, the video-based wave celerity results at the instrument locations are compared to the measured nonlinear shallow water wave equation-based wave celerity approximation (hereafter, referred to nonlinear celerity measurement), since wave height data are available only at the locations of the deployed instruments. When pressure datasets collected by two closely spaced instruments are available, more direct in-situ measurements of wave celerity can be accomplished by applying the cross-spectral analysis (Holland, 2001) to the pressure data. In this case, the pressure data should be sampled synchronically by the two instruments, ideally at the same sampling rate. However, the instruments used in 2003 Myrtle Beach measurements had time drifting problems during wave data collections. The cross-spectral method was tested to the pressure data measured by Aquadopp B and C of the four datasets, but the celerity results of two dataset cases were unreasonably smaller than the linear wave theory-based celerity, indicating inexact synchronization of the sampling timing of the instruments. Thus, pressure data-based celerity estimation is not considered for comparisons with the video-based celerity estimation in this study.

Due to the wave celerity transition across the breaker point, the individual celerity profiles in each of the four datasets had to be adjusted using Eq. 26 across the wave

celerity transition distance, L_b, prior to comparisons with in-situ measurements. The original celerity profiles in each of the four datasets were grouped into the three wave breaking groups using the k-means clustering method, resulting in the three representative celerity profiles locally-averaged for each of the three wave breaking groups as shown in Figs. 34 through 37.

The region of wave breaking in each breaking group was determined by utilizing the three representative celerity profiles locally-averaged such that the local celerity peak of each groups celerity profile should be located in that breaking region. The breaker points of individual waves in the inner breaking group were not detected, since their breaking events generally happen in the saturated breaker zone covered with white foam. Table 5 presents the results of grouping the celerity profiles into the three groups and the breaker point detection of each of the four datasets.

The numbers of the extracted realistic wave crest tracks (N_v^t) in each of the four datasets were regarded to approximate the number of the first highest 2/3 wave heights ($N_{2/3}$) in in-situ measured records in Chapter III. The inner breaking waves which were discarded from the breaker point detection are considered to have smaller wave heights than the waves in the other two groups, since wave breaking in shallow water are depth-dependent.

In Table 5, the detected breaker points are from the intermediate and the outer breaking groups, and the number of the wave celerity profiles having the detected breaker points (N_v^d) is approximately 0.42 times the number of waves in in-situ measured records ($\simeq 0.42N_w$ or $N_{2/5}$) with the range of $0.35 \sim 0.52N_w$. This fact suggests that the wave property statistics derived from the wave celerity profiles having the detected breaker points can be approximately compared to the wave statistics obtained from the first highest 1/3 waves ($N_{1/3}$), even though there is small difference in wave numbers between them as many as $N_{2/5} - N_{1/3} = 0.067N_w$. Hence, for comparisons

Table 5: Results of wave celerity profile grouping and wave breaker point detection.

Case No.	Breaking group	N_v^t	N_v^g	N_v^u	N_v^d	N_w	N_v^d / N_w
I	outer	203	73	8	116	302	0.38
	interm.		51	-			
	inner		79	79			
II	outer	266	74	-	191	415	0.46
	interm.		117	-			
	inner		75	75			
III	outer	147	36	-	91	259	0.35
	interm.		55	-			
	inner		56	56			
IV	outer	196	52	1	131	253	0.52
	interm.		80	-			
	inner		64	64			
Notes		N_v^t : number of the wave celerity profiles. N_v^g : number of the crest tracks in each group. N_v^u : number of the undetected breaker points in each group. N_v^d : number of the celerity profiles having breaker points. N_w : number of waves in in-situ measured record.					

between the video-based celerity estimates and the field data-based celerity approximations, the significant wave heights (H_s or $H_{1/3}$) are used to compute the nonlinear shallow water wave equation-based celerity approximation with the measured water depths (h_m) in this study.

Using the detected breaker points, the wave celerity transition of each wave celerity profile in the intermediate and the outer breaking groups was adjusted using Eqs. 25 and 26. The locally averaged of the adjusted individual celerity profiles in the intermediate and the outer breaking groups of each of the four datasets are presented in Figs. 34 through 37. In Figs. 34 through 37, big gaps between the original celerity profiles and the adjusted celerity profiles of the intermediate and the outer breaking groups were caused by adjusting the celerity transitions over the breaking areas. The areas with those big celerity gaps along the cross-shore indicate that wave breaking events densely occur in those areas. Having densely populated breaker points. In general, the breaker points are observed at the locations of sand bars having steep-sloped seaward front faces.

In order to compare the video-based celerity results with in-situ measurements, linear wave theory-based celerity (c_l) derived from measurements was computed using the measured water depths by shallow water linear wave theory, i.e. $c_l = \sqrt{g \cdot h_m}$. In addition, considering the nonlinear wave amplitude dispersion effects on the wave celerity in shallow water for comparisons, the measured nonlinear shallow water wave equation-based local celerity (or the nonlinear celerity measurement) c_{non} was calculated by $c_{non} = \sqrt{g(h_m + H_{1/3})}$ using the measured significant wave heights and water depths. The nonlinear celerity measurement are available only at the locations of the deployed instruments in the cross-shore transect. The maximum wave heights H_{max} and the root-mean-squared wave heights H_{max} obtained from the in-situ measured pressure head data were also used to present the possible range of the nonlinear amplitude effects in the video derived nonlinear shallow water wave equation-based

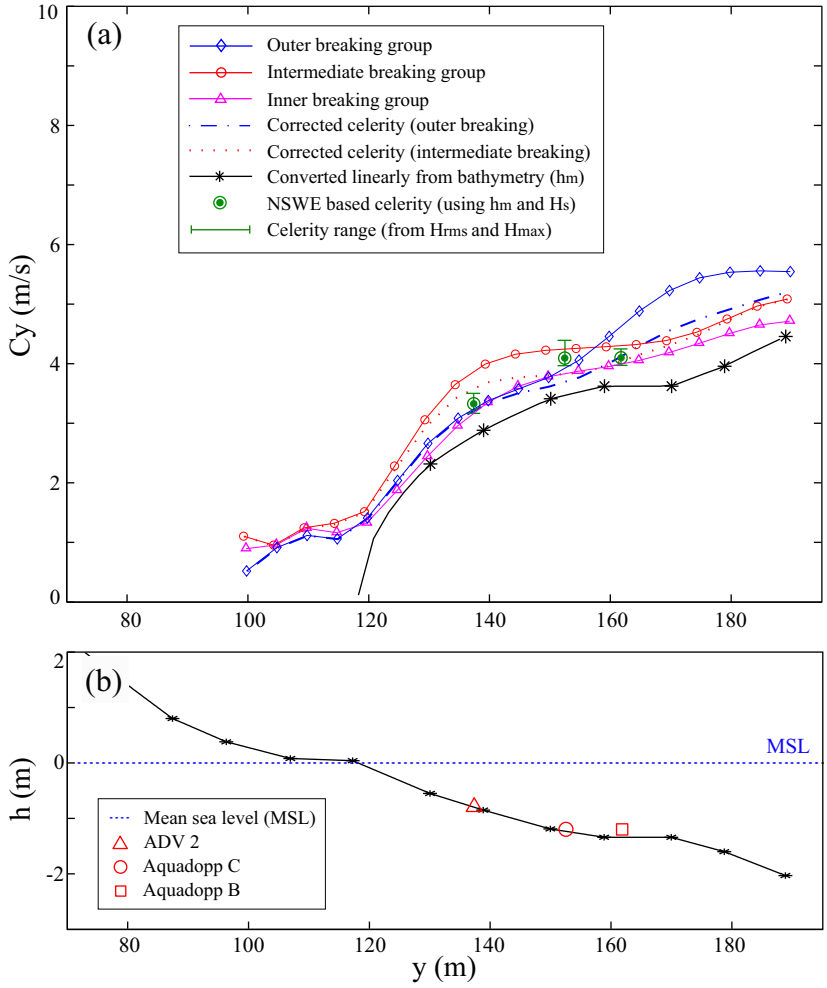

Figure 34: Comparisons of video-based wave celerity and the computed celerity from in-situ measurements in Case 1: (a) the locally averaged individual celerity profiles in each breaking group and the wave celerity computed from in-situ measurements, (b) the measured beach profile.

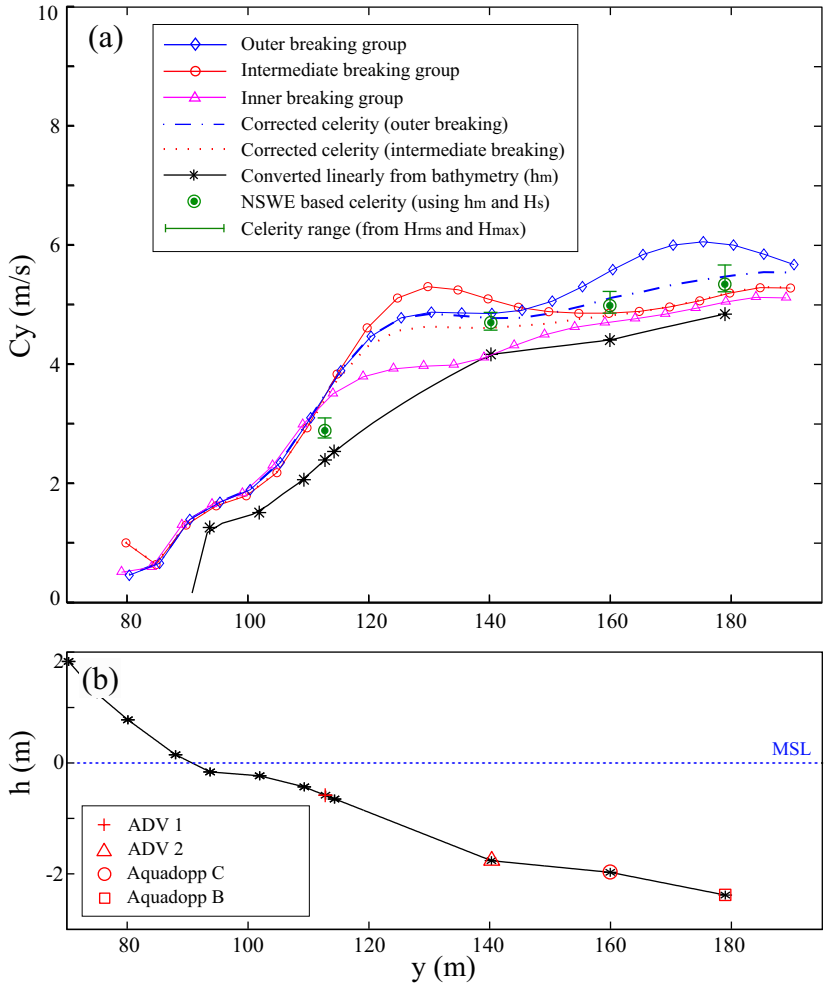

Figure 35: Comparisons of video-based wave celerity and the computed celerity from in-situ measurements in Case 2: (a) the locally averaged individual celerity profiles in each breaking group and the wave celerity computed from in-situ measurements, (b) the measured beach profile.

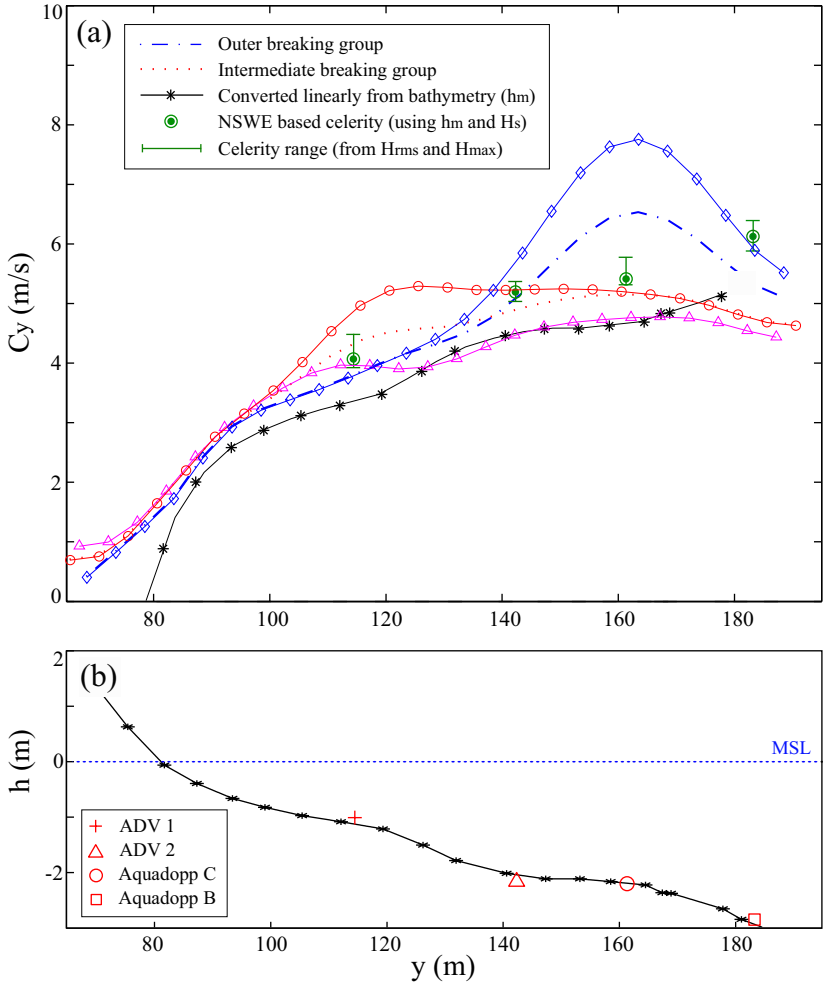

Figure 36: Comparisons of video-based wave celerity and the computed celerity from in-situ measurements in Case 3: (a) the locally averaged individual celerity profiles in each breaking group and the wave celerity computed from in-situ measurements, (b) the measured beach profile.

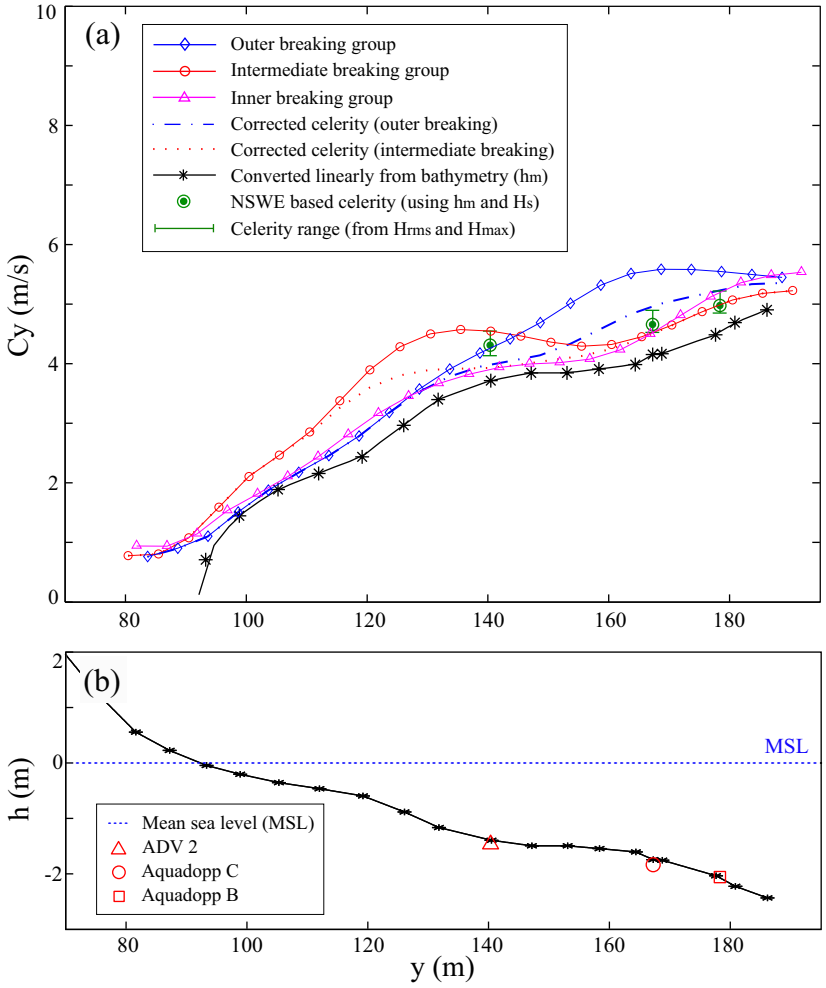

Figure 37: Comparisons of video-based wave celerity and the computed celerity from in-situ measurements in Case 4: (a) the locally averaged individual celerity profiles in each breaking group and the wave celerity computed from in-situ measurements, (b) the measured beach profile.

local celerity estimates.

From the comparisons in Figs. 34 through 37, it is seen that the estimated wave celerity results of the three celerity profiles (the inner, the adjusted intermediate, and the adjusted outer profiles) of each of the four datasets are generally larger than the wave celerity computed via linear theory. These over-estimates indicate that the video-based wave celerity estimates include the nonlinear amplitude dispersion effects. Compared to the wave celerity computed using the nonlinear shallow water wave theory, the two adjusted video-based celerity profiles in each of the four datasets are in the range of the nonlinear celerity computed using the wave height data. It means that the video-based wave celerity results were estimated reasonably including the nonlinear amplitude dispersion in the surf zone, i.e. in shallow water.

Table 6 summarizes the comparisons of the video-based celerity results and the in-situ measurement celerity results obtained from the measured water depth and wave data. The comparisons used the celerity values obtained at the locations of the deployed instruments, since the nonlinear celerity computed using the wave height data were available only at those locations. The quantified comparisons were expressed in terms of the normalized absolute celerity errors ε_l and ε_{non}:

$$\varepsilon_l = \frac{|c_v^m - c_l|}{c_l} \tag{28}$$

$$\varepsilon_{non} = \frac{|c_v^m - c_{non}|}{c_{non}} \tag{29}$$

where c_v^m is the mean of the 2 adjusted celerity values (c_v^i and c_v^o) of the video-based celerity estimates at each instrument location.

Compared to the linear wave theory-based celerity, the video-based celerity estimates have the error (ε_l) of averagely 12.3 %, being over-biased primarily due to the inclusion of the nonlinear amplitude dispersion effects. However, the error (ε_{non}) is significantly reduced to 2.6 % in average with the comparisons with the nonlinear

Table 6: Comparisons of video-based celerity and in-situ measurement-based celerity estimates (celerity unit : m／s).

Case No.	Instrument location	C_v^i	C_v^o	C_v^m	C_l	C_{non}	ε_l	ε_{non}
I	△	3.61	3.22	3.42	2.78	3.32	13.5 %	2.7 %
	○	3.83	3.69	3.76	3.47	4.10		
	□	4.04	4.13	4.08	3.62	4.11		
II	+	3.39	3.47	3.43	2.39	2.89	14.2 %	1.5 %
	△	4.59	4.75	4.67	4.16	4.69		
	○	4.79	5.09	4.94	4.39	4.97		
	□	5.16	5.45	5.31	4.83	5.33		
III	+	4.31	3.78	4.04	3.35	4.07	9.9 %	5.3 %
	△	4.88	5.06	4.97	4.47	5.19		
	○	5.14	6.50	5.82	4.65	5.41		
	□	4.74	5.32	5.03	5.38	6.13		
IV	△	3.91	3.97	3.94	3.69	4.30	11.4 %	1.0 %
	○	4.48	4.95	4.72	4.14	4.65		
	□	4.98	5.22	5.08	4.52	4.96		
Notes	+, △, ○, □ : locations of the deployed instruments ADV 1, ADV 2, Aquadopp C, and Aquadopp B in y (m) respectively. C_v^i : corrected celerity of intermed. breaking group at the instru. locations. C_v^o : corrected celerity of outer breaking group at the instrument locations. C_v^m : the mean of C_v^i and C_v^o. C_l : celerity by the linear wave theory (using h_m) at the instrument locations. C_{non} : NSWE celerity approxi. (using h_m and H_s) at the instrument locations. ε_l : the normalized absolute error between C_v^m and C_l. ε_{non} : the normalized absolute error between C_v^m and C_{nsw}.							

celerity measurements, confirming the reasonable inclusion of the amplitude effects in the video-based celerity estimates. In the comparisons of the video-based estimates and the nonlinear celerity measurements, relatively big discrepancies are observed around the areas of the densely populated breaker points, or in the region of wave celerity transition as observed in Figs. 34 through 37. The video-based celerity estimates were still over-estimated compared to the nonlinear celerity measurements over the celerity transition distances, even though they were adjusted using Eq. 25. Those over-estimates indicate that the ratio r_c of the accelerated celerity to the nonlinear shallow water equation based celerity approximation across the wave breaking area, as modeled to be 1.2, is still low for wave field conditions of the datasets used in this study. The error can be reduced, if the ratio r_c is determined properly for these wave conditions of the datasets.

4.6.2 Results of wave period estimation

For comparisons of the wave period estimates and the in-situ measurements, the median value (T_t^{median}) of the transient peak period map within 5m from the offshore boundary in each case of the four datasets was computed. The mean value (T_t^{mean}) was also computed, and the T_t^{mean} values were almost the same to the T_t^{median} values. So, the T_t^{mean} values are not presented. The T_t^{median} values of the four datasets were compared to the significant wave periods T_s and the mean periods T_m obtained from the water pressure data collected by the offshore instrument (Table 7).

The comparisons in Table 7 show that the T_t^{median} values of the four datasets are comparable to the in-situ measured wave periods T_s and T_m in general, having wave period differences of less than 0.5 s except the difference between T_t^{median} and T_m of Case 1. The relatively big disagreement between T_t^{median} and T_m in Case 1 may be due to a broad-banded spectrum, compared to the other 3 cases. In addition, the

Table 7: Comparisons of the transient peak period estimates obtained from video intensity data and the wave periods computed from wave pressure data.

Case No.	I	II	III	IV
T_s (s)	8.2	5.6	8.4	8.3
T_m (s)	6.4	5.2	7.9	8.0
T_t^{median}(s)	8.4	5.1	8.1	8.1
Water depth* (m)	1.09	2.31	2.78	2.11
Notes	* : depth of Aquadopp B.			

T_t^{median} values are observed to be more consistent with the significant wave periods T_s computed in the frequency domain rather than the mean periods T_m, even though both T_t and T_m were determined in the time domain. This suggests that the peak periods computed in the frequency domain can be also evaluated using the transient peak periods computed in the time domain by the wavelet analysis.

In order to verify validity of the transient peak periods T_t computed from the original image intensity time-series by the wavelet analysis, the wavelet analysis spectra of the intensity time-series were compared to those of the in-situ measured pressure head time-series. For this comparison, the image intensity data sampled at a location in the offshore area of the dataset Cases 2 and 4, and the wave pressure data collected by the offshore instrument of those two dataset cases were selected. Wave conditions of Cases 2 and 4 were contrasted each other, having shorter periods wide-banded and longer periods narrow-banded, respectively. Since the image intensity and the wave pressure data were sampled at different time phases, both datasets were synchronized by the cross-correlation method.

The results of the wavelet analysis results in Cases 2 and 4 are presented in Figs. 38

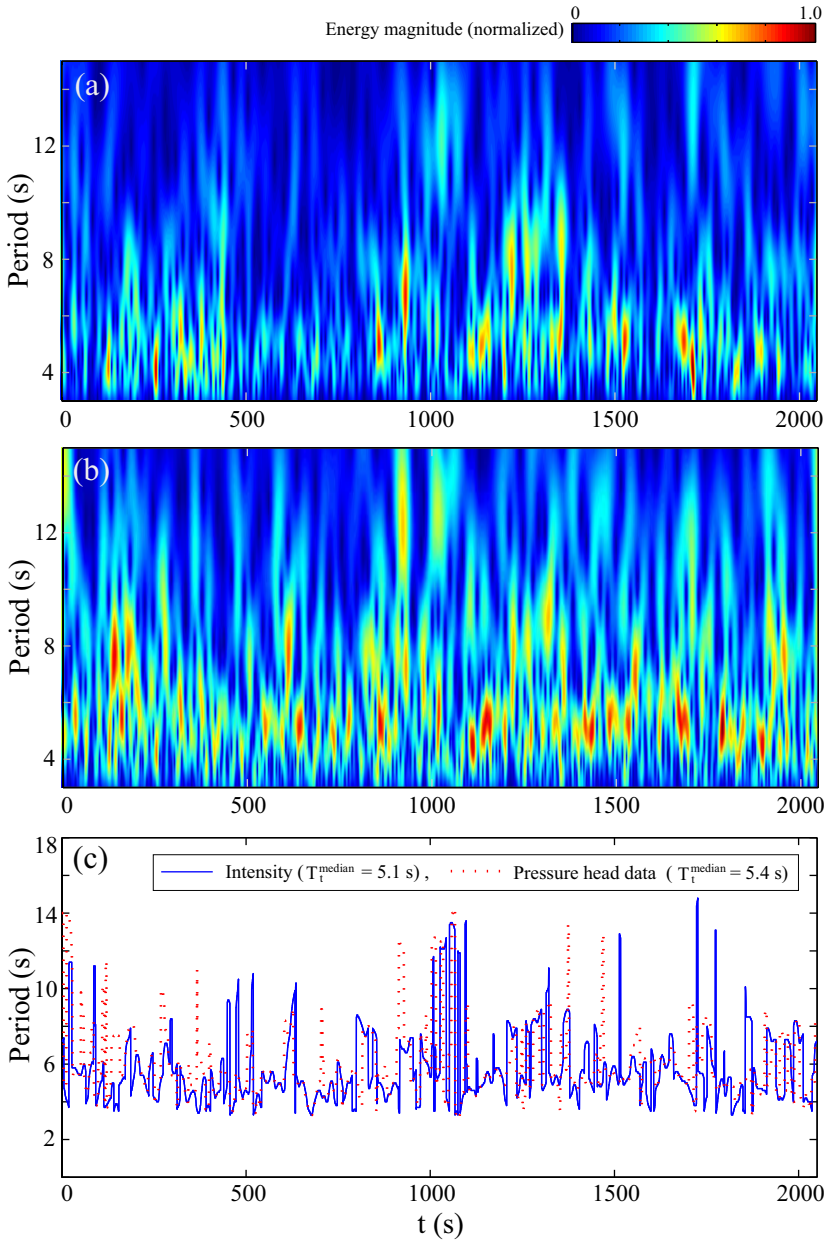

Figure 38: Comparisons of wavelet analysis spectra of image intensity and water surface level 1-D arrays for Case 2: (a) wavelet spectrum of intensity data, (b) wavelet spectrum of pressure head data, (c) comparisons of the transient peak period time-series in the two wavelet spectra.

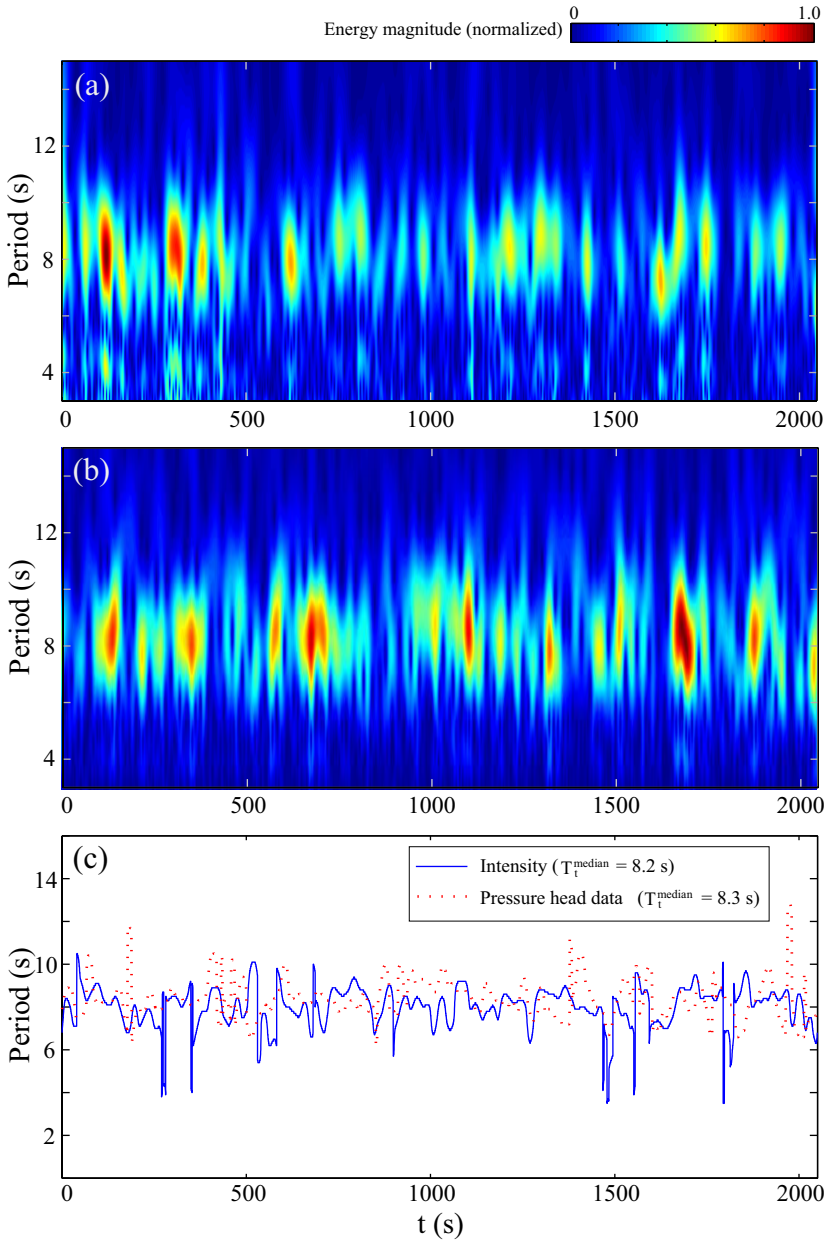

Figure 39: Comparisons of wavelet analysis spectra of image intensity and water surface level 1-D arrays for Case 4: (a) wavelet spectrum of intensity data, (b) wavelet spectrum of pressure head data, (c) comparisons of the transient peak period time-series of the two wavelet spectra.

and 39 respectively. The wavelet spectra patterns of the intensity data in both cases match well the wavelet spectrum patterns of the water surface level data as shown in Figs. 38(a)(b) and 39(a)(b). In the same context, Figs. 38(c) and 39(c) confirm that the transient peak period time-series of the intensity data of both cases have almost the same trends to those of the pressure data. The wave frequency spectrum for Case 4 is narrow-banded such that the transient peak period time-series of the intensity and the water level data vary within 1 s around the median wave period value of 8.3 s in general. The transient peak period time-series of the intensity and the wave data in Case 2 having the relatively wide-banded frequencies vary significantly approximately from 4 to 12 s. The median values of the two transient peak period time-series are 5.1 and 5.4 s respectively, and the wave periods at some time points are deviated even beyond 12 s. The two transient peak period time-series show a good noticeable trend match, having temporally longer peak periods larger than 12 s at the same moment.

As shown in the comparisons using the transient peak period time-series, application of the wavelet analysis to image intensity time-series to comply with the wave-by-wave approach will be meaningful in case of wave conditions having wide-banded spectra. However, narrow-banded wave cases may not need the wavelet analysis to provide transient wave periods, since variation of the transient wave periods is not significant and frequency dispersion is negligible in shallow water. These facts suggest that the peak period of a narrow-banded spectrum by the spectral frequency analysis can be also used as a sole period for each wave crest trajectory in the timestack domain for the depth inversion with a wave-by-wave approach. In this study, the transient peak periods by wavelet analysis were used

4.6.3 Results of incident wave angle estimation

The dataset Cases 1 and 2 were used to measure incident wave angles remotely, since they exhibited relatively larger angles than the other two dataset cases. Estimated incident angles in both cases were compared to in-situ measured directional wave energy spectra.

The direction of waves propagating in the surf zone is known to be almost normal to the shoreline. The rectified video image sequences of the four cases confirms this, even though the two Cases 1 and 2 showed relatively larger angles in the offshore region. Fig. 40 presents directional wave energy spectra of the four dataset cases obtained from Aquadopp C, deployed close to the seaward surf zone boundary. The directional wave spectra were analyzed from the pressure and horizontal components of wave velocities using the Iterated Maximum Likelihood Method. The waves in Cases 3 and 4 are narrow-banded, and their directions are almost normal (i.e. $\sim 0°$) to the shoreline. In contrast, the directional spectra in Cases 1 and 2 are wide-banded, having relatively larger angles in the ranges of approximately $-45 \sim 15°$ and $0 \sim 45°$ respectively. Table 8 presents the wave angles computed using the directional wave spectra of the two dataset cases. The peak frequency angle θ_p and the dominant incident angle θ_m were computed from each directional spectrum. The dominant incident angle is defined as the direction with the highest energy integrated over all frequencies. θ_m was computed by converting the 2-D wave energy spectrum $E(f, \theta)$ into the 1-D spectrum $E(\theta)$ through summing up each f-axis column of $E(f, \theta)$. θ_m is the angle having the highest energy in $E(\theta)$.

Since the instruments ADV 1 and ADV 2 of the two dataset cases were deployed in the area of vigorous turbulence, wave directions computed using their data were unreasonably larger than 0°. Hence, their angle measurements were discarded. In addition, wave velocity data of the Aquadopp B were not available to compute the directional spectrum. So, only directional wave spectra obtained from wave data of

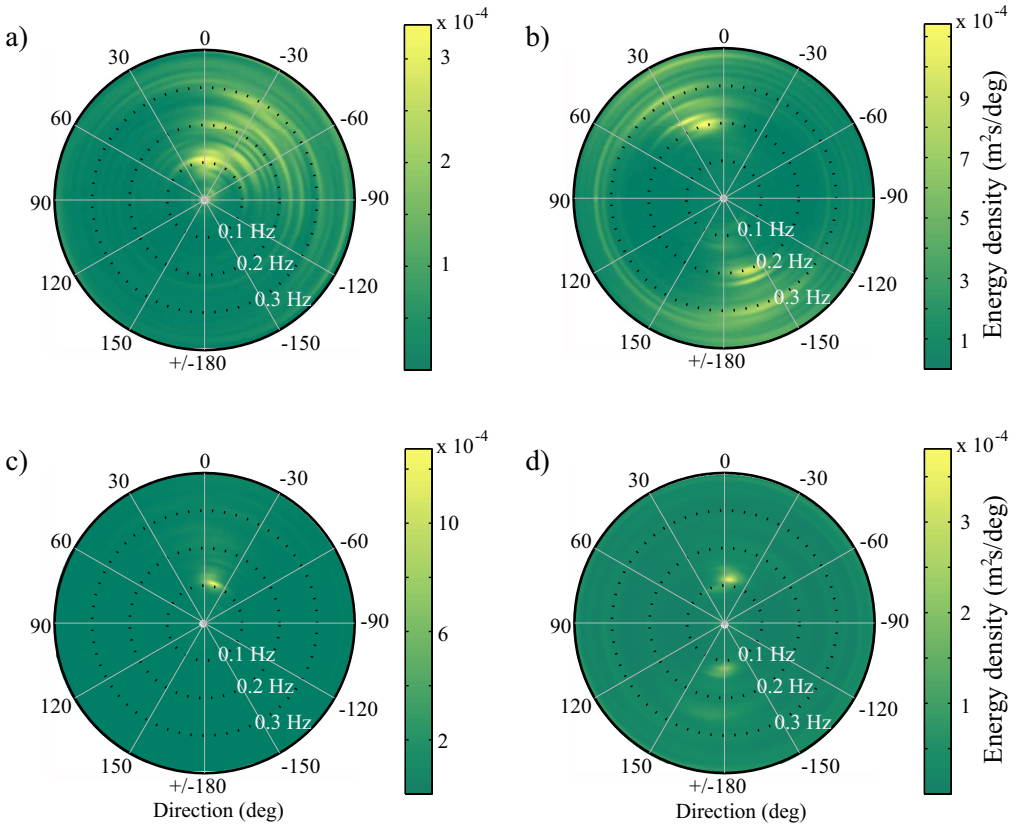

Figure 40: Directional wave spectra obtained from the pressure and the horizontal velocity component data measured by Aquadopp C: (a) Case 1, (b) Case 2, (c) Case 3, (d) Case 4.

the Aquadopp C were used for comparison between the remotely measured and the in-situ measured wave angles.

Figs. 41 and 42 present results of the wave angle profiles estimated using the individual wave crest trajectories and the processed image sequences and their comparisons, with in-situ measured wave angles. The incident wave angle profiles in Figs. 41 and 42 show the locally averaged wave angle profiles estimated from video imagery. In general, the video-based wave angle estimates at the deployed instrument locations are comparable to the in-situ measured angles. In particular, the estimates show better agreements with the dominant incident wave angles rather than the peak

Table 8: Incident wave angles of Cases 1 and 2 computed from the wave data collected by the deployed instrument Aquadopp C.

Case No.	θ_p (deg)	θ_m (deg)	T_s (s)	H_s (m)	h (m)	y (m)
I	-39	-32	8.9	0.48	1.22	152.5
II	24	12	4.9	0.55	1.73	159.9
Notes	θ_p : incident wave angle of the peak frequency θ_m : dominant incident wave direction h : depths of the deployed instruments y : locations of the deployed instruments in the offshore direction					

frequency angles. This is because the video-based estimates were obtained by averaging the wave angle profiles for all incoming waves, in the same way the dominant wave was computed.

The video-based wave angle estimates along the cross-shore transect approach 0° around the shoreline, indicating that wave crests are getting refracted to be parallel to the shoreline, as waves propagating toward shallow water depths. Interestingly, the video-based wave angle estimates in Case 1 (Fig. 41) show abnormal increase of the wave angle magnitude in the swash zone above the mean sea level, caused by the geometry of the swash zone. In addition, the magnitudes of the wave angles decrease significantly over the distances of $120 \sim 130$ m and $110 \sim 120$ m in y in Cases 1 and 2 respectively, comparably to the wave celerity profiles in Figs. 34 and 35. This is due to rapid decrease of wave celerity caused by the sudden water depth changes in those areas.

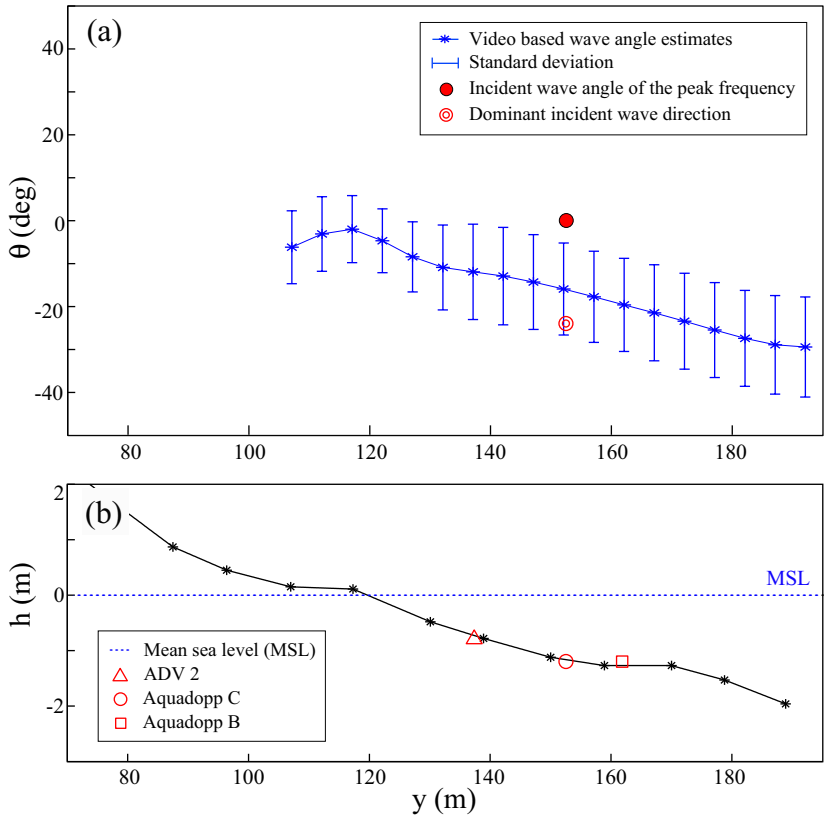

Figure 41: Comparisons of the video-based wave angle estimates and in-situ measuremtns: (a) incident wave angle profile obtained from video image data and in-situ measured wave angles, (b) beach profile and deployed instrument locations.

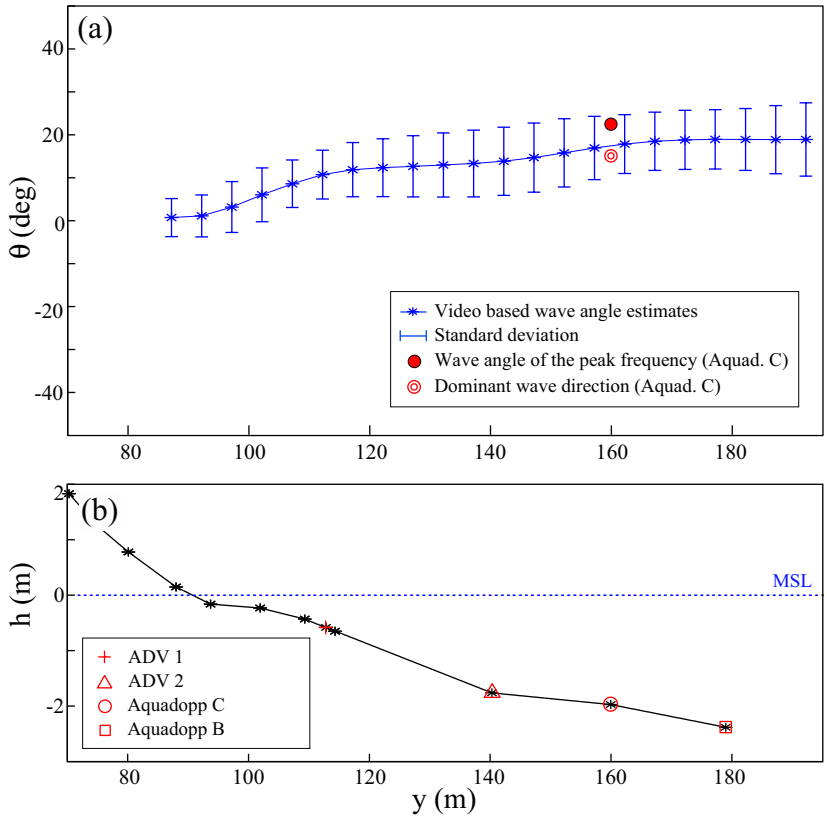

Figure 42: Comparisons of the video-based wave angle estimates and in-situ measuremtns: (a) incident wave angle profile obtained from video image data and in-situ measured wave angles, (b) beach profile and deployed instrument locations.

4.7 Summary

Wave celerity, wave period, wavelength, and incident wave angle were estimated with a wave-by-wave approach by utilizing the individual wave crest trajectories extracted in the space(y)time(t) domain of the processed image timestacks for the four datasets.

The wave celerity was computed by taking the first derivative (local slope) at each location point in y of the wave crest trajectories. The estimated wave celerity showed wave celerity transition across the breaker points up to 1.2 times larger than the nonlinear shallow water wave equation-based celerity. The wave celerity transition across the breaker points were adjusted based on the previous wave celerity investigations. The sole wave period for each wave under the random wave circumstance was determined by applying the Morlet wavelet analysis to 1-D arrays of intensity time-series and obtaining its corresponding transient peak period. The wavelength for each individual celerity profile was obtained by multiplying the wave phase speed C by its sole wave period: $L(y) = C(y) \times T$. The incident wave angle profiles of individual waves were estimated along the cross-shore transects by utilizing their crest trajectories and processed image sequences.

The video-based celerity estimates had the mean relative error of about 12.3% over-biased due to the inclusion of the nonlinear amplitude dispersion effects, compared to the linear wave theory. However, the mean relative error was significantly reduced to 2.6% in average in comparison with the in-situ measured nonlinear celerity. The median values of the transient wave period estimates from the image intensity arrays was well compared to the significant wave periods T_s and the mean periods T_m obtained from the water pressure data, having wave period differences of less than 0.5s in general. The video-based wave angle estimates at the instrument locations were well compared to the wave angle measurements (the peak frequency directions and the dominant wave directions) computed by directional wave spectrum analysis. In particular, the estimates showed better agreements with the dominant incident

wave angles, since the video-based estimates were averaged for all detected incoming waves.

CHAPTER V

NONLINEAR DEPTH INVERSION MODEL

5.1 Introduction

Waves approaching the shore become highly nonlinear in the surf zone, and their phase speeds are strongly influenced by the nonlinearity. Holland (2001) showed that exclusion of the nonlinear amplitude dispersion effects can commonly cause the error of inverted depths in shallow water ($h < 4$ m) to be up to 50%. For those reasons, the nonlinear effects must be taken into account for depth inversion in the shallow region.

Previous works for depth inversion using remotely collected wave image data (Dugan, 1997; Williams and Dugan, 1997; Stockdon and Holman 2000) adopted the linear dispersion relation, since actual water level data is not available by the remote sensing platforms. In order to perform nonlinear depth inversion in shallow water, Catalan (2005) sampled a hybrid data set composed of wave period and phase speed data retrieved from wave imagery and water surface elevation time-series generated by the combined refraction/diffraction model REF/DIF1 (Kirby and Dalrymple, 1994). The model requires input of wave amplitudes at the offshore boundary which cannot be provided by the remote sensing.

The present study includes the nonlinear amplitude dispersion effects in the depth inversion algorithm by retrieving wave amplitudes and water depths at the breaker points from nearshore video image sequences. The nonlinear depth inversion algorithm involves three primary model components: Wave Breaker Model (WBM), Wave Dissipation Model (WDM), and Wave Shoaling Model (WSM). Fig. 43 is a detailed

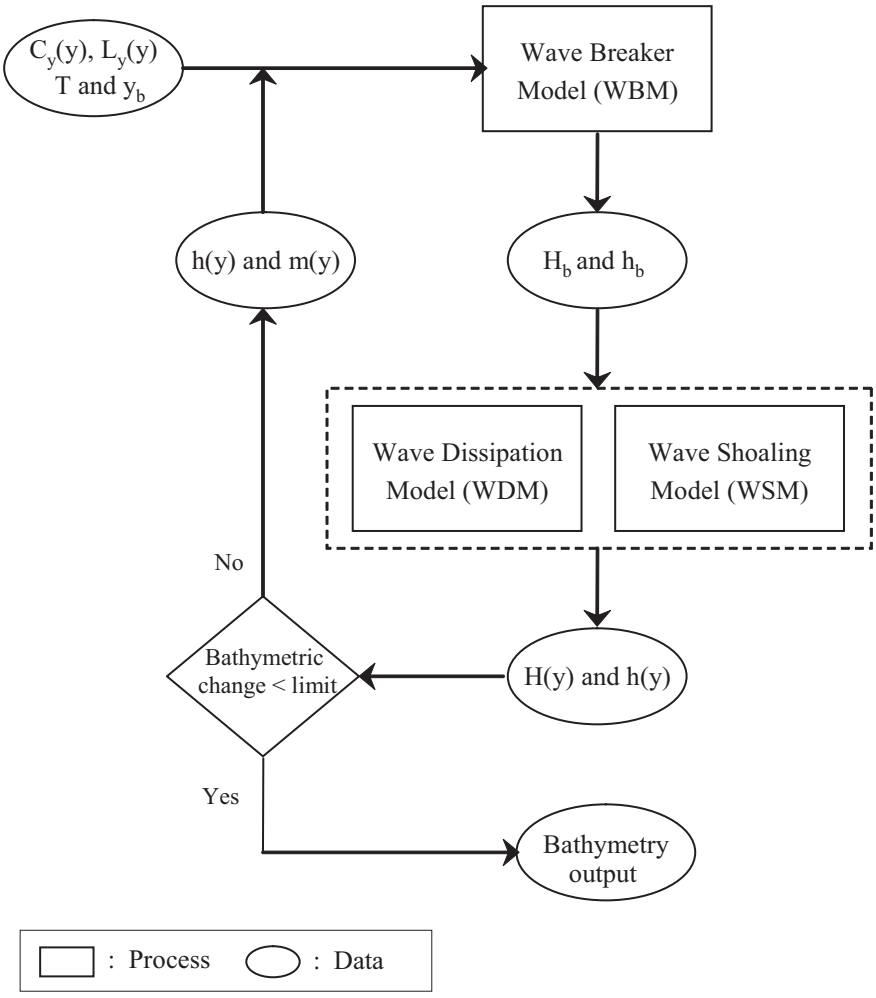

Figure 43: Flowchart of the nonlinear depth inversion algorithm involving Wave Breaker Model, Wave Dissipation Model, and Wave Shoaling Model.

flowchart of the nonlinear depth inversion algorithm with the three model components.

The Wave Breaker Model predicts breaking wave height H_b and breaker water depth h_b at the detected breaker point y_b from each celerity profile $c_y(y)$. The Wave Dissipation Model computes wave heights $H(y)$ dissipated starting from the breaker point in the shoreward direction. At the same time, it subtracts wave height contributions from the celerity profile, producing its water depth profile $h(y)$. The Wave Shoaling Model derives shoaled wave heights $H(y)$ and water depths $h(y)$ starting

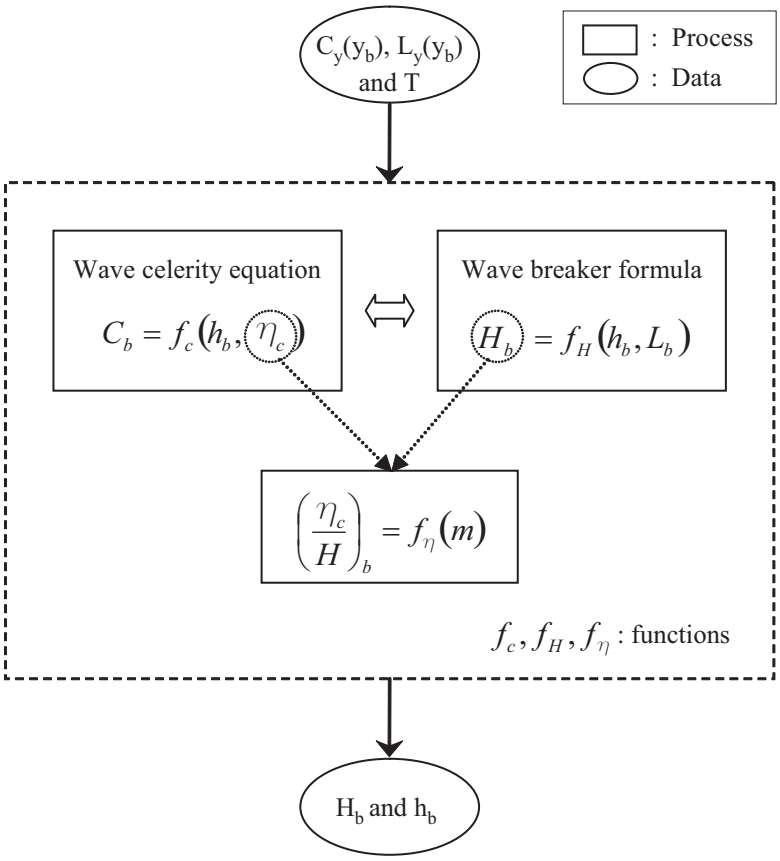

Figure 44: Components of the Wave Breaker Model along with inputs and outputs.

from its breaker point in the offshore direction. The beach profile is iteratively estimated by using the newly updated local water depths $h(y)$ and beach slopes $m(y)$.

5.2 Wave Breaker Model

The Wave Breaker Model predicts wave heights and water depths at the wave breaker points by using a nonlinear shallow wave theory-based wave phase speed equation and a wave breaker formula as shown in Fig 44. The two equations have two unknowns: H_b (or wave crest elevation η_c) and h_b. The other wave parameters such as $c_y(y_b)$ (or c_b) and L_b are obtained from a wave image sequence. Hence, the two unknowns of H_b and h_b can be determined by equating the two equations.

The ratio of η_c to H_b at the breaker point can be determined using a experimentally fitted function of local beach slope (m). Since the local beach slope cannot be

given before running of the depth inversion algorithm, however, the inversion algorithm is designed to be run iteratively, providing newly updated local beach slopes to calculate the ratios. The ratio is pre-set with a default value in the first run of the algorithm. The details in the Wave Breaker Model are described in the subsequent sub-sections.

5.2.1 Wave phase speed theory

Shallow water linear wave theory-based wave celerity, $C = \sqrt{gh}$, makes depth inversion straightforward. However, the inverted depths by Eq. 6 can be significantly over-predicted in shallow depths owing to the amplitude effects excluded in the equation, as found by the previous works (Suhayda and Pettigrew, 1977; Thornton and Guza, 1982; Holland, 2001).

In order to include the amplitude effects on wave propagation in shallow water, several nonlinear shallow water wave theory-based celerity approximations have been suggested. The approximated wave celerity based on the solitary wave theory (McCowan, 1891) is given as:

$$c = \sqrt{g\left(h_t + H\right)} \tag{30}$$

where h_t is the depth below wave trough. The solitary wave is assumed to have infinitely long wavelength and no boundary in wave channel. This assumption is not fully satisfied in the case of waves propagating in shallow water bounded by the beach. Thornton and Guza (1982) measured wave phase speed and wave heights in the surf zone, and compared the measured phase speed to the linear theory-based wave celerity. They found the ratio of water depths to root mean squared wave heights to be $H_{rms}/h = \gamma = 0.42$ in the saturated (inner) surf zone from their field measurements. They explained the difference between the measured (c_s) and linear

theory (c_L) based wave phase speeds by introducing the following equation:

$$c_s \leq \sqrt{gh} \cdot \left(1 + \frac{1}{2}\frac{H_{rms}}{h}\right) = c_L \cdot \left(1 + \frac{1}{2}\gamma\right) \approx c_L \cdot (1 + 0.21) \tag{31}$$

where γ is the saturated breaker parameter. Eq. 31 is slightly modified version of Eq. 30 as shown in follows (McCowan, 1891):

$$c = \sqrt{gh} \cdot \left(1 + \frac{1}{2}\frac{H}{h}\right) \approx \sqrt{gh\left(1 + \frac{H}{h}\right)} = \sqrt{g\,(h + H)} \tag{32}$$

Eq. 31 was introduced to compare the averaged of the measured phase speeds with the linear theory celerity. So, it is not suitable to be applied to individual wave cases. Madsen et al. (1997) suggested the more simplified from of Eq. 32 for regular waves only:

$$c = 1.3\sqrt{gh} \tag{33}$$

Holland (2001) derived the shallow water dispersion empirically from the cnoidal theory-based wave speed using the field data measured at the U.S. Army Corps of Engineers Field Research Facility, Duck, NC. Holland (2001) also suggested an empirical shallow water phase speed as follows:

$$c = \sqrt{g\,(h + \alpha \cdot H_s)} \tag{34}$$

where H_s is significant wave height and α is empirical coefficient. The coefficient value of α=0.48 showed the best fit for relation between the measured phase speeds and the actual depths in the surf zone shallower than 4 m. This phase speed is also established based on a statistical wave height rather than individual wave heights. In the present study, the wave phase speed equation (or local wave celerity) obtained from the characteristic form of the nonlinear shallow water equation is used:

$$c = \sqrt{g\left(h + \eta_c\right)} \tag{35}$$

where η_c is the wave crest elevation, since the instantaneous water surface level is consistent with wave-by-wave approach.

5.2.2 Wave breaker formula

The initiation of wave breaking in the surf zone is triggered when wave steepness cannot withstand the water column of a wave due to both the increase in wave height and the decrease in wavelength. Complexity of wave breaking mechanism makes theoretical description for the initiation of wave breaking very difficult. Nevertheless, a few theoretical expressions for the breaking initiation were derived under the concept that the wave phase speed begins to be overstepped by the horizontal component of the water particle velocity at the surface (McCowan, 1894; Miche, 1944). McCowan derived the well known breaking criterion from the solitary wave theory:

$$H_b = 0.78 \cdot h_b \tag{36}$$

where the subscript b indicates the breaker point. Since a solitary wave propagates above the still water level, h_b should be regarded as the trough elevation (h_{tb}) at the breaker point such that $H_b = 0.78 \cdot h_{tb}$. Kamphuis (1991) modified this solitary wave theory-based breaker criterion using the periodic wave concept. Assuming actual still water level (or h_b) lies halfway between the wave crest and tough, the breaker criterion $H_b = 0.78 \cdot h_{tb}$ becomes:

$$\frac{H_b}{h_b} = \frac{H_b}{h_{tb}}\frac{h_{tb}}{h_b} = 0.78\frac{h_{tb}}{\left(h_{cb} + h_{tb}\right)/2} = 0.56 \tag{37}$$

where h_{cb} is the crest elevation at the breaker point and equals $1.78h_{tb}$. Considering shoaled wave heights above the still water level near breaking points, as Kamphuis

(1991) suggested, the coefficient K_b of the solitary wave theory-based breaker criterion should be in the range of:

$$0.56 < K_b < 0.78 \tag{38}$$

The solitary wave theory-based breaker criteria represent only depth-induced wave breaking, and do not include the effects of wave steepness and beach slope on wave breaking. In contrast, Miche's breaking criterion for periodic waves was derived using small amplitude linear wave theory with inclusion of the frequency dispersion effects:

$$\frac{H_b}{L_b} = 0.14 \cdot tanh\left(2\pi\frac{h_b}{L_b}\right) \tag{39}$$

which approximates Eq. 36, if the term $\tanh(2\pi h_b/L_b)$ is simplified to $2\pi h_b/L_b$ assuming the very shallow water condition. Most of the breaker formulas including the two equations above have been established empirically or semi-empirically through calibration using laboratory data.

In random wave fields, wave breaking may happen at different locations across the wide surf zone, since individual waves have different heights and periods causing different steepness limits. Seyama and Kimura (1988) conducted flume experiments with consideration of unidirectional irregular waves and showed that individual zero-down crossing waves tended to break at a much smaller ratio of the wave height to water depth compared to the breaking criteria for regular waves. The breaking criterion reduction was found to be up to 30% regardless of the beach slopes. In this context, those theories established in the laboratory experiments with regular waves are not suitable to describe various wave breaking conditions in the random wave seas.

For irregular breaking waves in the field, a couple of the breaker formulas have been suggested, but no definitive investigation considering wave steepness and beach slope has been performed. Thornton and Guza (1983) investigated wave breaking

in the inner surf zone (or the saturated breaking zone) and suggested that a high proportion of waves should be breaking with the strong depth dependence as follows:

$$(H_{rms})_b = 0.42 h_b \tag{40}$$

In addition, H_{rms} statistics were compared to those of the first highest 1/3 wave height $H_{1/3}$, and showed a high correlation such that $H_{1/3} = 1.42 \cdot H_{rms}$ in the wave breaking zone. Using the relation between $H_{1/3}$ and H_{rms}, the above equation can be converted into:

$$\left(H_{1/3}\right)_b = 0.59 h_b \tag{41}$$

Similar observations for the ratio of the significant wave height to the water depth to be about 0.6 are found in other field research as well such as Wright et al. (1982), King et al. (1990), and Raubenheimer et al. (1996). Due to the strong depth and steepness dependence of wave breaking, larger waves were observed to more likely break, resulting in a greater proportion of higher breaking waves in the Rayleigh distribution. From the breaking wave height percent distribution of Thornton and Guza (1983), it is found that the breaking wave percentage among all incoming waves reduces from 100 to 10% in the outer surf zone as water depth increases from h_s to $2h_s$ where h_s is the depth at the seaward boundary of the saturated zone. In that depth range, in particular, the dominant breaking wave percent range are found to be approximately $20 \sim 40\%$, indicating that higher waves are breaking. Hence, Eq. 41 can be rewritten to be applied to wave-by-wave approach for indexing incipient wave breaking in the surf zone as follows:

$$H_b = 0.59 h_b \tag{42}$$

The above breaking criterion coefficient is consistent with Eq. 37 and Eq. 38 modified from the solitary wave theory-based breaker criterion. In addition, the breaker

coefficient reduction from 0.78 in Eq. 30 to 0.59 in Eq. 42 observed in laboratory experiments for irregular wave breaking is approximately 24%, being also consistent with those determined by Seyama and Kimura (1988).

In order to represent wave breaking induced by both the water depth and the wave steepness in irregular wave fields, Smith et al. (2001) modified the Miche criterion (Eq. 39) for the numerical spectral wave transformation model (STWAVE):

$$\left(H_{1/3}\right)_b = 0.1 \cdot L \cdot tanh\left(kh_b\right) \tag{43}$$

Based on the breaking wave height percent distribution in the surf zone (Thornton and Guza, 1983), similarly, the above equation can be assumed for individual waves:

$$H_b = 0.1 \cdot L_b \cdot tanh\left(kh_b\right) \tag{44}$$

From this equation, it is seen that the coefficient is reduced from 0.14 in Eq. 39 for regular waves to 0.1. This reduction is comparable to those determined by Seyama and Kimura (1988).

In this study, the modified Miche′s breaker formula (Eq. 44) is adopted to calculate wave heights and water depths at breaking points along with the nonlinear shallow water equation-based wave phase speed in Eq 35 as illustrated in Fig. 44, since the breaker formula represents both depth-induced and steepness-induced wave breaking over the entire surf zone and requires only local wave parameters which are provided from video imagery.

5.2.3 Ratio of crest elevation to wave height at the breaker point

The phase speed equation in Eq. 35 includes the wave crest elevation rather than the wave height. But, the breaker criterion (Eq. 44) is expressed in terms of the wave height instead of the wave crest elevation. Based on the linear wave theory, the

ratio of the wave height to the crest elevation is $\eta_c/H = 0.5$. In waves shoaling and breaking, wave asymmetry becomes pronounced, increasing wave skewness. Cnoidal wave theory predicts the ratio of η_c/H at the breaker point as high as 0.95, but measured values do not exceed 0.85 (Hansen, 1990). Hansen (1990) suggested an empirical formula for the ratio of η_c/H at the breaker point from experimental data on periodic waves:

$$\left(\frac{\eta_c}{H}\right)_b = 1 - 0.5 \cdot tanh\left(\frac{4.85}{\sqrt{U_b}}\right) \tag{45}$$

where U_b is the Ursell parameter at wave breaking, and approximated by $U_b = 10.1 \cdot m^{0.2} \cdot (H_o/L_o)^{-1}$. In the present study, the crest elevation is associated with the wave height using the above equation, even though the equation was established from laboratory experiments with regular waves. This is because no definitive study on the relation between the wave height and the wave crest elevation has not performed for irregular waves in the field.

5.3 Wave Dissipation Model

Once a wave starts to break, the wave height will decrease until it reaches some stable wave steepness limit. If the dissipation rate of the wave height is known somehow starting from the breaker point, the depth profile can be obtained from the measured phase speed. The Wave Dissipation Model aims to estimate wave heights and water depths starting from the breaker point adopting a wave transformation (dissipation) model for the wave breaking zone and the nonlinear shallow water theory-based wave phase speed. Fig. 45 presents a schematic of the wave dissipation model along with inputs and outputs.

The two component equations in the Wave Dissipation Model have two unknowns:

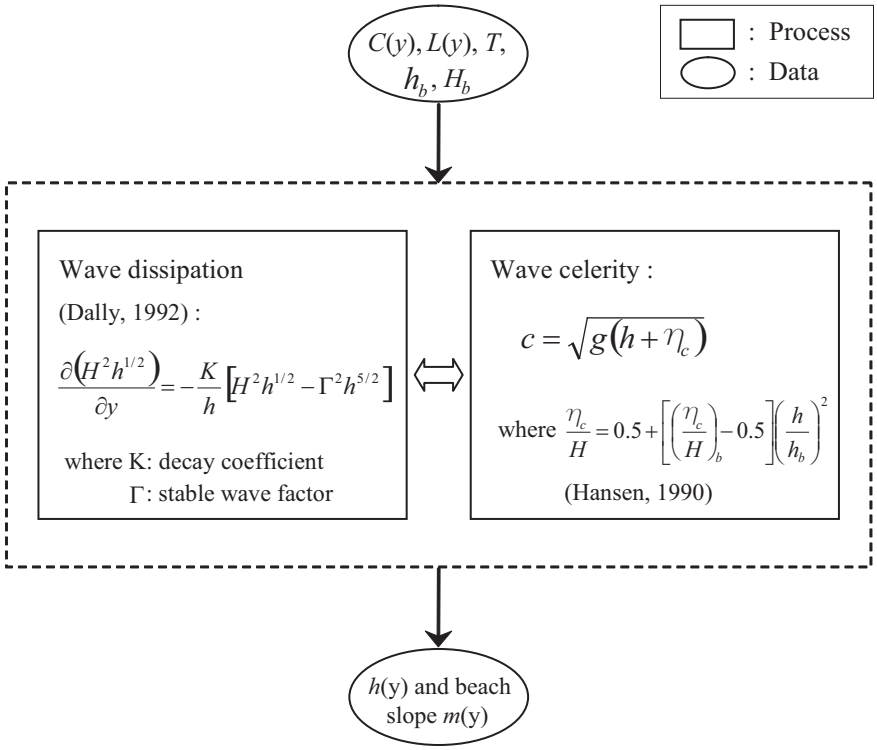

Figure 45: Components of the Wave Dissipation Model along with inputs and outputs.

$H(y)$ (or wave crest elevation $\eta_c(y)$) and $h(y)$. The wave celerity profile $c(y)$ is provided from the wave image sequence. Hence, the two unknowns of H and h are determined by combining the two equations. The ratio of η_c to H after wave breaking can be determined using an experimentally determined relation.

5.3.1 Wave dissipation modeling by wave-by-wave approach

After wave breaking, wave energy dissipation is mainly caused by the turbulent velocity fluctuations resulting from wave breaking. The energy dissipation due to bottom friction in the breaking zone is negligible compared to the turbulent dissipation. Dissipated wave height can be computed from the energy flux conservation law (Kamphuis, 1994):

$$\frac{\partial\left(Ec_g cos\theta\right)}{\partial y} = -D \tag{46}$$

where E is the wave energy per unit surface area, c_g is the group velocity, θ is incident wave angle, and D is the energy dissipation rate per unit surface area.

For quantifying wave decay of breaking random waves in the breaking zone, two main approaches have been proposed: turbulent bore energy dissipation-based probabilistic approach and stable energy approach (Kamphuis, 1994). The first approach computes the energy dissipation rate by introducing the bore dissipation concept from the hydraulic jump and associating the bore dissipation term with the statistical wave height distribution approximated by a truncated Rayleigh distribution (Battjes and Janssen, 1978; Thornton and Guza, 1983; Battjes and Stive, 1985). The wave height in the wave energy term is represented by the root mean square wave height (H_{rms}). This approach is not successful at explaining that the wave height stabilizes at some point after initiation of wave breaking, in particular, in barred beaches.

The second approach was developed by Dally et al. (1985), based on observation of the wave height stabilizing after wave breaking on a horizontal bed (Horikawa and Kuo, 1966). Dally et al. (1985) assumed that the energy dissipation rate per unit surface area is proportional to the difference between the local energy flux and the stable energy flux, resulting in:

$$\frac{\partial\left(Ec_g\right)}{\partial y} = -\frac{K}{h}\left[Ec_g - \left(Ec_g\right)_s\right] \tag{47}$$

where K is a dimensionless decay coefficient, h is the water depth, and the subscript s indicates the stable energy flux. Assuming a stable wave height given by $H_s = \Gamma h$ where Γ is a dimensionless stable wave factor, Eq. 47 is rewritten as:

$$\frac{\partial\left(H^2 h^{1/2}\right)}{\partial y} = -\frac{K}{h}\left[H^2 h^{1/2} - \Gamma^2 h^{5/2}\right] \tag{48}$$

Horikawa and Kuo (1966) showed experimentally that the waves breaking on a beach approach the stable wave height with the stable wave factor Γ in the range of $0.35 \sim 0.40$. Dally et el. (1985) determined best fit values for K and G for regular waves from small scale laboratory data, and found that fixed values of $K = 0.15$ and $G = 0.40$ represent robustly all the data from different beach slopes. Dally (1992) applied Eq 48 to random breaking waves in the nearshore field with the same fixed values of K and G by a wave-by-wave approach, and verified that the model derived wave height statistics show favorable comparison to the field measurements.

In the present study, the wave dissipation algorithm of Dally (1992) is adopted to compute wave dissipation rate, thereafter estimating dissipated wave heights and water depths in the breaking zone by association with the wave phase speed equation. In addition, the fixed values of $K = 0.15$ and $G = 0.40$ is used as verified by Dally (1992) for random breaking waves in fields. The wave dissipation algorithm is applied by the finite forward-stepping method:

$$\frac{\partial \left(H^2 h^{1/2}\right)}{\partial y} = \frac{\left(H^2 h^{1/2}\right)_{i+1} - \left(H^2 h^{1/2}\right)_i}{\Delta y} = -\left(\frac{K}{h}\left[H^2 h^{1/2} - \Gamma^2 h^{5/2}\right]\right)_{i+1} \tag{49}$$

where location i is given in the offshore side starting from the breaker point, and location $i + 1$ in the onshore side.

5.3.2 Ratio of crest elevation to wave height after wave breaking

At the initiation of wave breaking, the ratio of η_c/H has been observed to be up to 0.85 in laboratory experiments of periodic waves in the surf zone (Hansen, 1990). However, the ratio of η_c/H after wave breaking tends to approach the symmetric wave shape value of 0.5. The relation between η_c and H in shallow water can be derived using cnoidal wave theory. However, the theoretical cnoidal relation over-predicts the ratio of η_c/H in the breaking zone, compared to the experimental data

of Hansen (1990). Based on the cnoidal relation, Hansen (1990) proposed a parabolic variation relation and calibrated against laboratory data on various beach slopes for the relation η_c and H after wave breaking:

$$\frac{\eta_c}{H} = 0.5 + \left[\left(\frac{\eta_c}{H}\right)_b - 0.5\right]\left(\frac{h}{h_b}\right)^2 \tag{50}$$

The above equation approaches 0.5 as the depth decreases to 0. At the break point, this equation reverts to Eq. 45. In this study, Eq. 50 is used to compute the relation of the crest elevation and the wave height after wave breaking. In addition, the ratio of η_c/H is likely to vary in the range of $0.5 \sim 1.0$ in the wave breaking zone. So, the ratio is assumed to remain in that range during wave dissipation after wave breaking.

5.4 Wave Shoaling Model

The Wave Shoaling Model is used to derive water depths and wave heights in shallow water just before wave breaking. The Wave Shoaling Model algorithm is backward-schemed to compute the wave height and depth starting from the breaker point toward the offshore.

Up to the onset of wave breaking in shallow water, waves shoal and increase in wave height. If the coast is long and straight, the bottom contours may be also straight and parallel. In this special case, the change in wave height is found using the energy flux conservation law with the shallow water approximation:

$$H_2 = H_1\left(\frac{h_1}{h_2}\right)^{1/4}\left(\frac{cos\theta_1}{cos\theta_2}\right)^{1/2} \tag{51}$$

where subscripts 1 and 2 denote two different locations in the cross-shore direction. If the waves approach perpendicular to the coastline, Eq. 51 approximates to Green′s law:

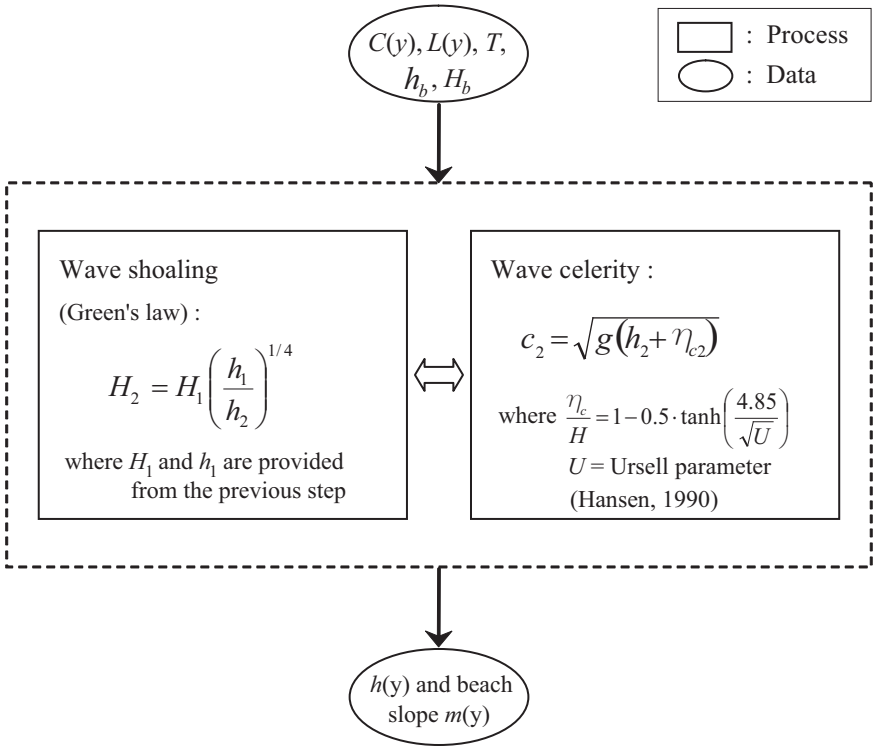

Figure 46: Components of the Wave Shoaling Model along with inputs and outputs.

$$H_2 = H_1 \left(\frac{h_1}{h_2}\right)^{1/4} \tag{52}$$

Eqs. 51 and 52 in the Wave Shoaling Model have two unknowns H_2 and h_2, since H_1 and h_1 are determined at the previous step or initially specified in the Wave Breaker Model at the wave breaking point. Hence, if the nonlinear shallow water theory-based wave phase speed is provided, the two unknowns become determinant by associating the wave shoaling equation with the wave celerity equation as shown in Fig. 46.

Myrtle Beach, where the 2003 datasets were collected, has partially straight coast line and parallel bottom contours over several kilometers alongshore. In addition, waves were incoming almost perpendicular to the coast in the surf zone. For those reasons, the Green′s law (Eq. 52) is primarily adopted to compute the two unknowns H and h. In Case 2 of the four datasets, having relatively large incident wave angles, Eq. 51 is alternatively used when the wave angle effects on the depth inversion should

be considered.

The ratio of η_c to H at the breaker point is determined using Eq. 45. The ratio η_c/H for shoaling waves before wave breaking is assumed to be larger than 0.5 and less than the value given by Eq. 45, since waves are still in shallow water having the higher and steeper crests and the shallower and longer troughs. The ratio η_c/H for shoaled waves in shallow water can be approximated from the first-order cnoidal wave theory, having accuracy within $\pm$ 5% for $U < 3000$ (Hansen, 1990):

$$\frac{\eta_c}{H} = 1 - 0.5 \cdot tanh\left(\frac{4.85}{\sqrt{U}}\right) \tag{53}$$

where U is the Ursell parameter defined as $U = HL^2/h^3$. In a typical sea state condition in shallow water with $H \sim 1\ m$ and $L \sim 50\ m$ at water depth of $h \sim 3\ m$, the Ursell parameter becomes 93 which is much less than the upper bound 3000. This preliminary test for the Ursell parameter indicates that the approximated above equation can be applied for shoaling waves in shallow water. So, Eq. 53 is used to determine the relation η_c/H in the Wave Shoaling Model in this study.

The ratio η_c/H in the Wave Shoaling Model has a discontinuity at the breaker point where the transition between Eqs. 45 and 53 occurs. Eq. 45 was adjusted to the experimental data after derivation while Eq. 53 remains theoretically derived. In order to connect the two equations at the breaker point smoothly, the relation η_c/H over the distance $y_b < y < y_b + 0.5L_b$ along the cross-shore is linearly interpolated as follows:

$$\left(\frac{\eta_c}{H}\right)_y = \left(\frac{\eta_c}{H}\right)_b - \frac{\left[(\eta_c/H)_b - (\eta_c/H)_{y_b+0.5L_b}\right]}{y_b + 0.5L_b}(y - y_b)\ , \quad for\ \ y_b < y < y_b + 0.5L_b \tag{54}$$

where the subscripts y, b, and $y_b + 0.5L_b$ indicate locations of shoaled wave crests. As mentioned in Chapter IV regarding wave celerity transition near the breaker point, the celerity transition was assumed to occur over the distance of approximately $y_b -$

$0.5L_b < y < y_b + 0.5L_b$ in Chapter IV, based on previous observations. For this reason, the distance $y_b < y < y_b + 0.5L_b$ in Eq. 54 is used.

At the break point and in the region $y \geq y_b + 0.5L_b$, Eqs. 45 and 53 are used respectively. In addition, the ratio η_c/H is assumed to remain in the range of 0.5 $\sim$ 1.0 during wave shoaling before wave breaking. In shallow water, wave breaking may occur at the maximum ratio of H/h at the breaker point. In the region of wave shoaling before wave breaking, the ratio H/h will be less than H_b/h_b. Hence, the ratio H/h is bounded to remain less than its maximum ratio at the breaker point in this study.

5.5 Beach profile iteration

The Ursell parameter at breaking, U_B, in Eqs. 45 and 50 is dependent of local beach slope. However, the beach slope is not known before executing the depth inversion algorithm. In addition, the ratio η_c/H at $y = y_b + 0.5L_b$ in Eq. 54 cannot be determined before implementing the nonlinear depth inversion algorithm, since the Ursell parameter at that location is not known yet. For these reasons, either an initial guess for beach slope or an initial value of the ratio η_c/H at the breaker point and the location $y = y_b + 0.5L_b$ needs to be chosen. The initial value of the ratio η_c/H at the breaker point in the Wave Breaker Model is set to be 0.75, since this parameter ranges from 0.7 to 0.8 (Hansen, 1990). As for the initial value of the ratio η_c/H used in the Wave Shoaling Model, the same default value 0.75 is used instead of Eq. 53 during the first run.

The initial beach profile estimated through the first iteration results in estimated depths and slopes, enabling the beach profile to be recalculated via the second iteration. The beach profile is updated until a certain residual limit. In this study, the residual R is defined as:

$$R^k = \frac{\sqrt{\sum_{i=1}^{N} \left(h_i^k - h_i^{k-1}\right)^2}}{N} \tag{55}$$

where k indicates k^{th} iteration, and i is location along the beach profile, with N total points. Computation stop once the residual is reduced to 10^{-2} m.

5.6 Results and discussion

Nearshore bathymetry in the wave breaking zone was inverted for each of the four datasets using the nonlinear depth inversion algorithm by involving the three model components: the Wave Breaker Model, the Wave Dissipation Model, and Wave Shoaling Model. The Wave Breaker Model was used to predict the wave height H_b and depth h_b at the break point by utilizing each celerity profile with its sole wave properties of the wavelength and wave period. The Wave Dissipation Model computed the dissipated wave height and water depth starting from the breaker point in the shoreward direction. The Wave Shoaling Model derived the shoaled wave height and water depth in the offshore direction starting from the breaker point. The beach profiles were iteratively estimated up to the residual limit by re-using the beach and beach slope profiles newly updated from the three model components of the nonlinear depth inversion algorithm.

5.6.1 Bathymetry derived by nonlinear depth inversion

In the depth inversion procedure, individual wave celerity profiles belonging to only two groups of the intermediate and outer breaking groups were considered, since each of them has its own breaker point identified from the raw image cross-shore timestacks. Table 9 presents a number of wave celerity profiles obtained from each video image dataset with a 34.2 minute time-span. The numbers N_v of video-imaging derived wave

Table 9: Numbers of wave celerity profiles used for nonlinear depth inversion.

Case No.	Breaking group	N_w	N_v^g	N_v	N_v / N_w
I	interm.	302	51	116	0.38
	outer		65		
II	interm.	415	117	191	0.46
	outer		74		
III	interm.	259	55	91	0.35
	outer		36		
IV	interm.	253	80	131	0.52
	outer		51		
Notes		N_w : number of waves in record. N_v : total number of the wave celerity profiles. N_v^g : number of the celerity profiles in each group.			

celerity profiles used to invert the beach profile in each dataset are approximately 0.43 times the number N_w of waves in the in-situ record, i.e. $N_{1/3} < N_v < N_{1/2}$. Since waves with higher wave heights are more likely to be captured in the video image sequence, it is regarded that the nonlinear depth inversion in this study was implemented utilizing the wave celerity profiles having higher wave amplitudes. Significant wave height H_s (or $H_{1/3}$) is a widely used wave height parameter and the corresponding number of waves is close to N_v. Hence, H_s obtained from the in-situ measured pressure data is compared to the video-imaging derived wave heights.

5.6.1.1 Predicted wave height and water depth

Through the nonlinear depth inversion algorithm composed of the 3 component models, each celerity profile with its corresponding wave properties (wavelength and wave period) in each of the four datasets resulted in a predicted beach (water depth) profile

and a predicted wave height profile at the fist iteration. Those individual beach and wave height profiles predicted by the nonlinear depth inversion in each of the four datasets were locally averaged. The locally averaged beach profile was used again to iterate the next depth inversion computation and update the beach profile. If the residual R between the two newly updated beach profiles satisfied the residual limit, computations ceased. Figs. 47 and 48 show the breaker points, the nearshore beach and wave height profiles predicted by the nonlinear depth inversion, and their comparisons with the in-situ measured wave heights and bathymetry.

The predicted depths $h_p(y)$ for each of the four datasets were compared to the measured depths $h(y)$. The depth comparisons were conducted only for the measured depth range of $h > 0.1\ m$. The run-up and swash zone was not considered, since the depth inversion in the swash zone requires totally different theoretical approaches and is beyond the research scope in this study. The predicted wave heights (were compared primarily to the significant wave heights H_s (or $H_{1/3}$) obtained from the in-situ measured pressure head data. Additionally, the ranges of wave heights computed from the measured pressure head data were presented in terms of $H_{rms} \sim H_{max}$ for comparisons with the predicted wave heights at the instrument locations.

In general, good agreement trends between the predictions of the wave height and the water depth by the nonlinear depth inversion and the in-situ observations are found from Figs. 47 and 48. The nonlinear depth inversion derived beach profiles are well fitted to the measured bathymetry, compared to the beach profiles obtained by the linear depth inversion. The linear depth inversion generated a depth profile using a celerity profile by the linear dispersion relation approximated in shallow water. The linearly inverted depth profiles were systematically over-estimated, having deeper depths than the measured over the entire surf zone, due to neglect of the amplitude dispersion effect in the dispersion relation. In contrast, the present nonlinear depth inversion estimated contribution of the nonlinear amplitude effect to the wave celerity

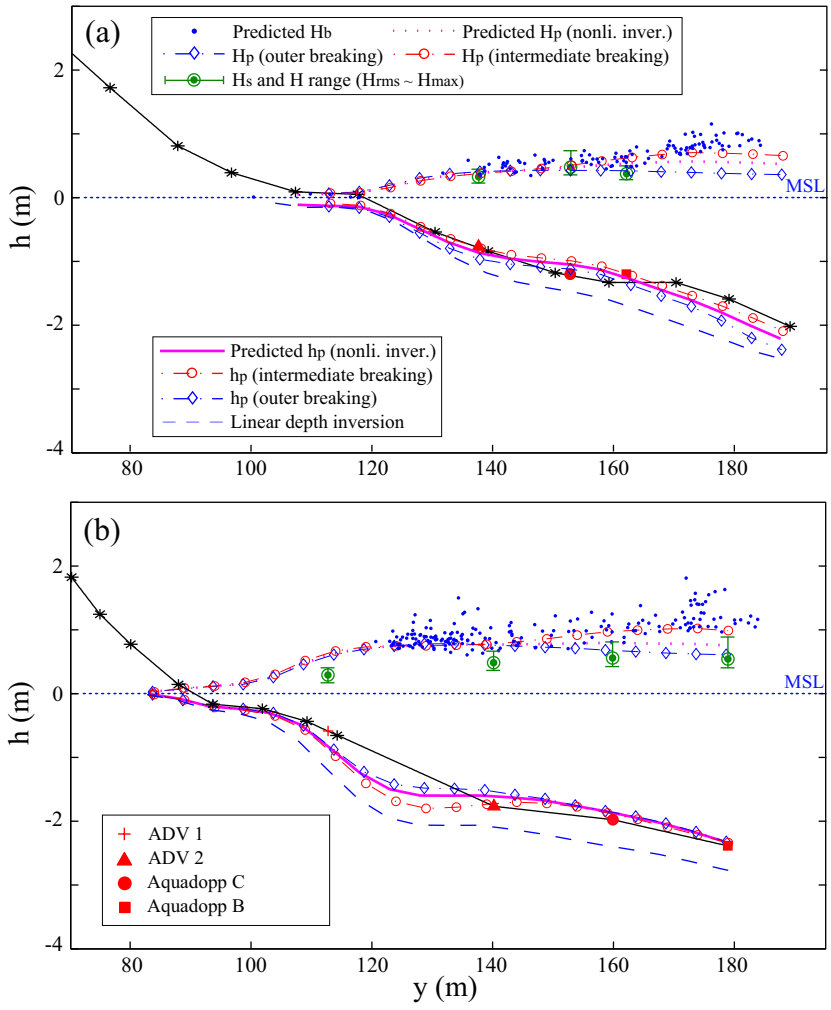

Figure 47: The breaker heights, the wave height and beach profiles predicted using the nonlinear depth inversion algorithm, and their comparisons with the in-situ measured wave heights and bathymetries in Cases 1 and 2: (a) Case 1, (b) Case 2.

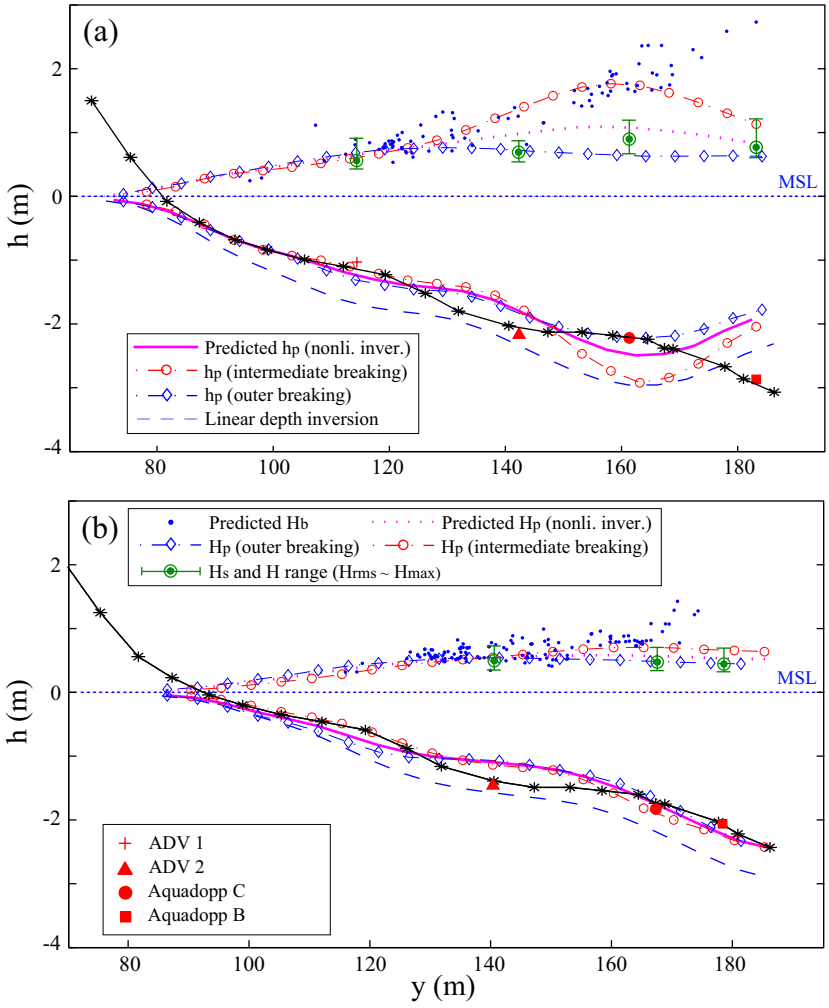

Figure 48: The breaker heights, the wave height and beach profiles predicted using the nonlinear depth inversion algorithm, and their comparisons with the in-situ measured wave heights and bathymetries in Cases 3 and 4: (a) Case 3, (b) Case 4.

dispersion and removed over-biased depth estimates. The predicted beach profiles by the nonlinear depth inversion match the measured beach profiles as shown in Figs. 47 and 48.

As for the predicted wave heights H_p using the nonlinear depth inversion algorithm, results for each of the four datasets are in the range of the wave heights of $H_{rms} \sim H_{max}$ obtained from the measured pressure head data, even though the predicted H_p were slightly over-estimated compared to the H_s. The predicted breaker heights H_b are found to be at the level of H_{max} obtained from the pressure head data, since breaking waves is likely to have highest heights. The predicted H_b also has a tendency to be slightly over-estimated, compared to the H_{max}. In particular, big differences between the predicted H_b and the H_{max} obtained from the pressure data are commonly found in the seaward steep-sloped beach areas, i.e. the seaward faces of bottom sand bars. Those big differences may be caused by the celerity transition even larger than 1.2 times the approximated nonlinear shallow water wave equation-based celerity.

The quantified comparisons of the predictions and the measurements were conducted in terms of normalized absolute errors:

$$\varepsilon_h(y) = \frac{|h_p(y) - h(y)|}{h(y)} \tag{56}$$

$$\varepsilon_H(y) = \frac{|H_p(y) - H_s(y)|}{H_s(y)} \tag{57}$$

and actual biased errors:

$$\Delta h(y) = h_p(y) - h(y) \tag{58}$$

$$\Delta H(y) = H_p(y) - H_s(y) \tag{59}$$

The mean $\varepsilon_h(y)$, $\varepsilon_H(y)$, $\Delta h(y)$ and $\Delta H(y)$ were computed over the entire profiles for depth errors or the instrument locations for wave height errors for each of the four

datasets as ε_h, ε_H, Δh and ΔH respectively. In addition, the standard deviations for those errors were calculated as ε_h^{std}, ε_H^{std}, Δh^{std} and ΔH^{std}.

Tables 10 and 11 summarize those error statistics for water depth and wave height comparisons, respectively. The depth estimates made by the nonlinear depth inversion show favorable agreements to the measured depths with an average of 14.8% normalized error, compared to normalized mean error of 38.4% for the linear approach. The linear depth inversion by Holland (2001) for shallow water (less than 4 m) predicted depths with normalized errors on the order of 20%. However, the normalized depth error concept may not be suitable to express the prediction accuracy for very shallow water depth (such as less than 1m), since smaller depth bias denominators of the error calculation fraction can cause fatally big errors. For this reason, the biased error indicating physical differences is more adequate to express the accuracy for depth inversions in shallow water as in this study with the depth range of $0.1 \sim 3$ m.

The average biased depth error by the nonlinear depth inversion is 0.06 m in the error range of $\pm$ 0.10m for the four datasets. Meanwhile, the linear depth inversion results in 0.28 m bias error, ranging from 0.33 to 0.48 m. The bias error of 0.06 m by the nonlinear inversion is almost the same order to the accuracy of the empirical nonlinear depth inversion formula by Holland (2001) having the bias error of 0.03 m for shallow water depth less than 4 m.

The predicted wave heights show good correspondence to the heights obtained from the pressured data within the wave height range of $H_{rms} \sim H_{max}$ as shown in Figs. 47 and 48. The overall bias error of the wave height estimates is about 0.14 m, and the average normalized wave height error is 31.3%. Those errors seem to be relatively larger compared to the depth estimate errors, approximately 2 times larger than the depth errors. However, the bias errors of the depth and wave height estimates are almost on the same order of 0.1 m, indicating that the nonlinear depth

Table 10: Statistical water depth comparison between predictions and measurements.

Case No.	I	II	III	IV
${}_{no}\varepsilon_h$ (%)	13.0	20.2	11.4	14.4
${}_{no}\varepsilon_h^{std}$ (%)	10.3	18.6	13.3	10.2
${}_{no}\Delta h$ (m)	0.05	0.07	-0.10	-0.03
${}_{no}\Delta h^{std}$ (m)	0.17	0.21	0.31	0.18
${}_{li}\varepsilon_h$ (%)	36.5	52.0	31.0	34.0
${}_{li}\varepsilon_h^{std}$ (%)	14.3	35.6	23.2	18.8
${}_{li}\Delta h$ (m)	0.38	0.48	0.33	0.33
${}_{li}\Delta h^{std}$ (m)	0.17	0.23	0.30	0.15
Notes	ε_h : normalized absolute depth error Δh : biased depth error std : standard deviation of the errors *no* : nonlinear depth inversion *li* : linear depth inversion			

Table 11: Statistical wave height comparison between predictions and measurements.

Case No.	I	II	III	IV
ε_H (%)	20.2	65.6	22.0	17.3
ε_H^{std} (%)	18.8	38.0	14.9	7.1
ΔH (m)	0.07	0.26	0.16	0.08
ΔH^{std}(m)	0.08	0.05	0.11	0.03
Notes	ε_H : normalized absolute wave height error ε_H^{std} : standard deviation of the normalized absolute wave height error ΔH : biased wave height error ΔH^{std}: standard deviation of the biased wave height error			

inversion predicted water depths and wave heights with the same accuracy. As a matter of fact, the depth errors were averaged over the entire beach profiles while the mean wave height errors were computed only at the instrument locations. In addition, the instruments were located in the area of dense wave breaking points where over-predictions of water depth and wave height are commonly observed. If the wave height data could be collected more densely and used to compare to the estimates, the wave height errors might be more reduced.

From Figs. 47 and 48, it is seen that the highly over-biased errors of both the depth and wave height estimates tend to appear in the locations of dense wave breaking. Relatively bigger estimate errors and standard deviations of the errors are observed in Cases 2 and 3 rather than Cases 1 and 4, as presented in Figs. 47 and 48, and Tables 10 and 11. Since the weather in Cases 2 and 3 was dark cloudy and rainy as mentioned in Chapter III (Tables 1 and 2), sea states were likely to have higher and steeper waves causing remarkable nonlinear amplitude effects and wave shape transitions across the

breaker points. In those two Cases with stormy sea states, over-estimations of water depths and wave heights in the vicinity of the dense breaker points at y = 120m in Case 2 and y = 160m in Case 3 are much larger than the other two cases. This is due to the celerity transition across the breaker point. Previously in Chapter IV, the wave celerity transition was adjusted to the level of the nonlinear shallow water wave equation-based celerity by dividing by the empirical factor 1.2 (Eq. 26). However, this factor is still under-estimated to adjust the wave celerity transition across the breaker points with higher and steeper waves generated in stormy days. Hence, in order to improve depth and wave predictions, well defined wave celerity transition observations on various sea states and beach systems are required.

The under-estimated depths are found in the bottom trough location in each of the four datasets where wave breaking rarely occurred. Those under-predictions were probably caused by fully un-recovered wave celerity after passing over the bottom crest positions. In the neighborhood of the bottom crests, incoming waves start to break and slow down. After passing over the bottom crests, breaking waves may not fully speed up to catch up with the depth dependency of the wave celerity while propagating over the bottom troughs deepened again.

An interesting depth under-prediction in the area of offshore boundary is found in Case 3 as shown in Fig. 48(a). The day in Case 3 was rainy and stormy having the biggest waves (H_s = 0.78 m) with narrow banded spectrum. About one third of the incoming waves were breaking in the seaward face of the bottom sand bar, having significant wave shoaling in that area. This depth under-prediction could be primarily caused by wave reflection. Incoming waves in this dataset case showed shore-normal incidence (Fig. 40(c)). Wave breaking with higher wave heights was occurring at the location of the bottom sand bar having the steep sloped seaward face. This wave breaking at the bottom crest location could cause some portion of breaking waves to be reflected and propagate toward the offshore, resulting in seeming

decrease of the incoming wave propagation speeds in the video image sequence. Other than the wave reflection, cross-shore surface currents and offshore disconnection of video-based celerity estimation could be possible causes. The instrument Aquadopp B had a faulty beam to collect 3 flow velocity components. Hence, the wave reflection and the cross-shore surface current issues cannot be discussed further by quantitative analysis approaches.

5.6.1.2 Variation of η_c/H and H_b/h_b through the surf zone

The Wave Breaker Model adopted the modified Miche breaker formula (Eq. 44) to predict wave heights and water depths at the breaker points and represent both depth-induced and steepness-caused wave breaking over the wide surf zone. Relations of the wave crest elevation and the wave height were determined through the three model components (Wave Breaker Model, Wave Dissipation Model, and Wave Shoaling Model) of the nonlinear depth inversion model to better predict wave crest elevation in the surf zone. While a beach profile and a wave height profile were produced along the cross-shore transect from each celerity profile through the nonlinear depth inversion, a profile of the ratio η_c/H was also implicitly computed and generated simultaneously. The ratio η_c/H profiles implicitly predicted by the nonlinear depth inversion for each of the four datasets were locally averaged. Figs. 49 through 52 present variation of the ratios H_b/h_b and η_c/H over the bottom profiles through the surf zone for each of the four datasets.

The starting position to predict water depth and wave height using each celerity profile was the breaker point. Due to the beach slope dependency of the ratio η_c/H at the breaker point, the ratio η_b/H_b at the first iteration of the nonlinear depth inversion algorithm was set to be 0.75 as an initial guess. For the second iteration, the ratio η_b/H_b was updated using the beach profile evaluated at the previous step

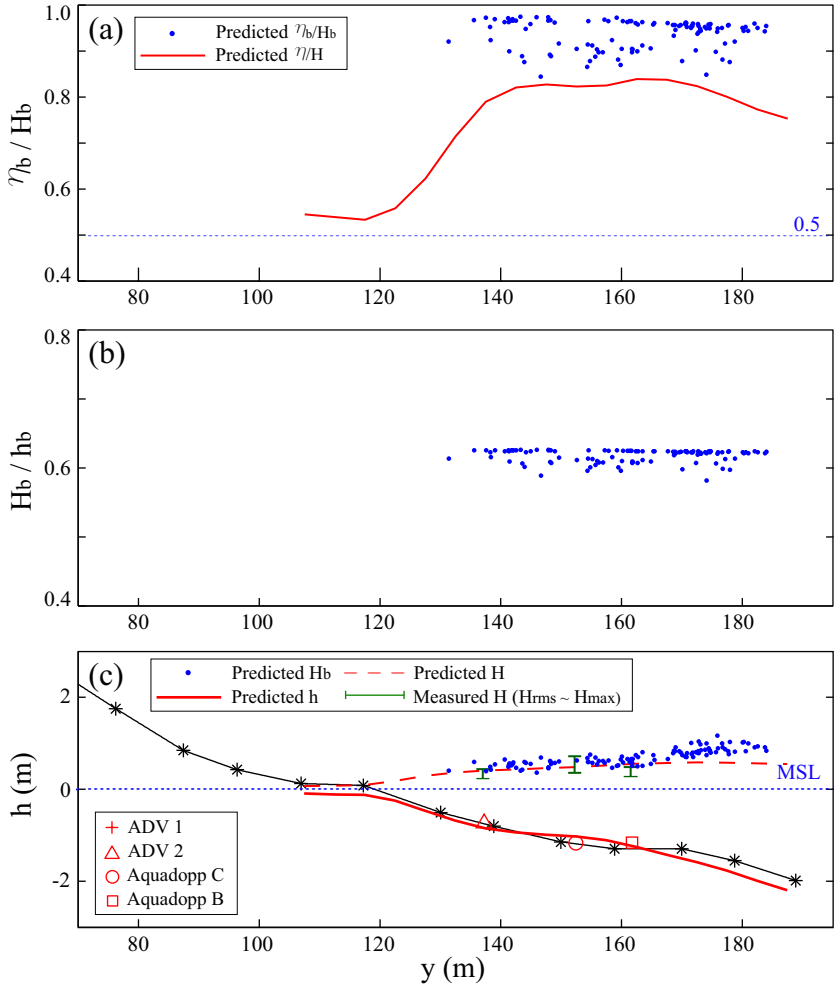

Figure 49: Variation of the ratios H_b/h_b and η_c/H over the bottom profiles for Case 1: (a) Predicted η_b/H_b and averaged η_c/H profile through the surf zone, (b) Predicted H_b/h_b, (c) Beach profile and predictions of breaker heights, wave height and beach profiles.

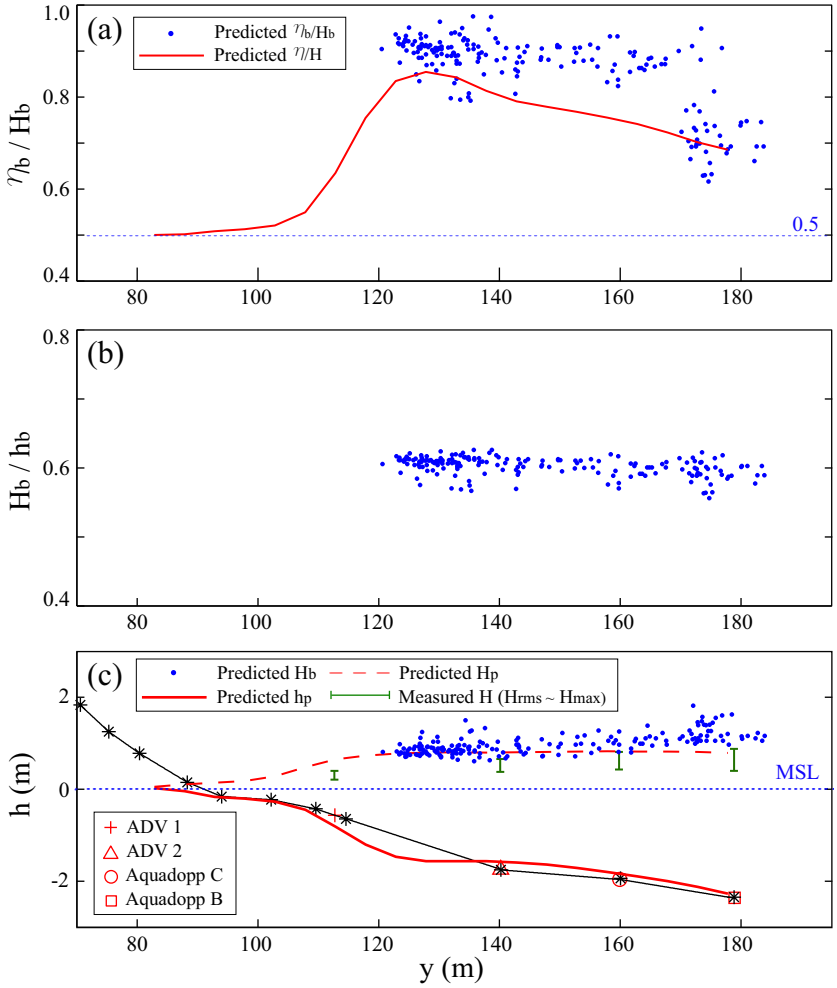

Figure 50: Variation of the ratios H_b/h_b and η_c/H over the bottom profiles for Case 2: (a) Predicted η_b/H_b and averaged η_c/H profile through the surf zone, (b) Predicted H_b/h_b, (c) Beach profile and predictions of breaker heights, wave height and beach profiles.

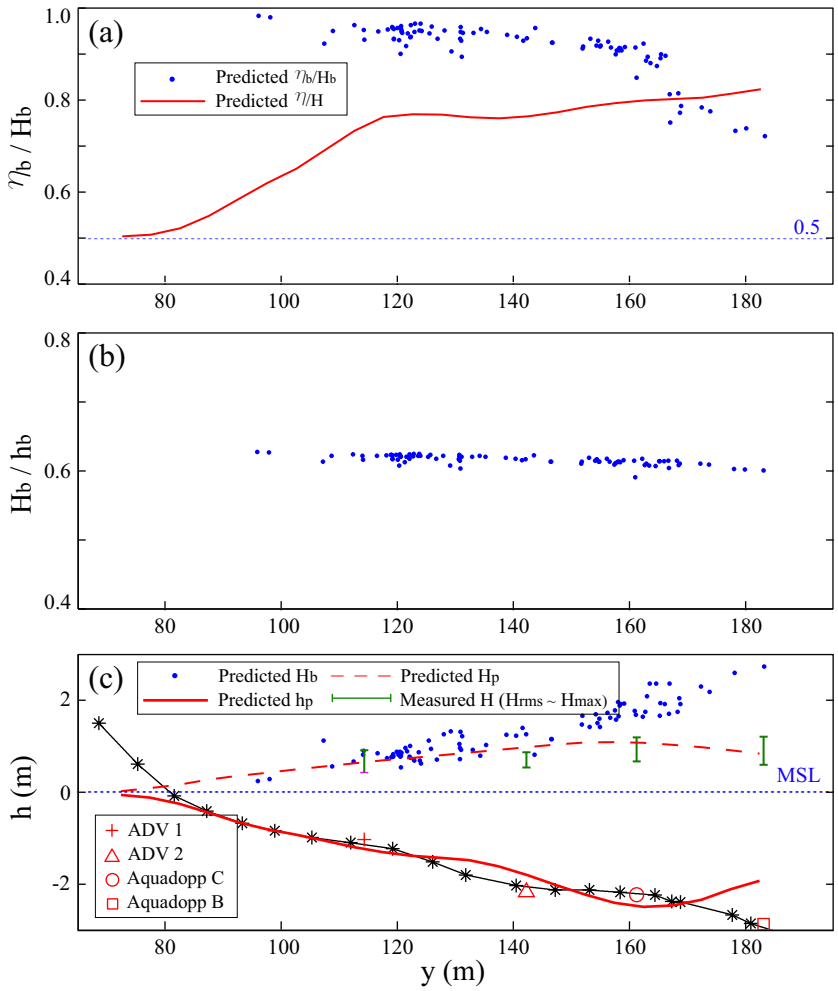

Figure 51: Variation of the ratios H_b/h_b and η_c/H over the bottom profiles for Case 3: (a) Predicted η_b/H_b and averaged η_c/H profile through the surf zone, (b) Predicted H_b/h_b, (c) Beach profile and predictions of breaker heights, wave height and beach profiles.

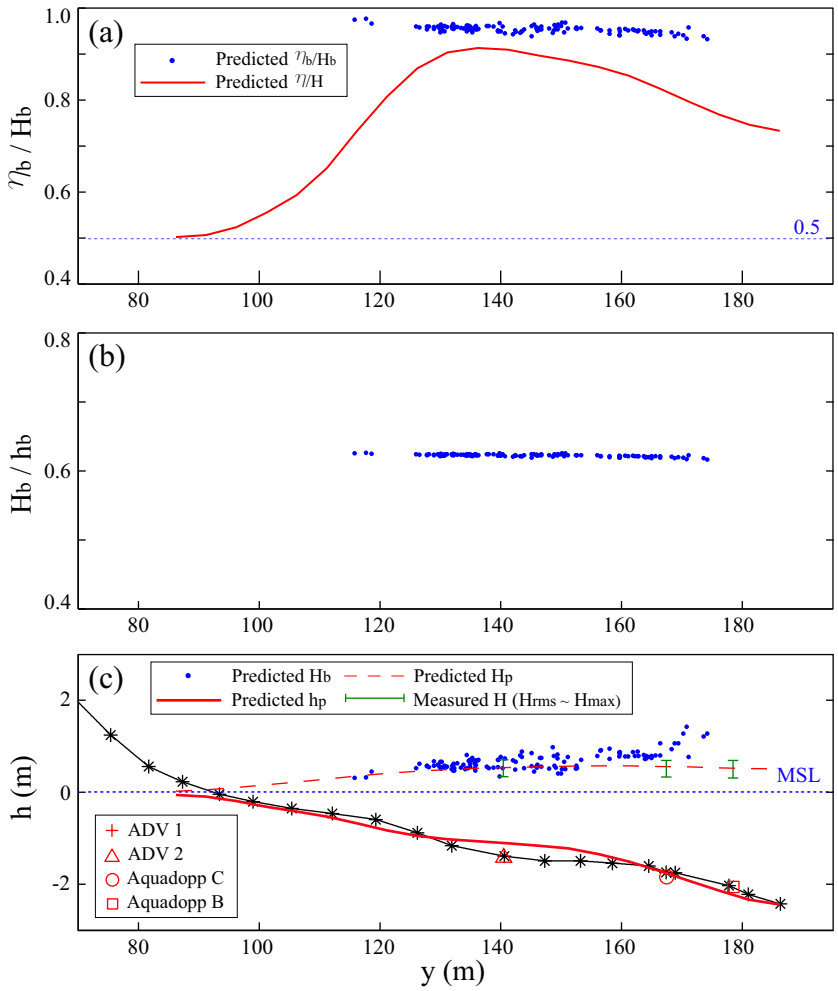

Figure 52: Variation of the ratios H_b/h_b and η_c/H over the bottom profiles for Case 4: (a) Predicted η_b/H_b and averaged η_c/H profile through the surf zone, (b) Predicted H_b/h_b, (c) Beach profile and predictions of breaker heights, wave height and beach profiles.

and the ratio η_c/H was re-computed starting from the breaker point through the surf zone.

The final η_c/H profiles of the four datasets are shown in Figs. 49 through 52 through the wave breaking zone. At the offshore boundary, the ratios are approaching 0.7 except for Case 3 in which a third of the incoming waves were onset of wave breaking at the offshore boundary. This value of 0.7 at the surf zone line is found to be within the range observed for shallow water waves (Svendsen et al., 1978). The 4 η_c/H profiles have high peaks in the area of dense breaker points, i.e. the seaward boundary of the inner surf zone, in general. In the inner surf zone, the profiles are approaching the value for a symmetrical profile (0.5), showing the parabolic variation form which is consistent with the observations of Hansen (1990). The slope at Myrtle Beach used in this study is in the range of $1/40 \sim 1/20$. From the observations of Hansen (1990) for those beach slopes, it is seen that the relation of η_c/H fitted to the experimental data varied down from about 0.9 to 0.5 between the breaker point to the shoreline forming a parabolic pattern.

As for the individual η_c/H ratios at the breaker points in each dataset, they are comparable to the observations of Hansen (1990), even though slightly over-predicted. The values of the ratio η_b/H_b obtained from the measurements by Hansen (1990) were in the range of approximately $0.75 \sim 0.85$, while the prediction of Hansen (1990) using the relation of η_b/H_b (Eq. 45) exceeded 0.9 up to 0.95. Similarly, the prediction of the ratio η_b/H_b made in the present nonlinear depth inversion ranged roughly from 0.7 to 0.95. In Cases 1 and 4, the ratio η_b/H_b at some of the breaker points was found to exceed even 0.95.

The predicted values of the ratio H_b/h_b were approximately in the range of 0.55 $\sim$ 0.65. This prediction range made in the random wave field is compatible with the suggestions (Eqs. 37 and 38) of Kamphuis (1991) and the field observations (Eq. 42) of Thornton and Guza (1983) such that the H_b/h_b ratio is about 0.6 overall. The

predicted H_b/h_b values have increasing patterns with decrease of water depths from the outer surf zone lines to the inner surf zone boundaries for the four datasets. This indicates that wave breaking in the outer surf zone became more steepness-dependent than in the nearby inner surf zone.

5.6.2 Effect of incident wave angle on the depth inversion

Incoming waves in the surf zone along a straight coast approach the shoreline at an angle undergo refraction. Wave crests in the four datasets are getting nearly parallel, as they approach to the shoreline in the surf zone as shown in Fig. 22. For this reason, the nearshore depth inversions were conducted by using only the cross-shore transect component (c_y) of the wave celerity vector $c = (c_x, c_y)$ where $c_x \sim 0\ m/s$, resulting in favorable agreements between the predictions and the measurements.

Among those good agreements shown in each of the four datasets, in particular, the nonlinear depth inversion for Case 2 produced a slightly under-predicted depth profile over the entire outer surf zone differently from the others. The under-biased depth prediction was primarily caused by the effect of the wave angle. From Fig. 22, it is seen that incoming waves in Case 2 had relatively larger wave angles in the surf zone compared to the other 3 cases. In addition, the incident wave angles continued to consistently deviate from the shore-normal direction (0°) over the surf zone as shown in Fig. 53(a).

In order to include the effect of the wave angle in the depth inversion, each individual celerity profile $c_y(y)$ was divided by $cos[\theta(y)]$, where θ is wave angle estimates from the video image sequence, to obtain its absolute magnitude celerity profile $c(y)$. Thereafter, those individual absolute magnitude celerity profiles were input to the present nonlinear depth inversion algorithm. In the Wave Shoaling Model, wave shoaling before wave breaking was modeled using the energy flux conservation law

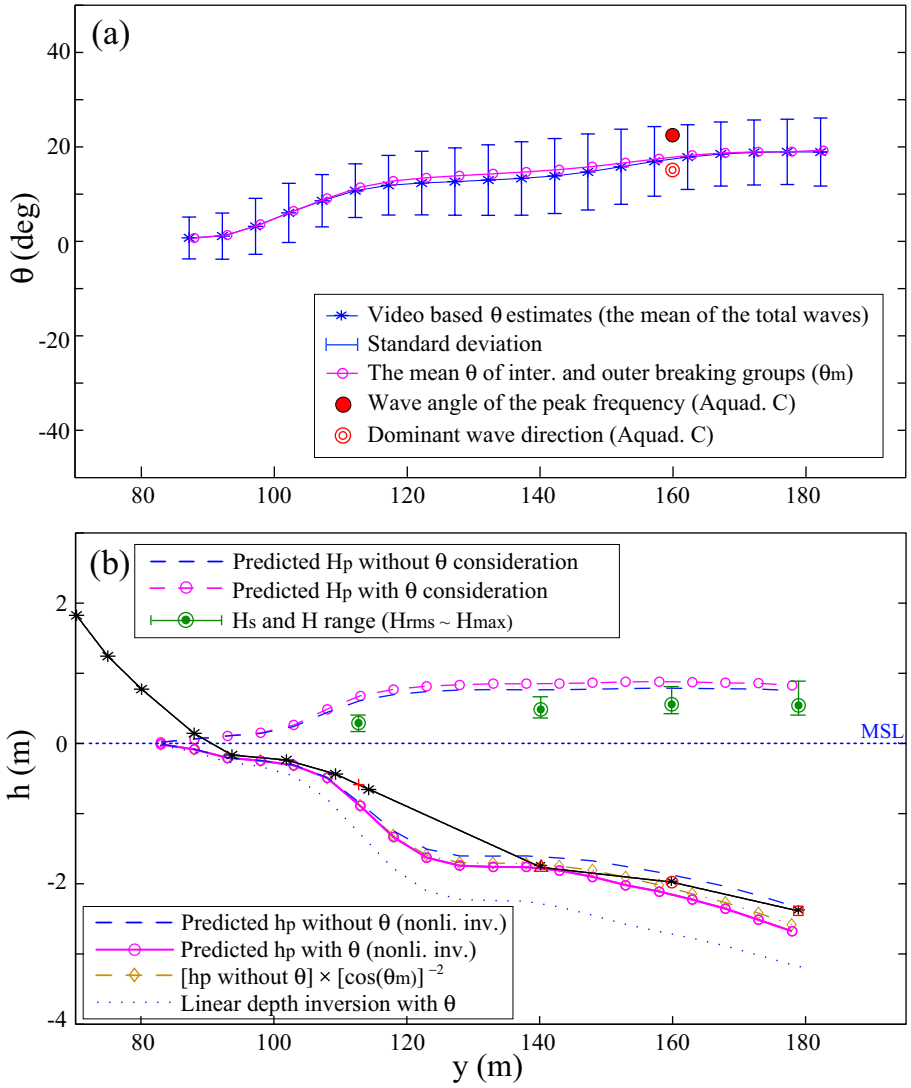

Figure 53: Effects of incident wave angle on the depth inversion in Case 2: (a) variation of incident wave angle estimated from video image sequence, (b) incident wave angle effects on predictions of wave height and depth.

with the shallow water approximation (Eq. 51), instead of Green′s law due to the wave refraction.

With the inclusion of the incident wave angles in the nonlinear depth inversion, the depth estimates increased beyond the measured depths over the under-predicted area as shown in Fig. 53(b). The effect of the incident wave angle on the depth prediction can be quantified using the nonlinear shallow water wave equation-based wave celerity equation, i.e. $c = \sqrt{g(h + \eta_c)}$. This equation can be re-arranged as a function of wave celerity: $h = c^2/g - \eta_c$. Since the absolute magnitude of celerity, $c(y)$, along the cross-shore transect can be expressed as $c(y) = c_y(y)/cos[\theta(y)]$, the re-arranged nonlinear shallow water wave equation-based dispersion relation becomes:

$$H_\theta = \frac{c_y^2/cos^2\theta}{g} - \eta_c \tag{60}$$

If θ is almost 0° in the surf zone, the above equation becomes $h_\circ = c_y^2/g - \eta_c$. By subtractiing the two equations, the little variation in θ or $cos\theta$ with the same c_y can be related to variation in h as

$$\delta h\,(= h_\theta - h_\circ) \sim h_\circ \cdot \left(\frac{1}{cos^2\theta} - 1\right) \tag{61}$$

where h_θ = predicted depth with the inclusion of wave angle, $h_\circ$ = predicted depth without the wave angle inclusion, and the δ denotes the variations. If the above equation is re-arranged again, it becomes:

$$h_\theta \sim \frac{h_\circ}{cos^2\theta} \tag{62}$$

In this perspective, when the depth profile predicted without the wave angle inclusion in the depth inversion was multiplied by the $1/cos^2\theta$ using the equation above, the product approximated the depth profile predicted with the consideration of incident wave angles. Thus, the depth difference when wave angles are included can be quantified approximately using Eq. 61.

5.7 Summary

Nearshore bathymetry in the wave breaking zone of each of the four datasets was inverted using the nonlinear depth inversion algorithm involving three model components: the Wave Breaker Model, the Wave Dissipation Model, and Wave Shoaling Model.

The Wave Breaker Model, composed of the modified Miche breaker formula and the approximated nonlinear shallow water wave equation-based celerity equation, was used to predict the wave height H_b and depth h_b at the breaker point by utilizing video derived wave properties. The Wave Dissipation Model, composed of the Dally wave dissipation formula and the approximate nonlinear shallow water wave equation-based celerity equation, was used to compute the wave height and water depth inshore of the break point. The Wave Shoaling Model, composed of Green′s law and the approximate nonlinear shallow water wave equation-based celerity equation, was used to derive the shoaled wave height and water depth in the seaward direction starting from the breaker point.

Good agreement between the predicted wave heights and water depths using the nonlinear depth inversion and the in-situ measurements were found in all four datasets for the depth range of 0.1 m to 3 m, in general. The nonlinear depth inversion-derived beach profiles were comparable to a measured with the biased mean depth error of +0.06m within ± 0.10m. In contrast, the linearly inverted depth profiles were systematically over-estimated over the entire surf zone, having an error of about 0.38m ranging from 0.33 to 0.48m, due to the neglect of the amplitude dispersion effect. The predicted wave heights using the nonlinear depth inversion algorithm were comparable to the significant wave heights H_s obtained from the measured pressure data with the biased wave mean height error of +0.14 m, ranging from 0.07 to 0.26

m. The predicted breaker heights were found to be at the level of the H_{max}, having a tendency to be slightly over-estimated, compared to the H_{max}.

Measurements of water surface elevation using planar remote sensing platforms are not available without stereo-optics, thereby the current remote sensing-based depth inversions are limited to utilizing the linear dispersion relation. However, the present Wave Breaker Model could retrieve the breaker heights and depths from nearshore mono-video imagery innovatively.

CHAPTER VI

ERROR SOURCE INVESTIGATIONS

6.1 Introduction

The newly developed video-based wave observation methodology enabled wave crest identification, wave property estimation and nonlinear depth inversion in the surf zone. Detailed procedures, results and individual discussions were presented in the previous three chapters. Herein, the results produced by the present video-based wave observation methodology will be analyzed and discussed through the error and accuracy investigations.

Error sources in the in-situ measured pressure and bathymetric data were mentioned during the brief description of the field data collection. Maximum error magnitude in the wave heights obtained from the four pressure datasets were possibly 0.003 m. Errors in the bathymetry measured by the Total Station system could be by up to 0.005 m in the vertical.

The results of the wave crest feature extraction, the wave property estimation and the nonlinear depth inversion may include errors caused by various error sources. The error sources can be categorized primarily into three groups: (1) accuracies in video image rectification, (2) adequacies of image processing parameters, and (3) accuracies in the chosen equations in the wave property estimation and the nonlinear depth inversion.

6.2 Errors in video image rectification

The wave image sequences captured in the 2-D image space domain are transformed into the real-world coordinates, involving camera distortion model calibration and image-to-world coordinate system transformation. Due to the fact that the coordinate transformation of image space to physical space is under-determined, some assumptions are introduced to the image rectification using the Direct Linear Transformation method such that image coordinates in the focal plane and the real world coordinates are collinear and camera lens distortion should be calibrated to be free prior to matching the image plane with the physical plane collinearly. In addition, the assumptions in the image transformation constrain the physical plane at a certain elevation (i.e. still water elevation), while waves propagate dissipating vertically in the surf zone. The assumptions made in the image rectification procedure can introduce some errors in physical analysis of wave crest movements. Hence, the physical errors caused by the image rectification needs to be quantified to validate the accuracy of the physical analysis for wave observations.

The physical error introduced by the camera distortion model calibration is primarily found in the distortion modeling equation in Eq. 12. Fig. 12 in Chapter III shows that the measurements of lens distortion used to model radial distortion deviate 0 to 2 pixels from the optimized two-coefficient odd-order polynomial for calibrating the radial distortion. This indicates that the odd-order polynomial does not account for all the non-linearities introduced by a camera lens, and therefore does not produce ideal, distortion-free video imagery. This potentially can cause significant errors in areas far from the video camera, while the transformation assumes that the camera is distortion-free.

Another possible image rectification error source is found in the collection of ground control points to calibrate the Direct Linear Transformation coefficients. All of the ground control points (GCP) to solve for the Direct Linear Transformation

coefficients are not evenly collected within the view of the entire image domain. Most of them are collected in dry beach areas as shown in Fig. 13. Close to the areas of the collected ground control points, precisely determined physical accuracy will be obtained. On the other hand, the physical accuracy may degrade with the increase of distance from the control point collection areas, i.e. toward the offshore. In addition, due to the oblique image capture by the video platform mounted on top of a high building in land, the physical resolution also will not be even in the rectified domain. The physical length resolution being higher in dry beach will decrease with the increase of distance toward offshore as shown in Figs. 54 and 55.

Figs. 54 and 55 present physical length scales of an image pixel after image rectification for Case 1 (oblique-top camera view) and Case 4 (oblique-side camera view) respectively. Commonly, the physical length scales of a pixel vertical length are much larger than the physical scales of the horizontal, in particular, as going out toward the offshore. Additionally, the physical length scales increase toward the offshore direction, having lesser physical length resolutions. Along the cross-shore transects for collecting image timestacks, the physical length scale of a pixel horizontal length is in the range of approximately $0.1 \sim 0.3$ m for both cases. In contrast, the physical length scales of a pixel vertical length ranges from 0.2 to 1.4 m. This indicates that a pixel error in image registration to real-world coordinates can cause mis-positioning error of up to 1.4 m at the offshore boundary areas.

The physical distance errors caused in the image rectification processes in this study were evaluated using the measured locations and the predicted locations of ground control points after the image rectification, and the measured instrument locations and the observed instrument locations in the rectified real-world coordinate frame. In order to quantify error of image rectification, i.e. errors between the predicted and the measured locations of the ground control points and the instruments, biased distance errors in the alongshore (x) and the cross-shore (y) directions were

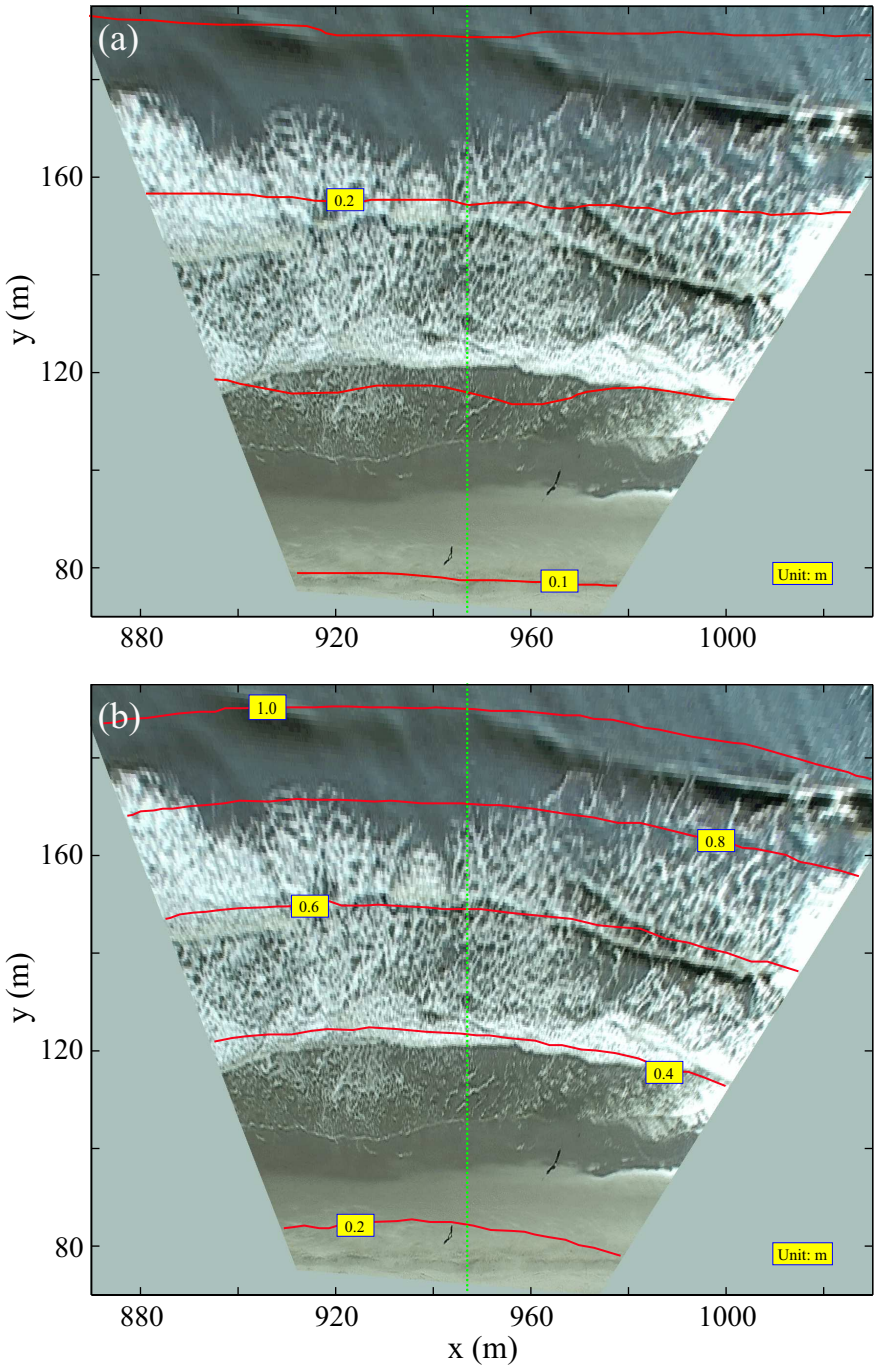

Figure 54: Physical length scales of an image pixel after image rectificatoin in Case 1: (a) physical length scales of one pixel horizontal length, (b) physical dimensions of one pixel vertical length.

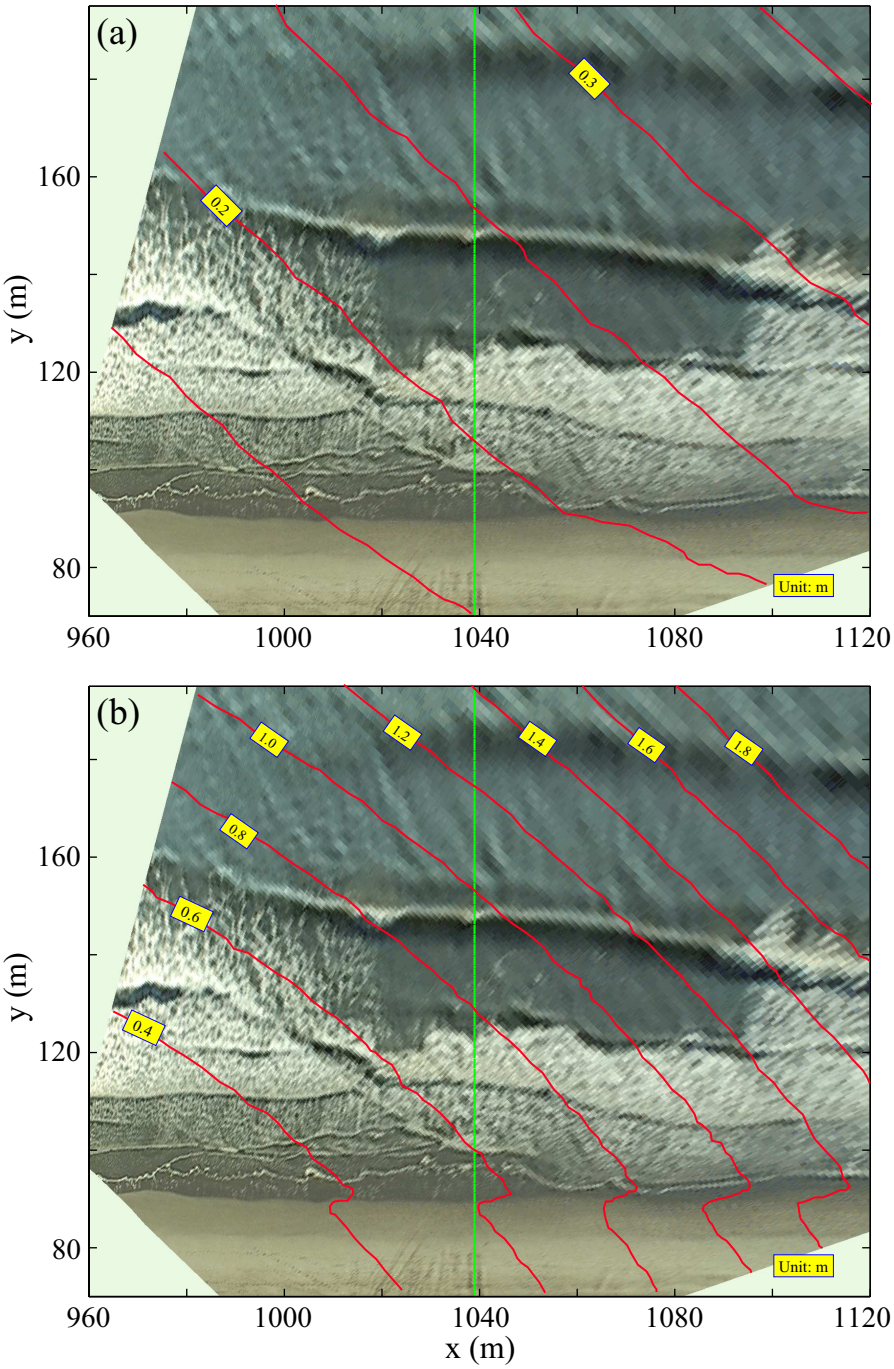

Figure 55: Physical length scales of an image pixel after image rectificatoin in Case 4: (a) physical length scales of one pixel horizontal length, (b) physical length scales of one pixel vertical length.

computed respectively:

$$\Delta x = \frac{1}{N}\sum_{i=1}^{N}(x_p - x_m)_i \tag{63}$$

$$\Delta y = \frac{1}{N}\sum_{i=1}^{N}(y_p - y_m)_i \tag{64}$$

where the subscripts p, m and N denote the predicted, the measured and number of data points respectively. Fig. 13 in Chapter III presents the collected locations of ground control points in the image frame and the comparison of their measured and predicted locations in the real-world coordinates in Case 1. The rectified (or predicted) physical locations of the ground control points collected from the image sequence were compared to the in-situ measured locations. The comparison in Fig. 13(b) for Case 1 shows excellent match between the predicted and the measured locations of ground control points. Table 12 summarizes the evaluated biased-distance errors of the image rectification processes for all four datasets.

In general, the image rectification accuracy in the dry beach regions for all four datasets produced consistently very small physical distance errors of less than 0.2 m, compared to the length scale of the area of the interest on the order of $\sim$ 100 m. In particular, the biased distance errors in the cross-shore directions are less than 0.1 m. Interestingly, in Case 1 with the oblique-top view image frame, the error in x-direction is less than Δy, while vice versa in the other three cases with the oblique-side view image frame.

Since video-based physical analyses for wave processes were conducted in the surf zone, it is more important to validate the rectification accuracy in the wave breaking zone. The locations of the deployed instruments in the surf zone for Cases 1 and 3 were identified in the rectified image frame and compared to the in-situ measured locations of the instruments as presented in Table 12. The locations of the deployed instruments in Cases 1 and 3 could be identified in the rectified image frame while

Table 12: Image rectification errors on the dry beach and in the surf zone.

Case No.	Errors in dry beach (using positions of GCPs)			Errors in the surf zone (using positions of instruments)		
	# of GCPs	Δx (m)	Δy (m)	# of instruments	Δx (m)	Δy (m)
I	18	0.01	-0.13	4	-0.81 (0.39)*	-0.68 (0.08)*
II	23	-0.08	-0.04	4	-	-
III	23	-0.18	-0.09	4	-0.29	0.03
IV	23	-0.14	-0.05	3	-	-
Notes	Δx : biased distance error in the alongshore direction (in average). Δy : biased distance error in the cross-shore direction (in average). * : biased distance error (in median).					

they were removed for data downloading in the early evenings. Video segments of the instrument removal process in Cases 2 and 4 failed to present valid instrument locations due to camera shifting problems caused by sun heating the camera tripods.

Fig. 56 presents the identified instrument locations and the surveyed locations for Cases 1 and 3, and shows excellent matches between them, with distance errors less than 0.3 m except for the second instrument (Aquadopp C) location from the offshore boundary in Case 1. The large mismatch of the Aquadopp C location is probably due to eventual wrong positioning of its actual location during the instrument location survey using a total station rod. At the time of the in-situ location survey in Case 1, the water level was above the waist of the rod man with roughly 0.3 m wave heights so that the rod man may have had difficulties in positioning. Excluding the Aquadopp C location, it is seen from Table 12 that the image rectification errors (Δy) in the cross-shore direction are less than 0.1 m, being consistent with the rectification accuracy in the dry beach area.

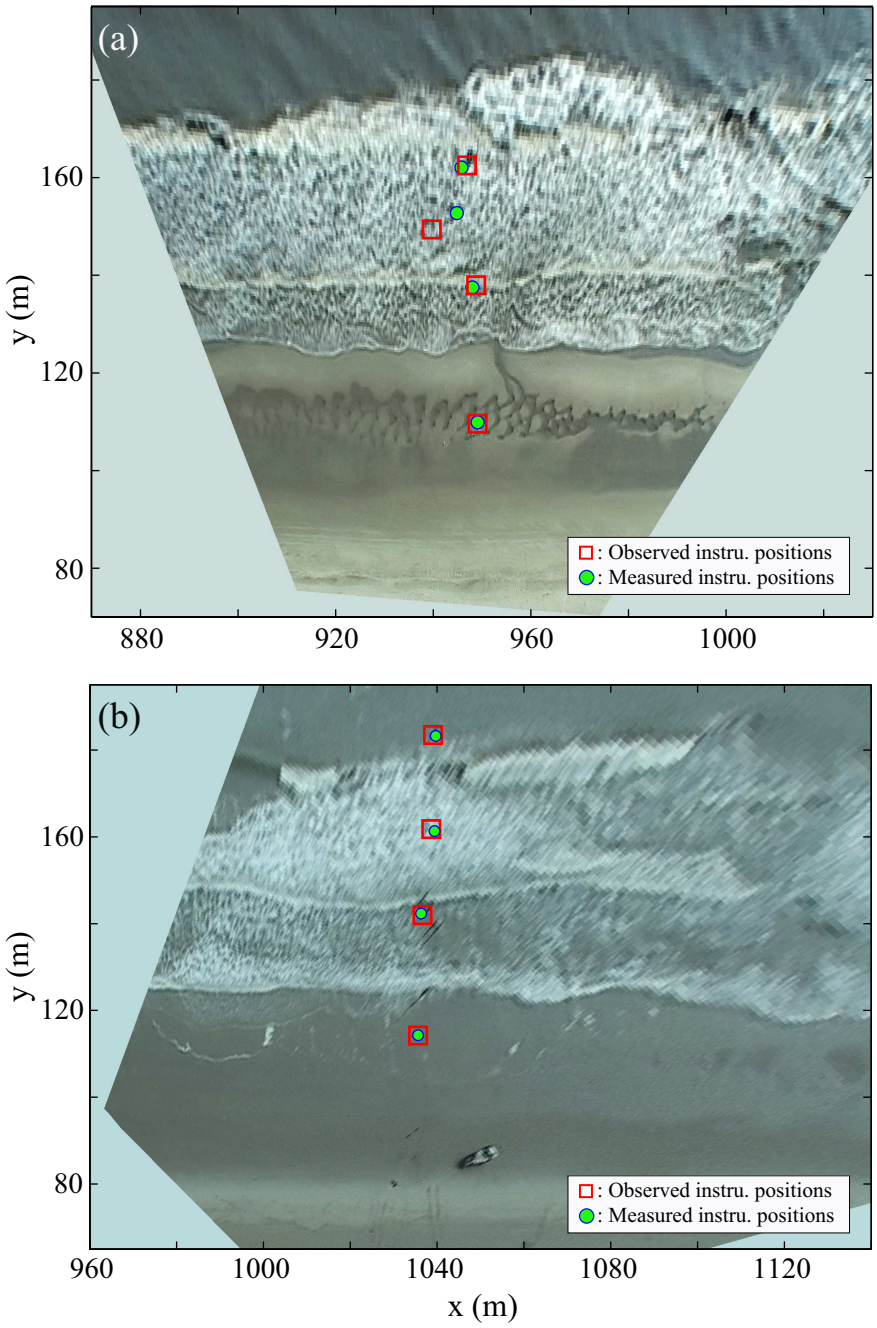

Figure 56: The locations of the deployed instruments identified in the rectified frames and their comparisons with the in-situ measured locations: (a) Case 1, (b) Case 3.

Another possible error during the image rectification processes is introduced when constraining the water surface to be flat to determine the Direct Linear Transformation model solution. If the elevation is inaccurate, the transformation may affect the accuracy of the world coordinate physical analysis. Throughout the present study, the wave crests were assumed to be at the still water level. However, the wave crests propagate at a higher elevation than the still water level, and transform after wave breaking with a decrease in wave height. In addition, the mean water level changes during the dataset time span due to the tidal influence. The higher elevation of the wave crests than the constrained flat water surface may lead to a mis-registration of the exact wave crest positions in the rectified domain.

The mis-registration caused by the vertical movements of the wave crests was quantified by assuming that the crest elevation is 1 m above the constrained still water level and computing horizontal space shift compared to the mis-registration-free (original) space domain. Horizontal space shifts caused by the mis-registration of the wave crests were computed for Cases 1 and 4. In the horizontal space shift calculation, it was assumed that all wave crests are at the horizontal 2-D space 1m above the still water level, and the rectified domain from this 1m higher horizontal space is the mis-registration-free space domain.

The horizontal space shifts in the cross-shore direction for both cases ranged from 2.0 to 3.2 m along the cross-shore transects over the surf zone, increasing with increase of the distance from the cameras. The horizontal space shifts in the longshore direction for both cases were uniform as -0.2 m and 2.2 m, respectively, along the cross-shore transects. This uniform mis-registration of the space shifts in the longshore direction is negligible in physical analysis, i.e. computation of wave celerity using wave crest trajectories, since the uniform biases of the horizontal space shifts do not influence on wave celerity calculation. Similarly, the horizontal space shifts in the cross-shore direction, ranging from 2.0 to 3.2 m over the surf zone, can be

considered. If the common bias of 2.0 m is subtracted from the range of 2.0 to 3.2 m, the range of effective horizontal space shifts in physical analysis becomes 0.0 to 1.2 m. Considering that most of incoming waves in each of the four datasets have wave amplitudes of less than 0.25 m, the effective horizontal space shifts in the cross-shore direction reduce to the range of 0 to 0.3 m, based on the guess by the linear interpolation.

Wave celerity was estimated using individual wave trajectories identified from the rectified image sequences having those rectification and mis-registration errors. Waves propagate through the surf zone on a length scale of 100 m. Compared to the length scale of the surf zone, length scales of those rectification and mis-registration errors are very small, being less than 1 %. Thus, the physical distance errors involved in the rectification processes are negligible in estimating wave propagation speeds through the surf zone.

6.3 Adequacy of image processing parameters

To extract wave crest features, several image processing parameters are determined, and the main parameters are selected as: 1) image frame sampling rate associated with the image frame differencing method, 2) interrogation window size for the directional low-pass image filtering, 3) sub-window size for the crest feature detection in the processed image timestacks, and 4) minimum pattern repeatability number during a dataset time-span for filtering the extracted wave crest trajectories by the pattern repeatability validation. The first two parameters were obtained by utilizing the mean speed of wave crests computed by the PIV method in the image domain. The third and last parameters were determined based on the assumption that the wave celerity is almost constant over the sub-window and an incoming wave propagation pattern in the surf zone is repeated multiple times at least more than the minimum pattern

repeatability number during a dataset time-span, respectively.

The wave crest displacement per second in the image domain was used to determine the optimal image frame sampling rate associated with the image frame differencing method to effectively reduce the effect of the drifting foam signals from the wave signals. The determination of the image sampling rate derived in Eq. 16 was based on the constraint that the displacement (in pixels) of the wave crests per sampling frame interval (dt) is set to about 2 pixels/dt, while the speed of slower moving foam is automatically limited to 0 or less than 1 pixel/dt. The mean speeds of the wave crests estimated in Case 1 (oblique-top image view) and Case 2 (oblique-side image view) determined the sampling rate f_s as approximately 3 Hz for both cases. In order to investigate the adequacy of this sampling rate for foam removal, directionality of the wave crests retained after image frame differencing implemented with different sampling rates were measured for both cases by utilizing the 2-D Fourier transform as shown in Fig. 57.

The image sequences for Cases 1 and 2 were processed by the image frame differencing method using different image sampling rates ranging from 1 to 15 Hz. The frame-differenced images (for instance, Fig. 57(a)(c)) were 2-D Fourier transformed as shown in Fig. 57(b)(d). Thereafter, frequency components with energy above the mean of the 2-D energy spectrum were isolated in the frequency domain to compute the directionality of the retained wave crests. The directionality is represented by the coefficient of determination (or R-square R^2) obtained by applying the linear regression to the isolated frequency components, expressed as (u, v) in the 2-D Fourier spectrum domain coordinates. The R-square denotes the strength of the linear association between u and v, and represents the percent of the data that is the closest to the line of best fit. Thus, as the R-square is larger, so the directionality of the wave crest features is stronger, having less foam signals non-directional in the frame-differenced images. Fig. 57(e) and (f) present variation of the R-square for the sampling rates

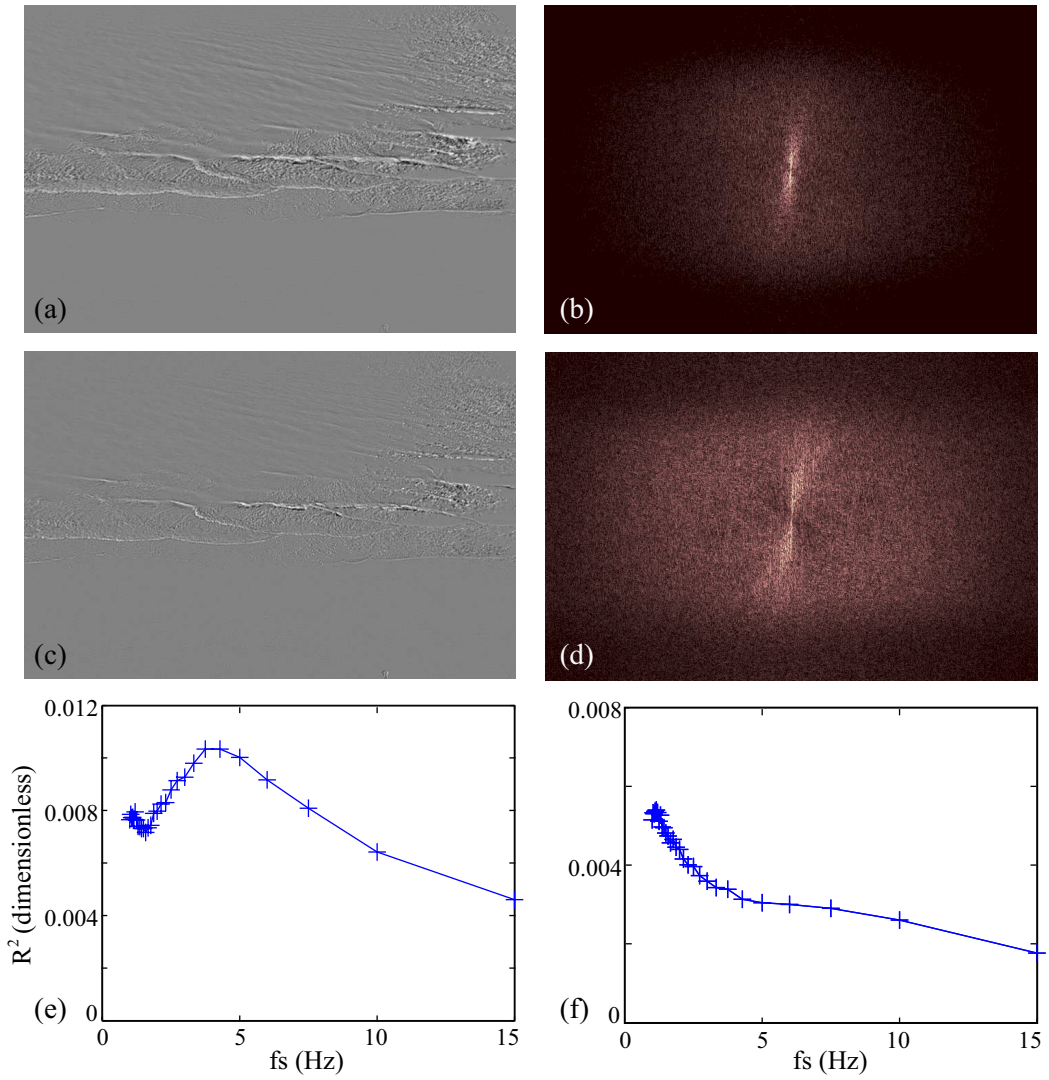

Figure 57: Directionalities (R-square) of the frame differenced image frames for different image sampling rates: (a) a frame differenced image with 3 Hz, (b) normalized 2D Fourier spectrum of (a), (b) the frame differenced image with 10 Hz from the raw images same to (a), (d) normalized 2D Fourier spectrum of (c), (e) variation of R-square (directionality) for different sampling rates in Case 1, (f) variation of R-square (directionality) for different sampling rates in Case 2.

ranging 1 to 15 Hz for Cases 1 and 2 respectively. These two plots indicate that the image frame differencing with less than 5 Hz results in larger R-squares, i.e. stronger directionalities of the frame-differenced images, thereby removing the foam induced-noise and retaining the wave crest features effectively. The image frame differencing with larger than 5 Hz degraded the directionality of the elongated wave crest features in the image frame, since too small image frame time intervals lost much of the wave crest feature signals. Fig. 57(c) and (d) visualize this tendency that the 2-D spectrum with the lower sampling rate strengthened directionality of the frame difference image while the spectrum with the higher frequency weakened the directionality. In general, it is seen from the two R-square plots that the sampling rate of 3 Hz determined by Eq. 16 resulted in the level of stronger directionality of the frame differenced images, compared to the higher frequencies.

The wave crest displacement per second captured in the image domain was also used to determine the sub-window size of 64×64 pixels for interrogating and filtering local areas of the frame-differenced image sequences by a directional low-pass filter. The sub-window size was determined to be equivalent to the length scale of the wavelengths (in pixels) of incoming waves in the image domain, intending to retain approximately one wave crest over the sub-window. The wavelengths in the image domain were computed by multiplying the phase speed of the wave crests by the wave period. The mean phase speeds of the wave crests in the image frames for Cases 1 and 2 were 5.42 and 6.87 pixels/s respectively. The incident wave period range was limited to 3 to 15 seconds in this study. Hence, the mean wave phase speeds multiplied by the mean (i.e. 9 seconds) of the wave period range produced the wavelengths 48.8 and 61.8 pixels for Cases 1 and 2 respectively. Those values suggested the nearest 2-bit integer of 64 for the sub-window size. If the sub-window size is too big, image filtering in that size will loose local curvatures of the wave crest features in it. If the sub-window is too small, the sub-window can fall between the wave crests, increasing

computation times. For these reasons, the sub-window size was determined based on the wavelength scale evaluated from the wave phase speeds in the image domain.

The crest tracking sub-window to detect and extract wave crest trajectories in the processed image cross-shore timestacks using the Radon transform was selected as 50 × 50 pixels, i.e. 5 m × 16.67 s ($H \times W$). The crest tracking sub-window was used in the intermediate and outer surf zones where change of the wave crest celerity was not significant, i.e. the wave crest trajectories in the timestacks were almost straight lines over the cross-shore distance of 50 pixels (or 5 m). The straight line segments of the wave crest tracks in the sub-window were detected and extracted by identifying the highest energy peak in the Radon transformed energy spectrum. If the highest energy peak greatly exceeds the other energy components, then the wave crest feature will be readily and precisely detected. Fig. 58 presents the ratio of the highest energy peak to the energy spectrum background for different sizes of the crest tracking sub-window applied to the processed image timestacks for Cases 1 and 2. Only square sub-windows were considered to simplify relational cases between sub-window sizes and the ratios of the highest energy peak to the energy spectrum background. Sub-windows having different shapes such as rectangular window can be used, depending on characteristics of wave trajectories in the processed timestacks.

The ratio (r_{peak}) of the highest energy peak to the energy spectrum background was computed by:

$$r_{peak} = \frac{E_{peak}}{E_{mean} + E_{std}} \tag{65}$$

where E_{peak} is the highest energy peak value, E_{mean} is the mean of the energy spectrum, and E_{std} is the standard deviation of the energy spectrum. Fig. 58 shows that the ratios for both Cases tend to increase linearly with increase in sub-window size, meaning that bigger window size resulted in an enhanced energy peak, readily enabling line detection. If the line detection is conducted with larger sub-window

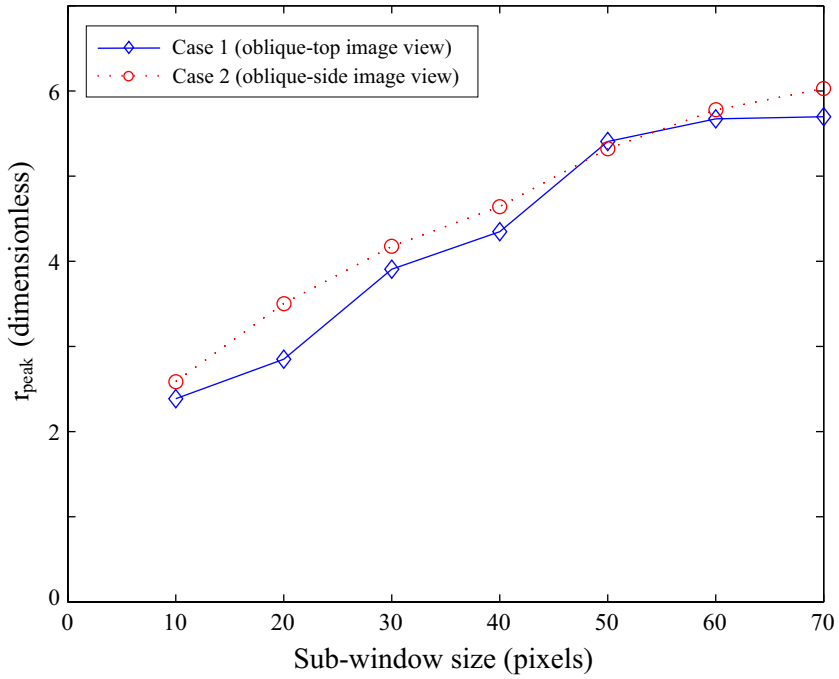

Figure 58: Ratio of the highest energy peak to the energy spectrum background for different sizes of the crest tracking sub-window.

sizes (e.g. more than 10 m), however, locally changing wave crest features such as wave celerity transition across the breaker points will be lost. In this perspective, it is seen from Fig. 58 that the vertical sub-window size of 5 m used throughout the present study is an appropriate window size large enough to readily detect the lines.

For filtering out erroneous wave crest trajectories, it was assumed that wave propagation patterns are repeated at least more than five times during the dataset time-span. Since erroneous wave crest tracking patterns caused by unexpected noisy intensity signals are not likely to happen repeatedly with the same shapes, the erroneous wave trajectory patterns were assumed to be repeated less than five times during the dataset time-span. So, throughout the present study, the minimal pattern repeatability number 5 was selected to retain the real wave crest trajectories. The pattern repeatability of each crest trajectory was investigated by the k-means clustering method. In order to look into the adequacy of the minimal pattern repeatability

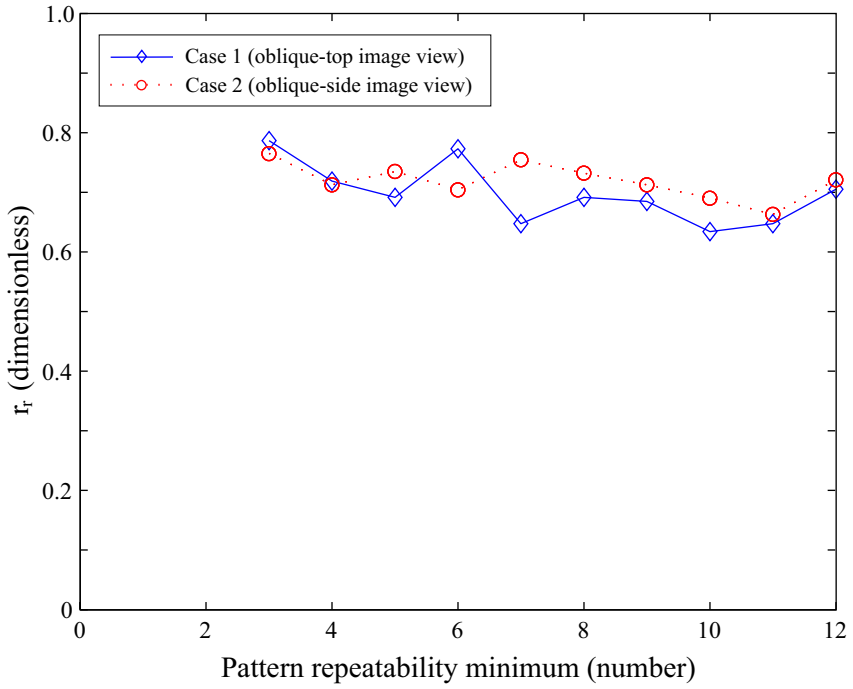

Figure 59: Ratio of the retained crest track number to the initial crest track number after filtering out the erroneous crest tracks for different pattern repeatability minimum numbers ranging from 3 to 12.

number 5, different minimal pattern repeatability numbers ranging from 3 to 12 were tested. Fig. 59 presents the ratio (r_r) of the retained crest track number to the initial crest track number after filtering out the erroneous crest tracks for different minimal pattern repeatability numbers.

From Fig. 59, it is seen that the ratios do not change significantly over the different pattern repeatability minimum numbers ranging from 3 to 12, keeping consistent ratios of the retained valid wave crest tracks around 0.7, even though the ratios have a tendency to decrease slightly with increase of the pattern repeatability minimum number. This indicates that most of the erroneous wave crest trajectory patterns were repeated no more than 2 times, and the pattern repeatability minimum number 5 selected in this study filters out most of the erroneous crest trajectories.

6.4 Errors in the adopted equations in the depth inversion algorithm

The majority of the adopted equations for the nonlinear depth inversion model such as the breaker formula, the wave dissipation formula and the relation between the wave height and the wave crest elevation were established empirically or semi-empirically via comparison to data from monochromatic wave experiments at laboratories. Well investigated studies for those equations in random wave fields are lacking, and there may be deficiencies in those equations when they are tested with random waves in the field. For instance, coefficients of the breaker criteria determined through laboratory experiments were observed to be reduced by up to 30% when they were compared to the irregular wave breaking cases as shown in Chapter V. Hence, the adopted breaker formula in this study had to be modified based on a couple of the wave breaking observations conducted for irregular waves in the laboratories or the inner surf zone. The deficiencies in the adopted equations for irregular waves possibly contributes to the errors in the depth inversion model.

The adopted equations for irregular waves in the surf zone have not been well investigated with wave-by-wave approaches, thereby resulting in difficulties of quantifying the accuracy of those equations applied in the depth inversion. The sensitivity of the depth inversion model to the variability of the model components was tested instead by introducing a perturbation δ to each of the parameters involved in the model components and assuming the others to be constant. Table 13 presents grouping of the parameters involved in each of the model components which can be variable depending on sea state conditions and were used in the sensitivity tests.

Other than the parameters of the model components in Table 13, wave properties, which were estimated from the video image sequence, are included, since their video-based estimates have uncertainties. In Chapter IV, for instance, the wave celerity transitions across the breaker points larger than the approximate nonlinear shallow

Table 13: Grouping of the model component parameters used for sensitivity analysis.

Model components	(wave properties)	WBM	WDM	WSM
Parameters	- Wave celerity (C) - Wave period (T)	- Breaker formula coeffcient (f_b) - Ratio η_b /H_b	- Decay coeff. (K) - Stable factor (Γ) - Ratio η/H	- Ratio η/H

water wave equation-based celerity were observed and adjusted to be comparable to the approximated nonlinear shallow water wave equation-based celerity. In addition, instantaneous wave period for each of individual waves were determined using the wavelet analysis to comply with the wave-by-wave approach in the depth inversion.

For the sensitivity tests, video-derived wave properties, model component parameter and beach profile data of one of the four datasets (Case 4) were used as input data, and six perturbations (-20, -10, -5, 5, 10, 20%) were applied to input values for the nonlinear depth inversion. The three negative perturbations were not applied to input values of wave celerity, since these negative perturbations could cause the input values of wave celerity to be less than shallow water linear wave theory-based wave celerity. In addition, the 1.2 factor of wave celerity transition for adjusting video-based celerity estimates was considered in input values of the wave celerity. The beach profile inverted correspondingly to each of the parameter perturbations was compared to the original bathymetry, computing error relative to the nonlinear predictions of bathymetry caused by the perturbation. Table 14 presents the results of the sensitivity tests of the variability of the model component parameters to the nonlinear depth inversion.

The results of the sensitivity tests show that the nonlinear depth inversion model is most sensitive to errors in wave celerity estimates. This means that accurate estimation of the wave celerity is most critical for prediction of the water depth

Table 14: Errors relative to the nonlinear predictions of bathymetry caused by perturbations through sensitivity analysis.

Parameters		C	T	f_b	η / H	K	Γ
δ (%)	-20	-	0.66	2.3	6.6	1.47	2.0
	-10	-	0.67	1.0	3.0	1.04	1.3
	-5	-	0.68	0.6	1.3	0.90	1.0
	+5	9.5	0.67	1.1	1.9	0.80	1.1
	+10	19.8	0.70	1.6	3.1	0.85	1.6
	+20	41.7	0.71	2.7	5.4	0.98	2.4
Notes		Normalized relative errors caused by the perturbations (%)					

through the depth inversion algorithm. Locally large depth errors commonly found in the area of the intensive wave breaking (i.e. the wave celerity transition area) in the nonlinear depth inversion in Chapter V can be explained in this perspective. Even though the wave celerity transitions were adjusted to be comparable to the nonlinear shallow water wave celerity, the adjusted celerity estimates were still larger than the nonlinear celerity. In order to improve depth predictions in the wave celerity transition area, more definitive investigations on wave celerity transition for various wave conditions and beach systems are required. The effect of the perturbations added to the original celerity on the depth predictions can be assessed from the nonlinear shallow water wave equation-based wave celerity equation re-arranged as $h = c^2/g - \eta_c$. The little variation in c can be related to variation in h as

$$\Delta h \,(= h_\delta - h_\circ) \sim \frac{1}{g}\Delta\left(c_\delta^2 - c_o^2\right) \tag{66}$$

where the subscripts o and δ denote the original and the perturbed values respectively. The error amounts generated by the perturbations of the wave celerity in Table 14 are accounted for by the above equation.

The perturbations applied to the ratio η/H, the breaker formula coefficient f_b and the stable wave factor Γ caused relatively very small errors in the depth inversion compared to the perturbations of the wave celerity. If the wave celerity estimates are made accurately, however, these parameters can play key roles for the accurate depth inversion. In this sense, if the good agreement trends between the predicted and the measured beach profiles except the wave celerity transition area shown in Chapter V are considered, those parameters were well suited to model transformation of irregular waves in the surf zone.

The depth inversion model was very robust regarding changes to the wave period and the decay coefficient, producing less than 2% errors even for perturbation of $\pm 20\%$. Wave dispersion in shallow water is almost independent of wave period and

wavelength, and the wave celerity equation includes the amplitude dispersion effect only. The wave period is only involved in prediction of breaking wave height and water depth, ultimately making no difference in depth prediction. Dally et al. (1985) already showed that the wave dissipation formula with the fixed decay coefficient K represented robustly wave transformation for different beach slopes. The sensitivity tests with changes of the decay coefficient also showed similar robustness of the present depth inversion to K.

6.5 Summary

Various error sources contributing to the results of the wave signature extraction, the wave property estimation and the nonlinear depth inversion were analyzed herein. The 3 investigated error sources are: accuracy of video image rectification processes, adequacy of image processing parameters, and accuracy of the adopted equations in the wave property estimation and the nonlinear depth inversion.

It was shown that the physical errors locally induced in the image rectification processes were very small compared to the entire space domain. The image rectification error was less than 0.1 m. The horizontal mis-registration error in terms of the relative space shift during wave propagation was less than 0.5% compared to the length scale of the surf zone. In addition, several image processing parameters determined during the image processing steps to extract wave crest features were found to be adequate to promote wave crest feature extraction. The investigated image processing parameters are: the image frame sampling rate associated with the image frame differencing method, the interrogation window size for the directional low-pass image filtering, the sub-window size for the crest feature detection in the processed image timestacks, and the pattern repeatability minimum number for filtering out the erroneous wave crest trajectories during a dataset time-span.

The errors in the depth inversion caused by the variability of the adopted equations

for transformation of irregular waves in shallow water were quantified through the sensitivity tests. The sensitivity tests showed that the most significant error source in the present nonlinear depth inversion is the inaccuracy in the wave celerity estimation. The inaccuracies in the other parameters such as the ratio η/H, the breaker formula coefficient f_b, the stable wave factor Γ, the decay coefficient K and the wave period T caused relatively very small errors in the depth inversion compared to the errors by the perturbations of the wave celerity.

CHAPTER VII

CONCLUSIONS

Various remote sensing techniques have been applied to invert the nearshore water depths by utilizing remotely measured wave properties. Among them, the video imaging technique has provided temporally and spatially high resolution observations of ocean waves and coastal bathymetry, even though the accuracy for wave measurements and depth inversions is degraded in the surf zone due to wave breaking induced white foam signals. This thesis compliments earlier video-based nearshore depth inversion studies by improving wave property estimation and developing a nonlinear depth inversion algorithm in the surf zone. This chapter summarizes the thesis results, and describes outlook and some future research considerations.

7.1 Summary of the results

Results can be summarized in two aspects: (1) nearshore wave properties such as wave celerity, wave period (wavelength) and incident wave angle were successfully estimated using video imaging techniques, in particular, extracting wave crest features out of noisy foam patches generated by wave breaking; (2) the nonlinear depth inversion algorithm for the nearshore depth inversion was successfully developed by utilizing the estimated wave properties and the breaking wave heights retrieved from video image sequences. The detailed results of the wave crest feature extraction and the wave property estimation by the newly-developed video-based wave observation methodology can be summarized as follows:

- The experimental field data from 2003 Myrtle Beach data collections (Haas et

al., 2004) were used for this study. Four different video datasets selected with various sea state and imaging conditions were used to retrieve depth-influenced wave properties.

- In order to remove noisy signals due to foam generated by wave breaking from nearshore video image sequences, object-oriented image processing methods, such as image frame differencing and directional low-pass image filtering, were applied by characterizing object displacements and orientations in the image sequences. Object-oriented image processing methods eliminated slowly moving foam patches from the image sequences, successfully retaining faster moving wave crest features.

- A Radon transform-based line detection algorithm was successfully applied to identify individual wave crest trajectories from the processed image sequences, i.e. the processed cross-shore image timestacks, by tracking pixels of highest intensity within an interrogation window of Radon transform.

- The number of realistic wave crest trajectories identified from the processed timestacks is about twice the number of the first highest 1/3 waves in the record.

- Wave celerity, period, wavelength, and angle were quantified using a wave-by-wave approach by utilizing individual wave crest trajectories extracted in the processed image timestacks.

- The estimated wave celerity showed wave celerity transition across the breaker point larger than the nonlinear shallow water wave equation-based celerity approximation. The wave celerity transition was adjusted, based on the previous investigations on wave celerity changes in the surf zone, in order for the nonlinear shallow water wave equation-based depth inversion to perform properly.

- The video-based celerity estimates had a normalized relative error of about 12.3%, over-biased due to the inclusion of the nonlinear amplitude dispersion effects, compared to the linear wave theory. However, the relative error was significantly reduced to 2.6% in average in the comparison with the approximate nonlinear shallow water wave equation-based celerity computed using the measured depths and pressure head data (i.e. wave heights).

- The sole wave periods for individual waves under the random wave circumstance determined using wavelet analysis were well compared to the significant wave period T_s and the mean period T_m obtained from the measured pressure head data, within a wave period difference of less than 0.5 s in average.

- The video based wave angle estimates at the instrument locations were well compared to the wave angle (the peak frequency and dominant wave angles) measurements computed by directional wave spectrum analysis, in particular, to the dominant wave angles defined as the direction with the highest energy integrated over all frequencies.

A nonlinear depth inversion algorithm was developed in this study. Beach profiles in the surf zone were successfully inverted by utilizing the video-derived wave properties. The nonlinear depth inversion model involves three model components: the wave breaker model, the wave dissipation model, and the wave shoaling model. Results of the nonlinear depth inversion in the surf zone derived from video imagery can be summarized as follows:

- The wave breaker model, composed of a modified Miche breaker criterion and the approximate nonlinear shallow water wave equation-based celerity equation, was used to predict the wave height and water depth at the breaker point by

utilizing video derived wave properties. The wave breaker model could retrieve the breaker heights and depths from nearshore mono-video imagery innovatively.

- The wave dissipation model, composed of the Dally wave dissipation formula and the approximate nonlinear shallow water wave equation-based celerity equation, computed wave heights and water depths after wave breaking, starting from the breaker point toward the shoreline.

- The wave shoaling model, composed of Green′s law and the approximate nonlinear shallow water wave equation-based celerity equation, was used to derive wave heights and water depths before wave breaking in the seaward direction starting from the breaker point.

- The nonlinear depth inversion-derived beach profiles were comparable to the measured bathymetry with a biased mean depth error of +0.06m within ± 0.10m for the depth range of 0.1 to 3 m. In contrast, the linearly inverted depth profiles were systematically over-estimated over the entire surf zone having a biased mean depth error of about 0.38 m, due to the neglect of the amplitude dispersion effects.

- The wave heights predicted within the nonlinear depth inversion algorithm had a biased wave mean height error of +0.14 m, compared to the significant wave heights obtained from the in-situ measured pressure data. The predicted breaker heights were found to be at the level of the maximum wave heights, having a tendency to be slightly over-estimated compared to the maximum wave heights.

- When the effect of the incident wave angle θ on the inverted depth was investigated, the predicted depths with inclusion of the angles were approximately $h_o(cos^{-2}\theta - 1)$ deeper than the predicted depths h_o without the wave angles.

- Regarding error sources influencing on the nonlinear depth inversion, accurate

estimation of wave celerity was found to be most critical for prediction of wave depth by sensitivity analysis.

7.2 Outlook and future research considerations

Complementary research issues are found from this study in two aspects: 1) experimenting with different beach systems, 2) verifying the adopted equations in the depth inversion for modeling irregular wave transformation in the surf zone for wave-by-wave approach.

The video and field datasets in this study were selected from the data collections at the Myrtle Beach having a weakly barred beach system, even though the datasets were selected to have various sea state and video imaging conditions. Wave properties and water depths derived from those video datasets showed good agreements with the in-situ measurements at the weakly barred beach. Furthermore, applicability of the present image process methodology and the suggested nonlinear depth inversion model to other beach systems, e.g. strongly barred or double-barred beach systems can be tested.

The equations involved in the nonlinear depth inversion model, such as the breaker formula, the wave dissipation formula, the wave refraction formula and the relation between the wave height and the wave crest elevation, are the ones which were established empirically or semi-empirically through regular wave experiments at laboratories. In addition, wave celerity transition across the breaker points larger than the nonlinear shallow water wave theory was observed in this study, but well defined formulas for the celerity transition and evolution over the wave breaking zone are not documented. In fact, dense instrumentation over the wide surf zone is basically required to investigate those wave celerity transition-related formulas for irregular waves in the field, being cost and labor intensive. In contrast, the present image

processing methodology enables irregular individual waves in wave image sequences to be detected and traced entirely over the surf zone with wave-by-wave approach. Using the present wave observation methodology, the following research issues can be investigated to better understand wave processes for irregular waves in the surf zone, thereby complimenting the present nonlinear depth inversion: wave breaking indexes for irregular waves in the field, wave refraction through the surf zone, wave celerity transition across the breaker points and evolution through the surf zone.

REFERENCES

Aarninkhof, S.G.J., and B.G. Ruessink. 2004. Video observations and model predictions of depth-induced wave dissipation. *IEEE Trans. on Geoscience and Remote Sensing*, 42(11), 2612- 2622.

Aarninkhof, S.G.J., B.G. Ruessink, and J.A. Roelvink. 2005. Nearshore subtidal bathymetry from time-exposure video images, *J. Geophys. Res.*, 110, C06011, doi:10.1029/2004JC002791.

Adler-Golden, S.M., P.K. Acharya, A. Berk, M.W. Matthew and D. Gorodetzky. 2005. Remote Bathymetry of the Littoral Zone from AVIRIS, LASH, and QuickBird Imagery, *IEEE Trans. on Geos. and Rem. Sens.*, 43 (2), 337-347.

Battjes, J.A. and J.P.F.M Janssen. 1978. Energy loss and set-up due to breaking of random waves, *Proc. of 16th Conf. on Coastal Eng.*, ASCE, 567-587.

Battjes, J.A., and M.J.F. Stive 1985. Calibration and verification of a dissipation model for random breaking waves, *J. of Geophys. Res.*, 90(C5), 9159–9167.

Bell, P. S. 1999. Shallow water bathymetry derived from an analysis of X-band marine radar images, *Coastal Engineering*, 37, 513-527.

Benny, A. H., and G. J. Dawson. 1983. Satellite imagery as an aid to bathymetric charting in the Red Sea, *Cartogr. J.*, 20, 5–16.

Bierwirth, P. N., T. J. Lee, and R. V. Burne. 1993. Shallow sea-floor reflectance and water depth derived by unmixing multispectral imagery, *Photogramm. Eng. Remote Sens.*, 59(3), 331– 338.

Catalan, P.A. 2005. Hybrid approach to estimating nearshore bathymetry using remote sensing, M.S. Thesis, Ocean Eng., Oregon State Univ.

Chang, K.-A., and P. L.-F. Liu. 1998. Velocity, acceleration and vorticity under breaking waves, *Physics of Fluids*, 10, 327-329.

Chickadel, C.C., R.A. Holman, and M.F. Freilich. 2003. An optical technique for the measurement of longshore currents, *Journal of Geophysical Research*, 108 (C11), 3364, doi:10.1029/2003JC001774.

Dally, W.R. 1992. Random breaking waves: Field verification of a wave-by-wave algorithm for engineering application, *Coast. Eng.*, 16, 369-397.

Dally, W. R., R.G. Dean, and, R.A. Dalrymple. 1985. Wave height variation across beach of arbitrary profile, *J. Geophys. Res.*, 90(C6), 11917-11927.

Dalrymple, R.A., A.B. Kennedy, J.T. Kirby, and Q. Chen. 1998. Depth inversion for nonlinear waves shoaling over a barred-beach, *in Proc. 26th Inter. Conf. on Coast. Eng.*, 2395-2408.

Dean, R.G., and R.A. Dalrymple. 1991. Water wave mechanics for engineers and scientists, *Advanced Series on Ocean Engineering 2*, World Scientific, Singapore.

Dibajnia, M. 2002. Observation of waves in the surf and swash zones using particle image velocimetry, *in Proc. 28th Inter. Conf. on Coast. Eng.*, 955-967.

Dugan, J.P. 1997. Bathymetry estimates from long range airborne imaging systems, *Proc. of 4th Int. Conf. on Remote Sensing for Marine and Coastal Environments*, Orlando, FL.

Dugan, J.P., C.C. Piotrowski, and J.Z. Williams. 2001. Water depth and surface current retrievals from airborne optical measurements of surface gravity wave dispersion, *J. Geophys. Res.*, 106(C8), 16903–16915.

Eubank, R.L. 1988. Smoothing Splines and Nonparametric Regression. New York: Marcel Decker.

Fritz, H.M. 2002. PIV applied to landslide generated impulse waves, In: Adrian, R.J. et al. (eds) Laser techniques for fluid mechanics, 305-320, Springer, New York, Berlin, Heidelberg.

Fritz, H.M., W.H. Hager, and H.-E. Minor. 2004. Near field characteristics of landslide generated impulse waves, *Journal of Waterway, Port, Coastal, and Ocean Engineering*, 130(6), 287-302.

Gonzales, R.C., and R.E. Woods. 1992. Digital Image Processing, 716 pp., Addison-Wesley-Longman, Reading, Mass..

Greidanus, H. 1997. The use of radar for bathymetry in shallow seas, *The Hydrographic Journal*, 83, pp. 13–18.

Grilli, S.T. 1998. Depth inversion in shallow water based on nonlinear properties of shoaling periodic waves. *Coastal Engineering*, 35(3), 185-209.

Haas, K., H. Demir, P. Work, G. Voulgaris, and S. Obley. 2004. Myrtle Beach Nearshore Experiment, Dec 10 to Dec 15th, 2003, Part II: Morphodynamic and Remote Imagery Measurements, Technical Report, School of Civil and Envi. Eng., Georgia Tech – Savannah.

Haller, M.C., Dalrymple, R.A., and Svendsen, I.A. 2000. Experiments on rip currents and nearshore circulation: Data report, Technical Report CACR-00-04, Center for Applied Coastal Research, University of Delaware.

Hansen, J.B. 1990. Periodic waves in the surf zone: Analysis of experimental data, *Coastal Eng.*, 14, 14-14.

Holland, T.K. 2001. Application of the linear dispersion relation with respect to depth inversion and remotely sensed imagery, *IEEE Trans. on Geos. and Rem. Sens.*, 39 (11), 2060-2071.

Holland, K.T., R.A. Holman, and T.C. Lippmann. 1997. Practical use of video imagery in neareshore oceanographic field studies, *IEEE Journal of Oceanic Engineering*, 22(1), 81-92.

Honkanen, M., and H. Nobach. 2005. Background extraction from double-frame PIV images, *Experments in Fluids*, 38, 348–362.

Horikawa, K. and C.T. Kuo. 1966. A Study of wave transformation inside surf zone, *Proc. of 10th Coastal Eng. Conf.*, ASCE, 217-233.

Irish, J.L., and W.J. Lillycrop. 1999. Scanning laser mapping of the coastal zone: The SHOALS system, *ISPRS J. Photogramm. Remote Sens.*, 54, 123–129.

Kamphuis, J.W. 1991. Incipient wave breaking, *Coastal Engineering*, 15, 185-203.

Kamphuis, J.W. 1994. Wave height from deep water through breaking zone, *J. Waterway, Port, Coastal and Ocean Engineering*, 120, 347-367.

Kennedy, A.B., R.A. Dalrymple, J.T. Kirby, and Q. Chen. 2000. Determination of inverse depth using direct Boussinesq modeling, *Journal of Waterway, Port, Coastal, and Ocean Engineering*, 126(4), 206-214.

King, B.A., M.W.L. Blackley, A.P. Carr, and P.J. Hardcastle. 1990. Observations of wave-induced set-up on a natural beach, *J. Geophys. Res.*, 95, 22289–22297.

Kirby, J.T., and R.A. Dalrymple. 1994. Combined refraction/difraction model REF/DIF1; version 2.5 Documentation and user's manual, Tech. Rep. CACR-94-22, Center for Applied Coastal Research, Ocean Engineering Laboratory, University of Delaware.

Lee, Z., K.L. Carder, R.F. Chen, T.G. Peacock. 2001. Properties of the water column and bottom derived from Airborne Visible Infrared Imaging Spectrometer (AVIRIS) data, *J. Geophys. Res.*, 106, 11639-11651.

Leu, L.G., and H.W. Chang. 2005. Remotely sensing in detecting the water depths and bed load of shallow waters and their changes, *Ocean Engineering*, 32, 1174-1198.

Leu, L.G., Y.Y. Kuo, and C.T. Lui. 1999. Coastal bathymetry from the wave spectrum of SPOT images, *Coastal Engineering Journal*, 41, 21-41.

Lippmann, T.C., and R.A. Holman. 1989. Quantification of sand bar morphology: a video technique based on wave dissipation. *J. Geophys. Res.*, 94, 995–1011.

Lippmann, T.C., and R.A. Holman. 1991. Phase speed and angle of breaking waves measured with video techniques, *Coastal Sediments ' 91*, 542-556.

Liu, P.C. 2000. Wave grouping characteristics in nearshore Great Lakes, *Ocean Eng., 27*, 1221–1230.

Longuet-Higgins, M.S., D.E. Cartwright, and N.D. Smith. 1963. Observations of the directional spectrum of sea waves using the motions of a floating buoy. *In: Ocean Wave Spectra*, Prentice-Hall, 111-136.

Madsen, P., O. Sorensen, and H.A. SchÄffer. 1997, Surf zone dynamics simulated by a Boussinesq type model, Part I: Model description and cross-shore motion of regular waves, *Coastal Engineering*, 32, 255-287.

McCowan, J. 1891. On the solitary wave, *Philosophical Magazine*, 32, 45-58.

Miche, R. 1944. Mouvements ondulatoires de la mer, Ann. des Ponts et Chaussees, Chap. 114, 131-164, 270-292, and 369-406.

Misra, S.K., A.B. Kennedy, and J.T. Kirby. 2003. An approach to determining nearshore bathymetry using remotely sensed ocean surface dynamics, *Coastal Engineering*, 47, 265-293.

Morlet, J., G. Arens, E. Fourgeau, and D. Giard. 1982. Wave propogation and sampling theory: Part I. Complex signal and scattering in multilayered media, and Part II. Sampling theory and complex waves, *Geophysics*, 47, 203–221, 222–236.

Narayanan, C., V. Rama Rao, and J. Kaihatu. 2004. Model parameterization and experimental design numbers in nearshore bathymetry inversion, *Journal of Geophysical Research*, 109 (C08006), doi:10.1029/2002JC001756.

Obley, S., G. Voulgaris, K.A. Haas, H. Demir, and P.A. Work. 2004. Myrtle beach nearshore experiment dec. 10 to dec. 15 2003. part 1: Hydrodynamic measurements, Technical report, University of South Carolina CPSD Technical report.

Piotrowski, C. C., and J. P. Dugan. 2002. Accuracy of bathymetry and current retrievals from airborne optical time series of imaging of shoaling waves, *IEEE Transactions on Geoscience and Remote Sensing*, 165, 27-39.

Raffel, M., C.E. Willert, and J. Kompenhans. 1998. Particle image velocimetry – a practical guide, Springer, Berlin.

Rattanapitikon,W., T. Vivattanasirisak, and T. Shibayama. 2003. A proposal of new breaker height formula, *Coast. Eng. J.*, 45, 1, 29-48.

Raubenheimer, B., R.T. Guza, and S. Elgar. 1996. Wave transformation across the inner surf zone, *J. Geophys. Res.*, 101, 25589-25598.

Ruessink, B. G., I. M. J. Van Enckevort, K. S. Kingston and M. A. Davidson. 2000. Analysis of observed two- and three-dimensional nearshore bar behaviour, *Marine Geology*, 169, pp. 161–183.

Sandidge, J. C., and R. J. Holyer. 1998. Coastal bathymetry from hyperspectral observations of water radiance, *Remote Sens. Environ.*, 65, 341–352.

Sapp, B. 2006. Observations of laboratory rip currents, M.S. Thesis, Civil Eng., Georgia Institute of Technology.

Scarano, F., and M.L. Riethmuller. 2002. Advances in iterative multigrid PIV iamge processing, *Exp. Fluids, 29(7)*, S51-S60.

Seyama, A., and A. Kimura. 1988. The measured properties of irregular wave breaking and wave height change after breaking on the slope, *in Proc. 21st Inter. Conf. on Coast. Eng.*, ASCE, 419-432.

Smith, J. M., A.R. Sherlock, and D.T. Resio. 2001. STWAVE: Steady-State Spectral Wave Model user's guide for STWAVE version 3.0, ERDC/CHL SR-01-01, U.S. Army Engineer Research and Development Center, Vicksburg, MS, 80 pp.

Spath, H. 1985. Cluster Dissection and Analysis: Theory, FORTRAN Programs, Examples, translated by J. Goldschmidt, Halsted Press, 226pp.

Svendsen, I.A., P.A. Madsen, and J. B. Hansen. 1978. Wave characteristics in the surf zone, *in Proc. 16th Inter. Conf. on Coast. Eng.*, ASCE, 520-539.

Stockdon, H.F., and R.A. Holman. 2000. Estimation of wave phase speed and nearshore bathymetry from video imagery, *J. Geophys. Res.*, 105, 22015– 22033.

Suhayda, J.N., and N.R. Pettigrew. 1977. Observations of wave height and wave celerity in the surf zone, *J. Geophys. Res.*, 82 (9), 1419-1424.

Svendsen, I.A. 2006. Introduction to nearshore hydrodynamics, Advanced Series on Ocean Engineering 24, World Scientific, Singapore.

Svendsen, I.A., and J. Veeramony. 2001. Wave breaking in wave groups, *Journal of Waterway, Port, Coastal, and Ocean Engineering*, 127(4), 200-212.

Thornton, E.B., and R.T. Guza. 1982. Energy saturation and phase speeds measured on a natural beach, *J. Geophys. Res.*, 87 (C12), 9499-9508.

Thornton, E.B., and R.T. Guza. 1983. Transformation of wave height distribution, *J. Geophysical Res.*, 88(C10), 5925-5938.

Torrence, C., and G.P. Compo. 1998. A practical guide to wavelet analysis, *Bulletin of the Ameri. Meteo. soci.*, 79(1), 61-78.

Trizna, D.B. 2001. Errors in bathymetric retrievals using linear dispersion in 3D FFT analysis of marine radar ocean wave imagery, *IEEE Trans. Geosciences and Remote Sensing*, 39, 2465-2469.

Van Enckevort, I.M.J., and B.G. Ruessink. 2001. Effects of hydrodynamics and bathymetry on video estimates of nearshore sandbar position, *Journal of Geophysical Research*, 106, pp. 16969–16979.

Williams, J.Z., and J.P. Dugan. 1997. Bathymetry measurements using electro-optical remote sensing, *Proc. of 4th Int. Conf. Remote Sensing for Marine and Coastal Environments*, Orlando, FL.

Work, P.A. 1992. Sediment transport processes at a nourished beach, Ph.D. Thesis, Coastal and Oceanogr. Eng., Univ. of Florida.

Wright, L.D., and A.D. Short. 1984. Morphydynamic variability of surf zones and beaches: A. synthesis, *Marine Geology*, 56, 93-118.